

Actuation characteristics and applications of piezoelectric materials and ionic polymer-metal composites

Zhang, Lei

2008

Zhang, L. (2008). Actuation characteristics and applications of piezoelectric materials and ionic polymer-metal composites. Doctoral thesis, Nanyang Technological University, Singapore.

<https://hdl.handle.net/10356/13076>

<https://doi.org/10.32657/10356/13076>



**NANYANG
TECHNOLOGICAL
UNIVERSITY**

**ACTUATION CHARACTERISTICS AND
APPLICATIONS OF PIEZOELECTRIC
MATERIALS AND IONIC POLYMER-METAL
COMPOSITES**

ZHANG LEI

SCHOOL OF CIVIL & ENVIRONMENTAL ENGINEERING

2008

Actuation Characteristics and Applications of Piezoelectric Materials and Ionic Polymer-Metal Composites

Zhang Lei

School of Civil & Environmental Engineering

A thesis submitted to the Nanyang Technological University
in fulfilment of the requirement for the degree of
Doctor of Philosophy

2008

Dedicate to
My mother, Wen Ying,
And in memory of my father, Shu Qi

Summary

Smart materials are a special class of materials which have abilities to change their physical properties in response to environmental stimuli. One of the important groups of smart materials is electro-active material (EAM) which responds to external electric potentials. Based on the working mechanism, the EAM can be further divided into two groups, i.e., electronic EAMs which rely on internal electrostatic forces for their actuation and ionic EAMs which depend on ion transportation and interaction for their actuation. Piezoelectric material and ionic polymer-metal composite (IPMC) are typical electronic EAM and ionic EAM, respectively.

Piezoelectric materials, when subject to a mechanical force, will become electrically polarized. Tension and compression generate voltages of opposite polarity, and in proportion to the applied force. Conversely, when piezoelectric materials are subject to an electric field parallel to the polarization direction, they will expand or contract according to the polarity of the field, and in proportion to the strength of the field. The two effects are labeled as direct and converse piezoelectric effect and they are the basis for piezoelectric materials as sensors and actuators.

Similar to piezoelectric materials, the IPMCs can also respond to electric and mechanical excitations. Instead of extension and contraction as piezoelectric materials, the IPMCs undergo transverse bending motion under an applied electric potential on the electrodes. On the other hand, the IPMCs can generate a measurable electric potential when it is subject to an imposed deformation. Thus, the IPMCs can also serve as sensors and actuators.

The two types of smart materials, each has its own characteristics, can be employed for different applications in biomedical engineering. The objective of this research is to study the actuation characteristics of piezoelectric materials and IPMCs and explore the possibility of using the two types of materials for biomedical applications.

Summary

Piezoelectric materials actuated plate and shell structures on elastic foundation are first investigated. Analytical solutions are obtained to associate the input electric signal with the structural response. Illustrative examples are provided for plate and shell vibration excited by piezoelectric actuators. In-plane vibration is also studied by using finite different method. The problem of optimal placement of a piezoelectric actuator on the plate and shell in terms of maximizing excitation is investigated based on the vibration solutions. A simple yet general procedure is proposed to find the optimal locations of the piezoelectric actuator on plates and shells.

For the IPMC material, the actuation mechanism of IPMC is studied. Charge redistribution due to applied electric potential in the polyelectrolyte membrane is investigated. Analytical solution of cation motion under dynamic electric potential is presented. Based on Nemat-Nasser's hybrid actuation model, explicit bending moment expressions are derived to account for the bending capacity of IPMC under both the static and dynamic electric potentials. Comparison shows that the bending moment expressions present results in good accordance with experimental data. The bending moment expressions are subsequently used to model IPMC based prototypes for biomedical applications.

In view of possible biomedical needs, three IPMC based prototype models, i.e., an IPMC beam on human tissues, an IPMC ring with elastic medium and an IPMC cylindrical shell with contained flowing fluid, are developed. Analytical solutions are obtained to associate the actuation effects of IPMC with the structural responses. The output effects, i.e., the pressure on the elastic medium or tissues and the velocity changes in flowing fluid, have been obtained. These results are meaningful for further modeling and experimental tests of the three prototypes. Illustrative examples are provided for each of the models.

Acknowledgements

I would like to express my sincere gratitude to my supervisor, Assistant Professor Yang Yaowen, for his invaluable guidance, patience, support and encouragement in conducting this research, without which the completion of this study is incredible.

I would like to express my sincere gratitude to Professor Soh Chee Kiong for his profound vision, research philosophy and methodology. It has been my privilege to obtain instructions from him.

The Research Scholarship offered by Nanyang Technological University is gratefully acknowledged.

Finally, I must acknowledge the constant understanding, encouragement and support provided by my family and friends, near and distant.

Table of Contents

SUMMARY	II
ACKNOWLEDGEMENTS	IV
TABLE OF CONTENTS	V
LIST OF FIGURES	VIII
LIST OF TABLES	XI
CHAPTER 1 INTRODUCTION	1
1.1 BACKGROUND	1
1.2 OBJECTIVES AND SCOPE OF THE RESEARCH	2
1.3 ORGANIZATION OF THESIS	4
CHAPTER 2 A REVIEW ON SMART MATERIALS.....	6
2.1 OVERVIEW OF SMART MATERIALS	6
2.2 PIEZOELECTRIC MATERIALS.....	7
2.2.1 History and characterizations.....	7
2.2.2 Piezoelectric actuators.....	11
2.2.3 Piezoelectric actuator-structure interaction	14
2.2.4 Optimal placement of piezoelectric actuators.....	17
2.3 IONIC POLYMER-METAL COMPOSITES	21
2.3.1 History and characterizations.....	21
2.3.2 Experimental study and physical modeling.....	24
2.3.3 Implemented and potential applications	30
2.4 CONCLUDING REMARKS	32
CHAPTER 3 MODELING OF PIEZOELECTRIC MATERIAL ACTUATED	
PLATE AND SHELL	33
3.1 INTRODUCTION	33
3.2 PIEZOELECTRIC ACTUATED PLATE	34
3.2.1 Problem formulation.....	34
3.2.2 Analytical solution	39
3.2.3 Illustrative example.....	43
3.2.4 In-plane vibration of piezoelectric actuated plate.....	46
3.3 VIBRATION OF PIEZOELECTRIC ACTUATED CYLINDRICAL SHELL	52
3.4 CONCLUSIONS	57
CHAPTER 4 OPTIMAL PLACEMENT OF PIEZOELECTRIC	
ACTUATORS ON PLATE AND SHELL	58

Table of Contents

4.1 INTRODUCTION	58
4.2 OPTIMAL PLACEMENT OF PZT ACTUATOR ON PLATE.....	58
4.2.1 Driving frequencies close to natural frequencies.....	59
4.2.2 Driving frequencies not close to natural frequencies.....	68
4.2.3 General procedure to determine PZT optimal locations via CPMF	75
4.3 OPTIMAL PLACEMENT OF PZT ACTUATOR ON SHELL	76
4.4 DISCUSSIONS	79
4.4.1 Driving frequency lower than the first natural frequency.....	79
4.4.2 Effect of PZT size	80
4.4.3 Effects of material properties, foundation stiffness and in-plane forces.....	81
4.5 CONCLUSIONS	81
CHAPTER 5 MODELING OF IONIC POLYMER-METAL COMPOSITES	82
5.1 INTRODUCTION	82
5.2 BENDING MOMENT CAPACITY OF IPMC	83
5.2.1 Charge redistribution.....	83
5.2.2 Bending moment.....	91
5.3 VALIDATION AND DISCUSSIONS	100
5.4 CONCLUSIONS	108
CHAPTER 6 APPLICATIONS OF IONIC POLYMER-METAL COMPOSITES	109
6.1 INTRODUCTION	109
6.2 IPMC BEAM STRUCTURE ON HUMAN TISSUES.....	109
6.2.1 Modeling of IPMC beam on human tissues.....	110
6.2.2 Illustrative examples and discussions	112
6.2.2.1 Illustrative examples.....	112
6.2.2.2 Optimal electrode length.....	115
6.2.2.3 Multiple electrodes	119
6.2.3 Concluding remarks.....	121
6.3 IPMC RING STRUCTURE WITH ELASTIC MEDIUM.....	122
6.3.1 Problem formulation.....	122
6.3.2 Displacement solutions	126
6.3.3 Illustrative example.....	128
6.3.4 Concluding remarks.....	137
6.4 IPMC SHELL STRUCTURE WITH FLOWING FLUID.....	137
6.4.1 Problem formulation.....	137
6.4.1.1 Motion equation of cylindrical shell	137
6.4.1.2 Fluid perturbation	140
6.4.2 Wave propagation solutions.....	144
6.4.3 Illustrative example and discussion	148

Table of Contents

6.4.4 Concluding remarks.....	151
6.5 CONCLUSIONS	151
CHAPTER 7 CONCLUSIONS AND RECOMMENDATIONS	153
7.1 SUMMARY AND CONCLUSIONS.....	153
7.2 FUTURE WORK	155
REFERENCES.....	157
LIST OF PUBLICATIONS	167

List of Figures

Figure 2.1 A typical PZT unit cell	8
Figure 2.2 PZT unit cell deformations (a) Original state (b) d_{33} effect (c) d_{31} effect (d) d_{15} effect	8
Figure 2.3 Definition of axes for PZT sheet	10
Figure 2.4 Structures of IPMC (Nemat-Nasser and Thomas, 2001).....	22
Figure 2.5 Microstructure of platinum electrode surface.....	22
Figure 2.6 Chemical structures of polyelectrolyte membrane used in IPMCs (a) Nafion, (b) Flemion, and (c) Aciplex.....	23
Figure 2.7 IPMC under electric potential (Shahinpoor and Kim, 2001)	23
Figure 2.8 A heart with IPMC compression band (Shahinpoor and Kim, 2004)	31
Figure 2.9 Four-finger gripper (Shahinpoor and Kim, 2004)	31
Figure 2.10 Artificial fish (Shahinpoor and Kim, 2004)	31
Figure 2.11 An IPMC linear actuator (Yamakita et al, 2004)	32
Figure 3.1 (a) Plate and PZT actuator system (b) Plate and PZT actuator coordinate system	34
Figure 3.2 Deflection of rectangular plate actuated by one PZT actuator at center ($\omega=18849.6$ rad/s)	44
Figure 3.3 Deflection of rectangular plate actuated by one PZT actuator at ($\xi=\eta=0.3$) ($\omega=18849.6$ rad/s)	45
Figure 3.4 Convergence of Eq.(3.37) vs m and n	45
Figure 3.5 Central finite difference meshes.....	47
Figure 3.6 In-plane displacement of plate in x direction	50
Figure 3.7 In-plane displacement of plate in y direction	51
Figure 3.8 In-plane displacement field of plate with contour plot.....	51
Figure 3.9 Stress resultants on a shell element	52
Figure 3.10 Deformation of cylindrical shell segment actuated by a pair of PZT actuators at center ($\omega=5155$ rad/s).....	56
Figure 4.1 Optimal location patterns of a PZT actuator on a rectangular plate with $\beta=1.5$ at driving frequencies close to natural frequencies	60
Figure 4.2 First nine mode shapes of rectangular plate	61

List of Figures

Figure 4.3 Optimal locations of a PZT actuator on rectangular plate with driving frequency closes to natural frequency of vibration modes (2,2) and (4,1)	65
Figure 4.4 Plot of CPMF $\Psi = \chi_{22} + \chi_{41}$	66
Figure 4.5 Optimal location patterns of a PZT actuator on a square plate at driving frequencies close to natural frequencies	67
Figure 4.6 Plots of CPMFs for square plate.....	68
Figure 4.7 Optimal location patterns of a PZT actuator on a rectangular plate with driving frequencies not close to natural frequencies.....	73
Figure 4.8 Optimal location patterns of a PZT actuator on a square plate with driving frequencies not close to natural frequencies.....	75
Figure 4.9 Numerical results of optimal location pattern of a pair of collocated PZTs when $\omega = 5155$ rad/s	78
Figure 4.10 Optimal location pattern of a pair of collocated PZTs when $\omega = 5155$ rad/s determined by Eq.(4.17).....	78
Figure 4.11 Optimal locations when driving frequency is near zero ($\omega = 0.0628$ rad/s)	79
Figure 4.12 Optimal locations when driving frequency lower than the first natural frequency ($\omega = 25133$ rad/s)	80
Figure 5.1 Cross section of a Pt-plated Nafion based IPMC	82
Figure 5.2 Schematic drawing of the cross-section of an IPMC sample	84
Figure 5.3 Comparison between analytical and numerical solutions	101
Figure 5.4 Configuration of an IPMC cantilevered beam	102
Figure 5.5 Comparison between calculated displacement and data in Nemat-Nasser (2002).....	104
Figure 5.6 IPMC cantilever beam deflections at $t = 1/(12f)$, $t = 1/(6f)$ and $1/(4f)$	107
Figure 6.1 Configuration of an IPMC beam on human tissues	110
Figure 6.2 Deflection of IPMC beam under 1 volt sinusoidal potential ($k = 15$ kPa)	113
Figure 6.3 Pressure distribution on human tissue under 1 volt sinusoidal potential ($k = 15$ kPa).....	114
Figure 6.4 Displacements vs. tissue stiffness.	114
Figure 6.5 Pressure vs. tissue stiffness	115

List of Figures

Figure 6.6 Relationship between electrode coordinates and maximum beam deflection ($k=15$ kPa)	117
Figure 6.7 Relationship between electrode coordinates and maximum beam deflection ($k=40$ kPa)	117
Figure 6.8 Relationship between electrode coordinates and maximum beam deflection ($k=0.9$ kPa)	118
Figure 6.9 Relationship between electrode coordinates and pressure ($k=0.9$ kPa)	118
Figure 6.10 Relationship between electrode coordinates and pressure ($k=15$ kPa)	119
Figure 6.11 Relationship between electrode coordinates and pressure ($k=40$ kPa)	119
Figure 6.12 Configuration of two discrete electrodes	120
Figure 6.13 Deflection of beam with two electrodes under identical potentials	120
Figure 6.14 Deflection of beam with two electrodes under opposite potentials	121
Figure 6.15 A circular IPMC ring filled with elastic medium	122
Figure 6.16 Deformation of IPMC ring with electrode area of $\pi/6$	129
Figure 6.17 Deformation of IPMC ring with electrode area of $\pi/3$	129
Figure 6.18 Deformation of IPMC ring with electrode area of $\pi/2$	130
Figure 6.19 Deformation of IPMC ring with electrode area of π	130
Figure 6.20 Deformation of IPMC ring with electrode area of $3\pi/2$	131
Figure 6.21 Deformation of IPMC ring with electrode area of 1.9π	131
Figure 6.22 Deformation of IPMC ring with electrode area of 2π	132
Figure 6.23 Electrode areas vs. maximum radial displacements	133
Figure 6.24 Configuration of two active electrode areas of IPMC ring	134
Figure 6.25 Deformation of IPMC ring with two electrodes	134
Figure 6.26 Electrode area vs. maximum radial displacement for different elastic media	136
Figure 6.27 Pressure distribution of IPMC ring with two electrodes	136
Figure 6.28 Configuration of IPMC circular cylindrical shell filled with fluid	138
Figure 6.29 Amplified shell deformation at electric signal of 1.5 V/0.25 Hz (10 times)	149
Figure 6.30 Shell deformation at electric signal of 3 V/0.25 Hz	150
Figure 6.31 Cylindrical shell with multiple electrodes	151

List of Tables

Table 3.1 Material properties and constants for plate and PZT	43
Table 3.2 Material properties and constants for shell and PZT	56
Table 5.1 Parameters, symbols and values for an IPMC sample with Li^+ as cation	102
Table 5.2 Parameters, symbols and values for an IPMC sample with Na^+ as cation	105
Table 6.1 Maximum radial displacements for different electrode areas.....	132

Chapter 1 Introduction

1.1 Background

Materials are the basis of human civilization. Every stage of mankind history is characterized by its materials used, such as the Stone Age and the Bronze Age hundreds of thousands of years ago, the age of silicon that we are experiencing and the emerging age of smart and nano-materials. Smart materials are a special class of materials which have abilities to change their physical properties in response to environmental stimuli. They are also called intelligent materials because of their resemblances to biological creatures under stimuli. The stimuli could be pressure, temperature, electric and magnetic fields, chemicals or radiation. The changeable physical properties associated with these stimuli could be shape, stiffness, viscosity or damping. Those smart materials that can respond to electric stimuli are called electro-active materials (EAMs). Due to their ease of manipulation and excitation, the EAMs form an important category in smart materials. Based on their working mechanisms, the EAMs can be further divided into two major groups, the electronic EAMs and the ionic EAMs (Bar-Cohen, 2001). The electronic EAMs, rely on electrostatic forces for their actuation. The electronic EAMs are usually stiffer than the ionic EAMs and capable of producing rapid responses and large forces. However, the required electric potential is usually as high as hundred to thousand volts and the strains are generally small. On the other hand, the ionic EAMs, involve ion transportations, chemical reactions and electrostatic forces in their actuation. They can provide large strains under low electric potential. However, because the ionic EAMs are generally compliant, the resulting force is usually small. The response speed of ionic EAMs varies from milliseconds to seconds. Piezoelectric materials and ionic polymer-metal composites (IPMCs) are typical electronic EAM and ionic EAM, respectively.

Chapter 1 Introduction

Piezoelectric materials have a long history compared to other smart materials. The discovery of piezoelectricity can be dated back to the late 19th century by Pierre and Jacques Curie (Ikeda, 1990). Piezoelectricity consists of direct and converse piezoelectric effects. The former property lies in the ability of piezoelectric materials to generate electric charge in proportion to external force, which enables them as stress/strain sensors. The converse piezoelectric effect of these materials refers to their expansion or contraction under the existence of electric field parallel to the direction of polarization, which enables them as controllable actuators.

Similar to piezoelectric materials, the IPMCs can also respond to electric potential. Instead of extension and contraction as piezoelectric materials, the IPMCs undergo transverse bending under electric signals. When the IPMCs are suddenly bent, measurable electric charges can be detected on the electrodes of IPMCs. The IPMCs also have the potential to be used as sensors and actuators.

These two kinds of EAMs, each having its own characteristics, can be used for different applications in biomedical engineering. In this thesis, the actuation characteristics of piezoelectric materials and IPMCs are studied. Prototype models are developed to employ the two types of EAMs for potential biomedical engineering applications. Emphases are on the modeling of dynamic behaviors of piezoelectric materials and IPMCs and their interactions with structures. The effect of EAMs actuation, force or displacement output, is optimized to suit different purposes.

1.2 Objectives and scope of the research

The main objective of this research is to study the actuation characteristics of piezoelectric materials and IPMCs and explore the possibility of using the two types of materials for biomedical applications.

Specifically, the present work has the following major contributions:

Chapter 1 Introduction

- 1) Dynamic models of piezoelectric material actuated plate and shell structures on an elastic foundation are developed. Analytical solutions of transverse vibration are derived. In-plane vibration of plate is evaluated by finite difference method. These models build up the relationship between the structural response and the input electric signals on piezoelectric materials.
- 2) Optimal placement of piezoelectric materials on plates and shells in terms of optimal excitation is investigated. A simple yet general procedure is proposed to find the optimal locations of piezoelectric materials on plates and shells. This procedure only requires the calculation of natural frequencies of structures and therefore easy to implement.
- 3) The dynamic behaviors of IPMCs are studied. Explicit bending moment expressions are proposed by simplifying Nemat-Nasser's hybrid actuation model (Nemat-Nasser, 2002). The solutions provide an easy estimation of the bending capacity of IPMCs for certain hydration rate and given counter ion type, thus easing the modeling of IPMC components.
- 4) Three prototypes of IPMCs for biomedical applications, i.e., a beam structure for minimum invasive surgery, a ring structure for heart compression band and a fluid-filled cylindrical shell for artificial vessels are proposed and modeled. Analytical solutions are obtained to associate the actuation effects of IPMCs with the structural responses. The solutions and conclusions obtained are not limited for use in the proposed biomedical applications.

1.3 Organization of thesis

This thesis consists of seven chapters. Following the introduction given in this chapter, Chapter 2 presents a general description of smart materials especially piezoelectric materials and IPMCs. Fundamentals of piezoelectricity theory and research on piezoelectric actuators, actuator-structure interactions and optimal placements of piezoelectric actuators are presented. A brief history of IPMCs and research development on the mechanism of IPMC actuation and sensing are reviewed. A review on the applications of the two types of EAMs is also presented.

Chapter 3 presents formulations of piezoelectric materials actuated plate and shell structures. Firstly, a simply supported plate subject to in-plane forces, bonded on an elastic foundation and excited by a PZT actuator is investigated. Analytical solution is obtained to predict the deflection of the plate. The pressure generated on the elastic foundation is evaluated. The in-plane vibration is also studied by finite difference method. Calculation examples are provided for illustration. Subsequently, the formulation and solution procedures are applied to a simply supported cylindrical shell on an elastic foundation actuated by a pair of collocated PZT actuator. Closed form solution is also obtained.

In Chapter 4, the problem of optimal placement of PZT actuator on plate and shell in terms of maximizing the vibration is investigated. It is found that the optimal locations of the PZT actuator are dependent on the driving frequency of the actuator and the natural frequencies of the plate and shell. A function named combined position mode function (CPMF) is proposed to identify the optimal locations of a piezoelectric actuator on plate and shell no matter whether the driving frequency is close to the natural frequencies or not. A general but simple procedure is proposed for optimal excitation of structures. The effect of the geometry of PZT actuator on the excitation of plate is discussed.

The actuation mechanism of IPMC materials is studied in Chapter 5. By using Taylor's series expansion, explicit bending moment expressions are derived through

Chapter 1 Introduction

Nemat-Nasser's hybrid actuation model for both static and dynamic electric potentials. Comparisons are made between the proposed bending moment expression and the experimental results in literature. The formulae provide an easy way to estimate the bending capacity of IPMC materials at a given hydration rate.

Chapter 6 illustrates three different models of IPMC based structures, i.e., an IPMC beam on human tissues, an IPMC ring with elastic medium and a fluid-filled IPMC cylindrical shell, for possible biomedical applications. In view of possible applications of IPMCs as minimally invasive surgery tools, a dynamic IPMC beam model on human tissue is developed. An analytical solution is obtained to describe the vibration response of the IPMC beam to an electric potential. Based on the analytical solution, the beam deflection curve and the pressure distribution generated on human tissue were obtained. The optimal electrode location and length in terms of maximizing the deflection and generative pressure are discussed. The deflection curve and generative pressure for a multiple discrete electrode IPMC beam are also obtained. To model heart compression band, the vibration of an IPMC ring with elastic medium under harmonic electric signal is investigated. An analytical solution of IPMC ring vibration under electric potential is obtained. The deformation of IPMC ring under different electrode areas and the pressure generated on elastic medium inside the ring are calculated. Multiple electrodes are also considered for use in the IPMC ring. Illustrative examples are provided. Lastly, a dynamic model of a fluid-filled IPMC shell for artificial vessels is developed. The vibration response of the shell and the velocity field of the contained fluid under the applied electric potential are obtained by the wave propagation method. An illustrative example is presented. It is found that the flow velocity can be enhanced by the application of electric potential on the IPMC shell. It is also possible to further increase the axial flow by multiple electrodes and the solutions obtained in this section can be extended to multiple electrode analysis.

Finally, the main conclusions of this study and the recommendations for future research are summarized in Chapter 7.

Chapter 2 A Review on Smart Materials

2.1 Overview of smart materials

Rogers et al. (1988) defined smart materials as materials which have ability to change their physical properties in a specific manner in response to certain specific stimulus input. The stimulus could be pressure, temperature, electric and magnetic fields, chemicals or nuclear radiation. The changeable physical properties associated with these stimuli could be shape, stiffness, viscosity or damping.

Shape memory alloys (SMAs), fiber optics, piezoelectric ceramics and polymers, electrostrictive materials, electrorheological (ER) fluids, magnetostrictive (MS) materials, conductive polymer and ionic polymer-metal composites (IPMCs) are some typical smart materials. Because of their unique capability of responding to stimuli, smart materials have been employed in numerous applications in the field of sensors and actuators. Piezoelectric materials, for example, generate a surface charge (response) upon the application of mechanical stress (stimulus) and conversely, undergo a material deformation in response to an applied electric field. Similarly, the ER fluids have inherent ability to undergo an abrupt and reversible change in viscosity and hence internal damping (response) when subjected to electrostatic potentials (stimulus). A detailed description of smart materials has been presented by Thompson et al. (1992).

Due to easy actuation, smart materials that respond to electric stimuli form an important category. They can be called as electroactive materials (EAMs). Based on the working mechanism, the EAMs can be further divided into two groups, the electronic EAMs and the ionic EAMs (Bar-Cohen, 2001). The electronic EAMs rely on electrostatic forces for their actuation. The electronic EAMs are usually stiffer than the ionic EAMs and capable of producing rapid response and large forces. However, the required electric potential is usually as high as hundred to thousand volts and the strains are generally small. The ionic EAMs, on the other

Charter 2 A Review on Smart Materials

hand, involve ion motions, chemical reactions and electrostatic forces in their actuation. They can provide large strains under low electric potential. However, because the ionic EAMs are generally compliant, the resulting forces are usually small. The response speed of ionic EAMs varies from milliseconds to seconds. Piezoelectric materials and ionic polymer-metal composites (IPMCs) are typical electronic EAM and ionic EAM, respectively. The actuation characteristics of the two kinds of smart materials are the concern of this research. Reviews on piezoelectric materials and IPMCs are presented in the following sections.

2.2 Piezoelectric materials

2.2.1 History and characterizations

In 1880, Jacques and Pierre Curie discovered an unusual characteristic in certain crystalline minerals: when subjected to a mechanical force, the crystals became electrically polarized. Tension and compression generated voltages of opposite polarity, and in proportion to the applied force. Subsequently, the converse of this relationship was confirmed: if these voltage-generating crystals were exposed to an electric field, they lengthened or shortened according to the polarity of the field, and in proportion to the strength of the field. These behaviors were labeled the direct piezoelectric effect and the converse piezoelectric effect, respectively.

The piezoelectric effect can be explained by the displacement of ions in crystals that have a nonsymmetrical unit cell. Fig.2.1 illustrates a typical lead-zirconate-titanate (PZT) unit cell. As shown in Fig.2.2, when the crystal is pulled, compressed or distorted, the ions in each unit cell are displaced, causing the electric polarization of the unit cell. Because of the uniformity of crystalline structure, these effects accumulate, inducing an electric potential difference between certain surfaces of the crystal. When an external electric field is applied to the crystal, the ions in each unit cell are displaced by electrostatic forces, resulting in the mechanical deformation of the whole crystal.

Charter 2 A Review on Smart Materials

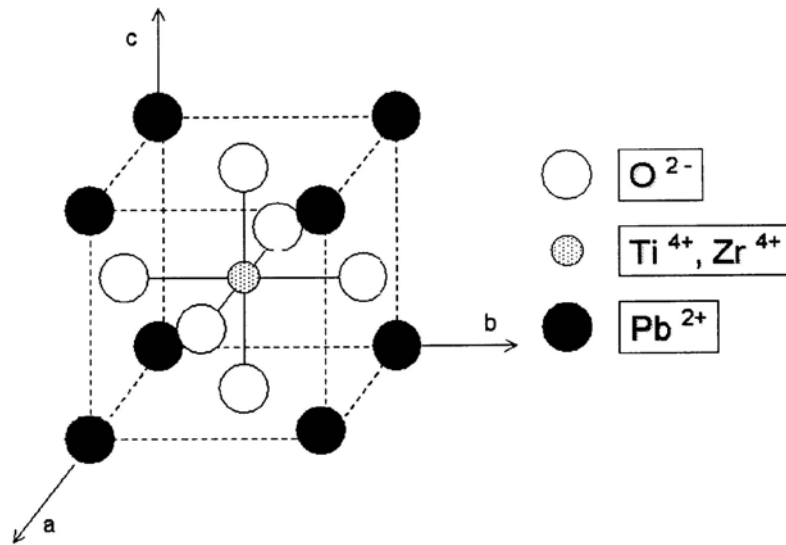


Figure 2.1 A typical PZT unit cell

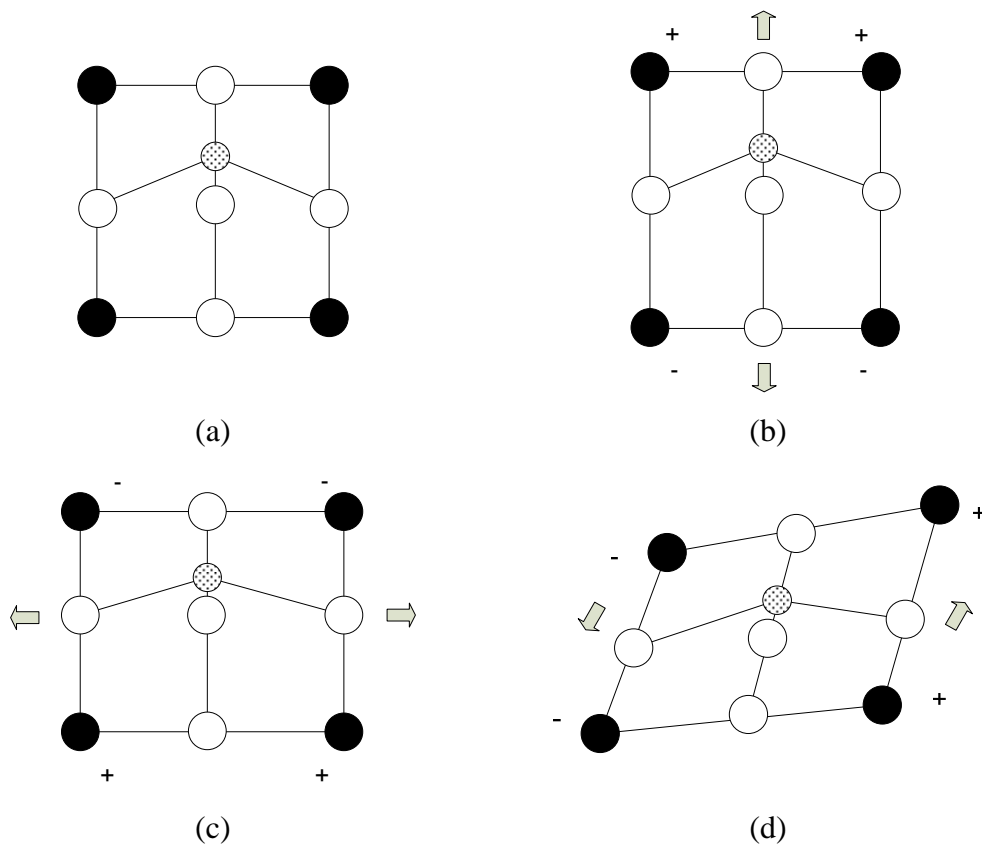


Figure 2.2 PZT unit cell deformations (a) Original state (b) d_{33} effect (c) d_{31} effect (d) d_{15} effect

Charter 2 A Review on Smart Materials

The most popular piezoelectric materials are PZT which is a ceramic, and polyvinylidene fluoride (PVDF) which is a polymer. PZT is one of the most commonly used piezoceramics. It is a solid solution of lead zirconate and lead titanate, often doped with other materials to obtain specific properties. PZT is manufactured by heating a mixture of lead, zirconium and titanium oxide powders to around 800-1000°C. This heating results in a perovskite PZT powder, which is mixed with a binder and sintered into the desired shape. The resulting unit cell is elongated in one direction and has a permanent dipole moment along this axis. However, since the ceramic consists of many such randomly oriented domains, it has no net polarization. In order to align the unit cells in a particular direction, a high electric field is applied. This process is called poling, and it imparts a permanent net polarization in the ceramic.

Due to the poling process, the material becomes transversely isotropic in the plane normal to the poling direction. PZT sheets have high stiffness, which renders them as good actuators. PZT ceramic has been designed as solid-state sensors and actuators for many applications such as precision positioning, noise and vibration sensing and cancellation, linear motor and so on (Uchino, 1996).

Under small field conditions, the constitutive relations for a piezoelectric ceramic are (IEEE Standard, 1987),

$$D_i = e_{ij}^{\sigma} E_j + d_{im}^d \sigma_m \quad (2.1)$$

$$\varepsilon_k = d_{jk}^c E_j + s_{km}^E \sigma_m \quad (2.2)$$

where D_i is the electric displacement; ε_k is the strain vector; E_j is the applied electric field and σ_m is the stress vector. The piezoelectric constants are the dielectric permittivity e_{ij}^{σ} , the piezoelectric coefficients d_{im}^d and d_{jk}^c , and the elastic compliance s_{km}^E . The superscripts d and c are added to differentiate the direct and converse effects, respectively, and the superscripts σ and E indicate that the quantity is measured at constant stress and constant electric field, respectively.

Charter 2 A Review on Smart Materials

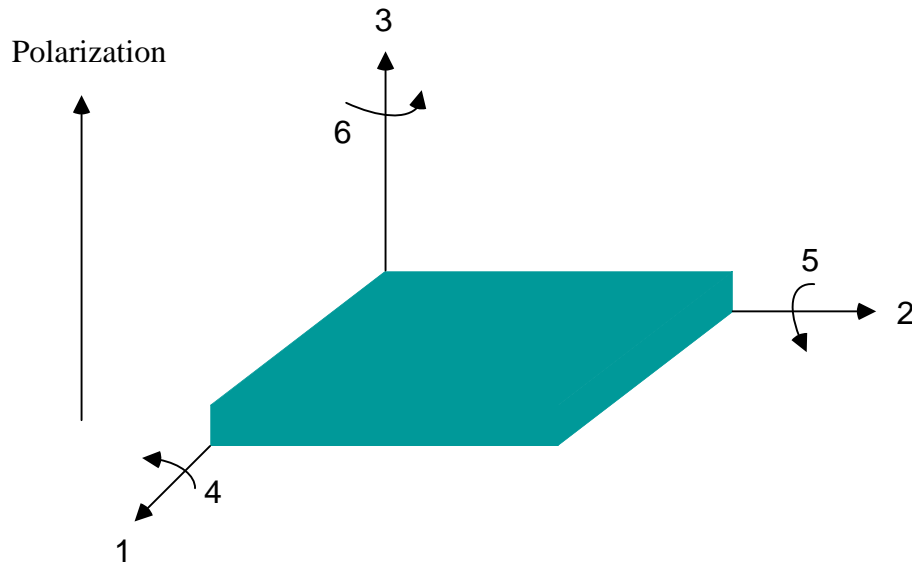


Figure 2.3 Definition of axes for PZT sheet

As shown in Fig.2.3, the poling direction, which is generally along the thickness of a PZT sheet, is denoted as the 3-axis. The 1-axis and 2-axis are in the plane of the PZT sheet. The materials are normally assumed isotropic in the 1-2 plane. The piezoelectric coefficient matrix d_{jk}^c can be expressed as

$$\mathbf{d} = \begin{bmatrix} 0 & 0 & d_{31} \\ 0 & 0 & d_{31} \\ 0 & 0 & d_{33} \\ 0 & d_{15} & 0 \\ d_{15} & 0 & 0 \\ 0 & 0 & 0 \end{bmatrix} \quad (2.3)$$

where d_{31} and d_{33} relate the normal strains in the 1 and 3 directions respectively to a field along the poling direction, while d_{15} relates the shear strain in the 2-3 and 1-3 planes. The elastic compliance matrix is

Charter 2 A Review on Smart Materials

$$\mathbf{s} = \begin{bmatrix} S_{11} & S_{12} & S_{13} & 0 & 0 & 0 \\ S_{12} & S_{22} & S_{13} & 0 & 0 & 0 \\ S_{13} & S_{13} & S_{33} & 0 & 0 & 0 \\ 0 & 0 & 0 & S_{44} & 0 & 0 \\ 0 & 0 & 0 & 0 & S_{44} & 0 \\ 0 & 0 & 0 & 0 & 0 & S_{66} \end{bmatrix} \quad (2.4)$$

and the permittivity matrix is

$$\mathbf{e}^{\sigma} = \begin{bmatrix} e_{11}^{\sigma} & 0 & 0 \\ 0 & e_{11}^{\sigma} & 0 \\ 0 & 0 & e_{33}^{\sigma} \end{bmatrix} \quad (2.5)$$

Eq.(2.1) is the sensing equation based on the direct piezoelectric effect and Eq.(2.2) is the actuating equation based on the converse piezoelectric effect.

PVDF is made up of long chains of repeating monomer (-CH₂-CF₂-). Each monomer has an inherent dipole moment. PVDF film is manufactured by solidification of the film from the molten phase, which is then stretched in a particular direction and finally poled. The stretching process aligns the chain in the direction of stretching. Combined with poling, this imparts a permanent dipole moment to the film. Because of stretching, the material is rendered piezoelectrically orthotropic, that is $d_{31} \neq d_{32}$, where '1' is the stretching direction. The PVDF material is characterized by low stiffness (Young's modulus is about 1/12th that of aluminum). Also, PVDF films can be shaped as desired according to the intended application. These characteristics make PVDF films more attractive for sensor applications, despite of their low piezoelectric coefficients (approximately 1/10th of PZT).

2.2.2 Piezoelectric actuators

There are many kinds of actuators used for various applications. The three most common types of piezoelectric actuators are the multilayer ceramic actuators, the bimorph or unimorph actuators and the flextensional composite actuators.

Charter 2 A Review on Smart Materials

The multilayer actuators, in which certain thin ceramic sheets are stacked together with internal electrodes utilizing the direct extensional mode, are characterized by large generated force, high electromechanical coupling, high resonant frequency, low driving voltage and quick response but small displacement.

The bimorph or unimorph actuators consist of two thin ceramic sheets or one ceramic sheet and one metal sheet bounded together with poling and driving direction normal to the interface. When driven, the alternative extension and shrinkage of ceramic sheets due to transverse mode result in a pure bending vibration. This kind of actuator can generate large displacement but low electro-mechanical coupling, low resonant frequency and low driving force.

For the flextensional composite actuators, two typical examples are so called “moonie” and “cymbal” actuators, which consist of a piezoelectric or electrostrictive ceramic disk and metal end-caps. The ceramic is excited in an extensional mode and the metal caps in a flexure mode. The metal end-caps act as a mechanical transformer converting and amplifying the radial displacement ceramic into linear motion. Quite large displacement can be achieved by this kind of actuator.

Wang et al. (1996) investigated the characteristics of cantilevered shear mode piezoelectric actuators. The soft PZT ceramic plate was poled along its length and driven across its thickness, with one end mechanically clamped and the other end free. Experimental results showed that relative large tip displacement can be obtained through nonlinear piezoelectric response at high driving electric field.

Glazounov and Zhang (1998) proposed a piezoelectric actuator generating angular displacement from the piezoelectric d_{15} shear response. The actuator was a tube consisting of an even number of segments poled along the length, which was adhesively bonded together, and the joints acted as electrodes to apply the driving voltage. The experimental results showed that the actuator functioned well under torque load and demonstrated superior characteristics compared with previously reported torsional actuators. Centolanza and Smith (2002) applied this torsional actuator to actively twist rotor blades.

Charter 2 A Review on Smart Materials

Dong et al. (2001) presented a ring-type piezoelectric actuator that combined a ring shaped piezoelectric component with a thin disc. In this actuator, the ring-shaped piezoelectric ceramic produced a radial contraction or expansion, resulting in a large flexural displacement at the center of the metal disc. Both experimental and finite element analysis proved the concept.

Wang et al. (2002) described two kinds of piezoelectric multilayer microactuators for the dual stage actuation systems in high track density hard disk drive, namely split-morph and annular split-morph. These piezoelectric multiplayer microactuators possessed a useful compromise performance among displacement, resonance frequency and generated force. Together with their thin plate-like features and low drive voltage, they were particularly suitable for mounting on the suspension of a head gimbal assembly or between the flexure tongue and slider as the secondary fine-tuning actuator. Their research revealed that the new design concept provided a valuable alternative for multilayer piezoelectric actuators.

To overcome the disadvantage of limited generative displacement of multilayer piezoelectric actuator, Kim et al (2003) proposed a three-dimensional bridge type flexure hinge mechanism to amplify the displacement of a commercial piezo-stack. The mechanism was composed of two bridge mechanisms which were symmetrically connected in vertical direction. The mechanism had high amplification ratio in small size which made it suitable for miniaturization and fast motion.

Chu et al (2006) designed a disk-pivot micro piezoelectric actuator by using certain vibration mode. This actuator was composed of a metal disk stator with a piezoelectric ceramic disc, a metal rod rotor and auxiliary parts. The piezoelectric disk was used to excite wobble mode vibrations, the metal cylinder stator was used to amplify the transverse displacement and the metal rod rotor was actuated to rotate. This actuator had advantages of low driving voltage, micromotion and convenient control of wobble state.

Charter 2 A Review on Smart Materials

2.2.3 Piezoelectric actuator-structure interaction

The applications of piezoelectric actuators are usually associated with a host structure, such as beam and plate. Many analytical and numerical models have been introduced in literature to describe the behavior of structures with piezoelectric actuators.

Crawley and Luis (1987) presented an analytical and experimental development of piezoelectric actuators as elements of intelligent structures. Both static and dynamic analytic models were derived for the segmented piezoelectric actuators that either bonded to an elastic substrate or embedded in a laminated composite. These models led to the prediction of the response of the structural member to an electric potential applied to the piezoelectric, thus providing guidance as to the optimal location for actuator placement.

Dimitriadis et al (1991) extended the analysis to two dimensional thin plate vibration actuated by distributed piezoelectric actuators. Their computation results showed that the vibration modes could be selectively excited and the geometry of the actuator shape had great effects on the distribution of the response among modes.

The idea of exploiting the shear mode to create transverse deflection in sandwich beams was first suggested by Sun and Zhang (1995). The ANSYS package was used to numerically model a cantilevered beam with a shear mode piezoelectric actuator. It was shown that embedded shear actuators offered many advantages over surface mounted extension actuators.

Later, Zhang and Sun (1996) formulated an analytical model of a sandwich beam with a shear piezoelectric actuator that occupied the entire core. The model derivation was simplified by assuming that the face layers follow an Euler–Bernoulli beam model, whereas the core layer acts as a Timoshenko beam model.

Charter 2 A Review on Smart Materials

Furthermore, a closed-form solution of the static deflection was presented for a cantilevered beam.

Chandrashekhara and Varadarajan (1997) presented a numerical model of a composite beam using a higher-order shear deformation theory. Extension piezoelectric elements were used to produce the desired deflection in beams with clamped-free, clamped-clamped and simply supported ends.

An analytical formulation and closed-form solutions of composite beams with extension piezoelectric actuators was presented by Abramovich (1998). The beam model was based on the first-order shear deformation theory. Static shape control for beams with various boundary conditions was demonstrated.

Aldraihem and Khdeir (2000) proposed a deflection analysis of beams with piezoelectric patches. It was shown that the results of the first order beam theory were very sensitive to the value of the shear correction factor. The results also indicated that a shear mode actuator could not generate deflection in a hinged-hinged beam and that extension mode actuators could not generate deflection in a clamped-clamped beam. For all other boundary conditions, the deflection provided by the extension actuators was always greater than that from a shear actuator for the identical electric field intensity.

The actuation performance of smart beams with extension and shear mode piezoelectric actuators was studied by Khdeir and Aldraihm (2001). The First-order and higher-order shear deformation beam theories were adopted. The piezoelectric stress resultants were expressed in terms of Heaviside functions. The results showed that the shear patches created the largest deflection if they were placed near the supports, whereas the extension patches produced the largest deflection at the beam center. For clamped-hinged and clamped-clamped beams, shear patches performed better than the extension patches.

Charter 2 A Review on Smart Materials

Preumont (2002) has studied the effect of a laminar piezoelectric actuator bonded on one surface of a beam. The study showed that for a laminar actuator of constant width, the effect of the distributed actuator is equivalent to adding a concentrated moment at the boundary of the actuator. The expression for the concentrated moment was derived.

Aldraihm and Khdeir (2003) developed a precise deflection model of beams with collocated piezoelectric patches by the first-order and higher-order beam theories. Analytical solutions were obtained with the aid of the state-space approach and the Jordan canonical form. It was shown that the first-order beam lacked the ability to accurately predict the beam behavior in the region of the patches when compared with the results of the higher-order beam. They also investigated the effects of patch length and location on the deflected shape of beams with two piezoelectric pairs. For the clamped–hinged and clamped–clamped beams, the deflected shape switched from negative to positive when the piezoelectric pairs were moved toward the supports. The results of clamped–clamped beams indicated that increasing the patch length did not necessarily increase the deflection. The solutions could be used in the design process to obtain detailed deformation information of beams with various boundary conditions.

Vel et al (2004) presented an analytical solution for the cylindrical bending motions of linear piezoelectric laminated plates by extending the Stroh formalism which was a sextic formalism for two-dimensional deformations of anisotropic elastic materials (Ting, 1996). Fourier basis functions for the mechanical displacements and electric potential that identically satisfied the motion equations and charge equation of electrostatics were used to solve the boundary value problem via the superposition principle.

Baillargeon and Vel (2005) obtained an exact three-dimensional solution for the cylindrical bending vibration of simply supported laminated composite plates with an embedded piezoelectric shear actuator. Suitable displacement and electric potential functions that satisfied the simply supported boundary condition were used

Charter 2 A Review on Smart Materials

to reduce governing equation to a set of coupled ordinary differential equations which were then solved by the power series method.

For a structure bonded with multiple PZT patches, Cheng and Lin (2005) proposed a method to formulate the couplings between the PZT patches and the host structure and among the PZT patches themselves based on the impedance technique. Their method provides an alternative to solve the inverse vibration problem analytically.

Qing et al (2006) presented a realistic mathematical model for the static and dynamic analysis of a plate with piezoelectric patches. The plate and the piezoelectric patches were discretized by the same linear quadrilateral element. The linear algebraic equations of the plate and the piezoelectric patches were established independently. The numerical results showed that their proposed method offered good predicative capability.

Based on the kinematical assumption of the Love-Kirchhoff thin plate theory including the shear function with a quadratic variation of the electric potential along the thickness direction of the piezoelectric patches, Fernandes and Pouget (2006) investigated the static and dynamic response of a plate with piezoelectric elements. In this investigation, the stiffness and the inertial contributions of the piezoelectric patch were not neglected. Their approach could accurately predict the global and local response of composite structure.

2.2.4 Optimal placement of piezoelectric actuators

Once PZT patches are adopted as actuators in a smart system, concerns will arise on where to place the actuators. Appropriate placement of actuators would promote system efficiency, improve controllability and observability as well as save materials and energy.

Charter 2 A Review on Smart Materials

Kang et al. (1996) studied the optimal placement of collocated piezoelectric sensor/actuator for vibration control of laminated composite beams. The finite element method was used for the analysis of dynamic characteristics of laminated composite beams with piezoelectric sensor/actuator.

Wang and Wang (2000) studied the optimal design of a pair of collocated piezoelectric patch actuators that were surface bonded on various beams. The design involved selecting the optimal location and size of the piezoelectric actuators based on a controllability perspective. The definition of controllability index was adopted, which was dependent on the placement and the size of piezoelectric patches. By maximizing the index, optimal location and size of piezoelectric actuators were obtained.

Barboni et al. (2000) investigated the optimal placement of piezoelectric actuators for the control of beam vibration. The bending moment produced by a single piezoelectric actuator was evaluated by the pin-force model. Closed-form solution for harmonic forcing was obtained with explicitly accounting for the dimension and the position of the actuator.

Ip and Tse (2001) studied the optimal configuration of a piezoelectric actuator on isotropic rectangular plates. Finite element model was developed to analyze simply supported and cantilevered plates. Their results indicated that the controllability of a particular vibration mode was more sensitive to the patch location than the patch orientation. For the simply supported plate, the optimal patch positions coincided exactly with anti-nodes of the vibration modes. For the cantilevered plate, this was not true for all modes.

Bruant et al. (2001) proposed a new approach to find the optimal location of piezoelectric actuators and sensors on beam structures. The optimal locations were found separately for actuators and sensors. The actuator locations were obtained by minimizing the mechanical energy integral of the system and the sensor locations by maximizing the energy output. This method was based on the differentiation of

Charter 2 A Review on Smart Materials

the optimization criteria and equations of motion with respect to the design variables.

Damaren (2003) examined the actuator/sensor location for box type structures by the finite element method. The box was modeled as a system of joined plates in which both extensional and bending deflections were incorporated. A location criterion was developed which was based on the damping injected into the first few modes by a simple constant gain feedback. It was found that the central regions of each face which avoid the edges and corners offered the most promising sites for collocating piezoelectric actuators and sensors.

Yang et al (2003) studied the vibration control problem of a cantilevered column bonded with a piezoelectric layer. Two feedback control strategies, namely, displacement feedback control and velocity feedback control, were designed to control the vibration of the column. The analytical and semi-analytical solutions for the governing equations were deduced for these two control strategies, respectively. The vibration characteristics of a cantilevered steel column bonded with a polyvinylidene fluoride layer were computed as an example. The numerical results showed that the designed velocity feedback control method provided satisfactory vibration control by damping out the vibration of the structure with an acceptable feedback voltage, while the displacement feedback control method was unable to do this.

Wetherhold et al (2003) studied the optimization problem of directionally attached piezoelectric (DAP) actuators. The effect of the DAP actuator geometric parameters and the material properties were investigated in a systematic way for the case of a cantilevered beam. The material property study indicated the existence of an optimum point whereby the weight and cost could be lowered while improving the structural response by using a composite actuator. The actuator thickness, width, orientation angle and offset had significant effects on the structural response. The order of these parameters in terms of importance was actuator thickness, orientation angle, width and offset.

Charter 2 A Review on Smart Materials

Jin et al. (2005) proposed a fuzzy-controlled genetic-based optimization technique for optimal vibration control of cylindrical shell structures with piezoelectric sensors and actuators. The geometric variables of piezoelectric patches including the placement and size of piezoelectric sensors and actuators were processed using fuzzy set theory. The optimal distributions of piezoelectric patches based on different vibration modes were investigated.

Rather than investigating the optimal placement of sensors and actuators on time invariant structures such as beams and plates, Zhang and Erdman (2006) studied the optimal placement of sensors and actuators on flexible linkage mechanisms for active vibration control. Based on the concept of the controllability and the observability of the controlled subsystem and the residual subsystem, the objective functions were proposed aiming at the maximization of the controllability and the observability of the controlled modes and minimization of those of the residual modes. This model was solved by the modified constrained variable metric method. Numerical example supported the feasibility of the proposed method.

Qiu et al (2007) investigated the optimal placement of piezoelectric actuators on cantilevered plate for vibration suppression. The optimal placement method was developed based on the degree of observability and controllability. By using the two-order Butterworth band-pass filter and average effect of multiple piezoelectric actuators, the bending and torsional modes were decoupled. Analytical and experimental results showed that the proposed control method was feasible and the optimal placement method was effective.

Mehrabian and Yousefi-Koma (2007) presented a technique for optimal positioning of piezoelectric actuators on a smart fin structure. Neural networks were employed to find an optimal 3-dimensional surface for the frequency response function peak data obtained from a finite element model of a flexible aircraft fin. The position of a single pair of piezoelectric actuators on the fin was optimized by using the weighing factors on each of the modal surface. The proposed algorithm was able to solve the

Charter 2 A Review on Smart Materials

optimal positioning problems of sensors and actuators on different flexible smart structures.

It is seen that the literature above concentrates on the optimal placement of PZT actuators/sensors from the controllability or vibration suppression perspective. While in some applications, the optimal placement of PZT actuators in terms of maximizing the excitation is needed. However, there is very limited literature, if any, concerning this type of optimal placement. In Chapter 4 of this thesis, the optimal placement of PZT actuators is studied from the maximizing excitation perspective.

2.3 Ionic polymer-metal composites

2.3.1 History and characterizations

Compared to piezoelectric materials, IPMC is a relatively new smart material. IPMC which is also known as ionic conducting polymer gel film (ICPF) was initially found in fuel cell research. In the early 1990s, Sadeghipour et al (1992) found the sensing ability of ionic polymer. Later the converse process of charge storage mechanism associated with fuel cell, actuation capacity, was also found by Oguro's group (1992). Ever since then, the ionic polymer has been attracting more and more attention from researchers.

IPMC is a type of wet electro-active polymers (EAPs) in that salt solution is required for its actuation. As shown in Fig.2.4, an IPMC consists of a thin polyelectrolyte membrane and a type of noble metal chemically plated on both sides of the membrane. The typical polyelectrolyte membranes used in IPMC are Nafion, Flemion and Aciplex. Typical plating metals are gold, platinum and silver. Fig.2.5 illustrates the microstructure of a platinum electrode surface and Fig.2.6 shows the chemical structures of the three types of membranes.

Charter 2 A Review on Smart Materials

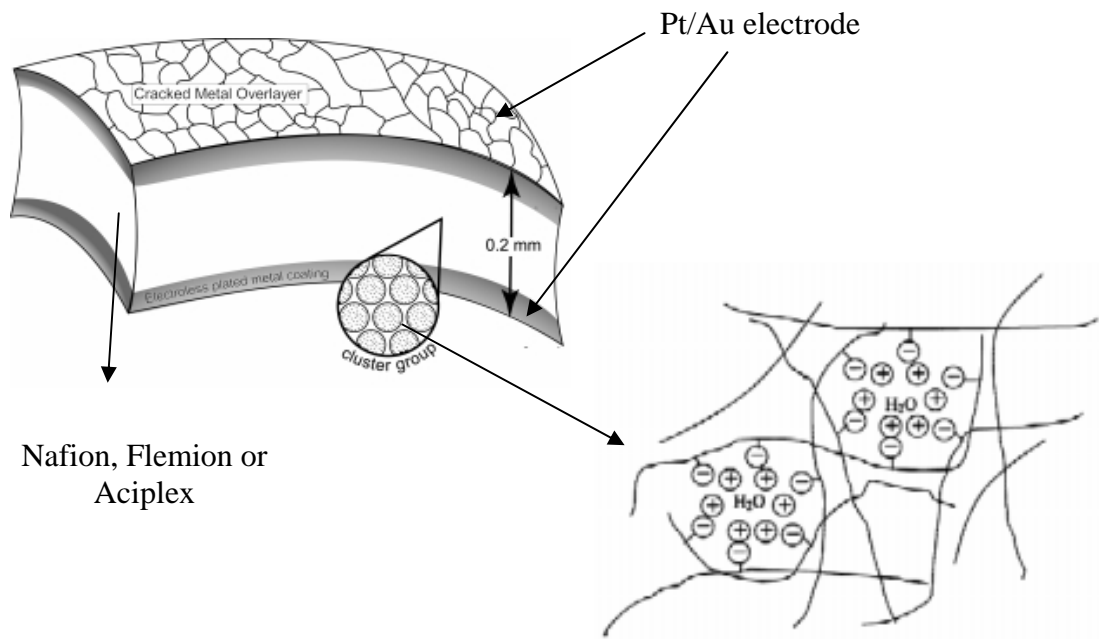


Figure 2.4 Structures of IPMC (Nemat-Nasser and Thomas, 2001)

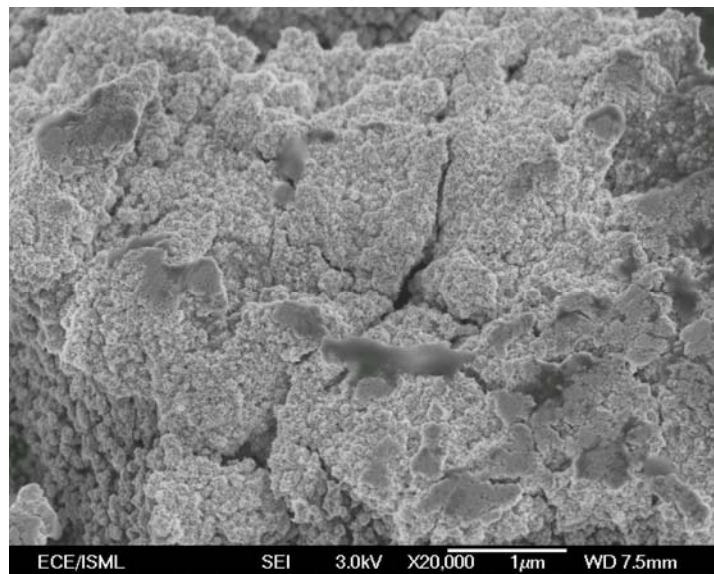


Figure 2.5 Microstructure of platinum electrode surface

Charter 2 A Review on Smart Materials

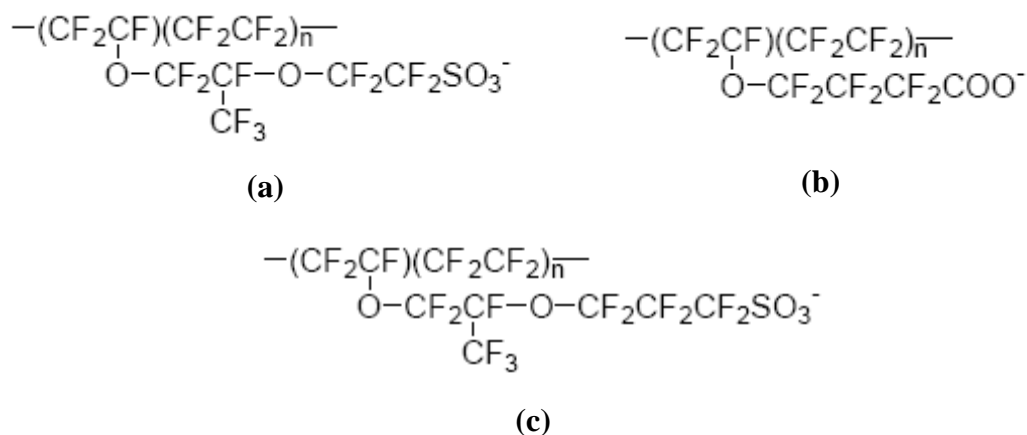


Figure 2.6 Chemical structures of polyelectrolyte membrane used in IPMCs (a) Nafion, (b) Flemion, and (c) Aciplex

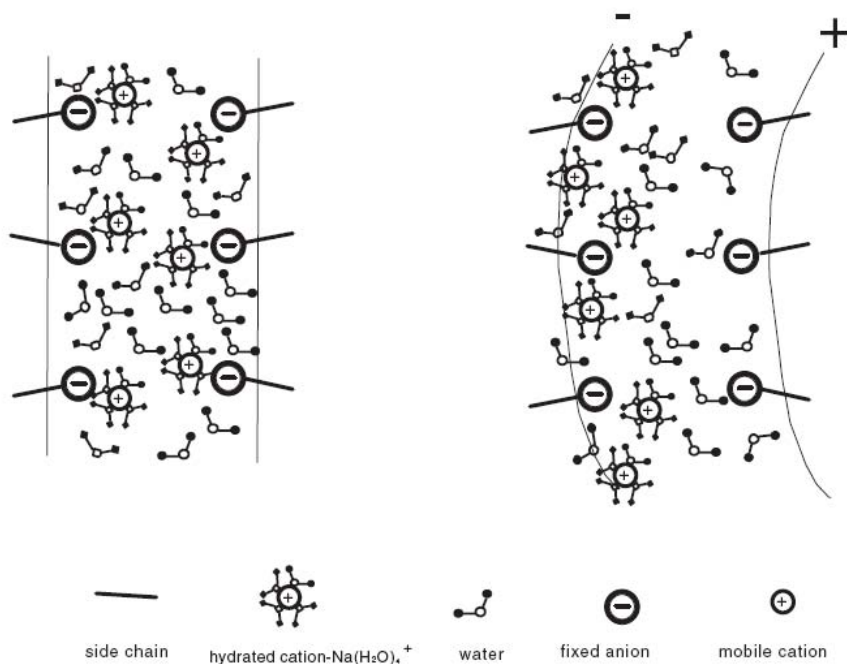


Figure 2.7 IPMC under electric potential (Shahinpoor and Kim, 2001)

As shown in Fig.2.4, the microstructures of IPMC membrane are in the form of interconnected clusters in which anions are covalently fixed to the backbone of

Charter 2 A Review on Smart Materials

polymers while cations and their associated solvent molecules are free to move within or out of clusters. Thus, when an electric potential is applied to the electrode, the free cations and associated solvent molecules will migrate under electric field, from anode to cathode. As illustrated in Fig.2.7, due to the charge redistribution process, two layers near the electrodes form, i.e., cation dominant cathode boundary layer and anion dominant anode boundary layer. Due to the imbalance of the electrostatic stresses and other chemical stresses developed within the two layers, the IPMC will bend under electric potential.

IPMC can undergo a fast and large bending motion when a low electric potential is applied to its electrodes. Conversely, IPMC can generate a measurable electric potential when it is subjected to a sudden bending. Thus, IPMC can serve as both actuators and sensors. When IPMC is subject to constant voltage, IPMC's fast bending motion is generally followed by a slow relaxation. The relaxation direction is dependent on the membrane type. For Nafion, the relaxation direction is reverse to initial bending direction while for Flemion, the relaxation is in the same direction as that of initial bending. The phenomenon could be explained by the cation charge redistribution and the following solvent diffusion within the polyelectrolyte membrane.

2.3.2 Experimental study and physical modeling

To date, the mechanism of IPMC is still uncertain. Several models have been developed based on experiments and/or theoretical analyses. These researches provide a basis for further understanding of IPMC materials.

Asaka et al (1995) experimentally studied the bending response of a solid polymer electrolyte membrane-platinum (SPM-Pt) under various electric stimuli waveforms. They represented the bending response of SPM-Pt as a function of current flow between two electrodes.

Charter 2 A Review on Smart Materials

Asaka and Oguro (2000a) proposed a kinetic model of SPM-Pt bending response. Comparisons were made between experimental results and theoretical model. Their model included the effect of the interfacial stress between the Pt electrode and the membrane. The bending behavior after the characteristic time was explained successfully by this model including the interfacial effect.

Asaka and Oguro (2000b) reported the oscillatory bending responses of SPM-Pt. The oscillations took place when the anodic oxidations of formaldehyde or sodium formate in aqueous sulfuric acid solutions happened on a plated Pt electrode. The frequency and the waveform of the oscillations were dependent on the concentration of the organic compounds and the direct current applied.

Shahinpoor and Kim (2001, 2004 and 2005) and Kim and Shahinpoor (2003) presented a series of review papers on the fundamental properties and characteristics of IPMC, manufacturing techniques, phenomenological modeling of actuation and sensing mechanism and potential applications.

Nemat-Nasser and Li (2000) presented a micromechanical model based on electrostatic interaction of ion transport. Central to their theory was the recognition that the interaction between an imbalanced charge density and the backbone polymer could be represented by an eigenstress field. Their theory was able to explain IPMC bending under electric field and also generative charges when bent. Comparisons showed a good match between theory prediction and experimental results.

Later, Nemat-Nasser (2002) studied the micromechanics of IPMC materials and proposed a nano-scale hybrid model incorporating electrostatic, osmotic and elastic effects in the actuation process. This model is able to account for both static and dynamic behavior of IPMC.

Newbury and Leo (2002) presented a linear, two-port model to represent the electromechanical transduction in ionic polymer actuators. The model parameters

Charter 2 A Review on Smart Materials

were determined by fitting the simulated responses of Laplace domain transfer functions to experimental data of Nafion based actuator.

Shahinpoor and Kim (2002) investigated the mass transfer induced actuation of IPMCs and developed a technique to minimize water leakage and to increase force density of IPMCs.

Tamagawa et al (2002) proposed a simple method to estimate the time-dependent nominal Young's moduli and generated force of IPMCs. IPMC cantilevered beams were tested. Numerical simulations validated the proposed method.

He et al (2003) established a one-dimensional variational model for IPMC in terms of electric displacement, electric field, pressure and water velocity. Variational solutions were obtained for the governing equation of charge redistribution.

Taking into account of the viscoelastic property of polymer material, Newbury and Leo (2003a) developed a linear electromechanical model based on equivalent circuit for IPMC transducers. A series of experimental tests were conducted to verify the model (Newbury and Leo, 2003b).

Nemat-Nasser and Wu (2003) carried out extensive experimental studies on IPMCs with different backbone ionomers and various cation forms. Experimental results on both Nafion and Flemion based IPMCs with alkali-metal or alkyl-ammonium cations were reported. It was observed that Flemion based IPMCs with fine dendritic gold electrodes had higher ion-exchange capacity, better surface conductivity, higher hydration capacity and higher longitudinal stiffness than Nafion based IPMCs. Under same voltage, Flemion based IPMCs displayed greater bending actuation.

Yagasaki and Tamagawa (2004) studied the viscoelastic properties of IPMCs. An experimental method was proposed to estimate the general time-dependent elastic

Charter 2 A Review on Smart Materials

moduli of IPMCs. A viscoelastic model for IPMC beam was presented and validated by experimental tests.

Farinholt and Leo (2004) presented a model for charge sensing due to imposed deformation in IPMCs. An expression for charge density, electric field and electric potential under short-circuit conditions was developed from the electrostatic field equations. This model predicted that the induced stress would produce a capacitive discharge in the polymer. Experimental results verified the basic form of the model and also demonstrated that the geometric scaling predicted in the model agreed with measured data.

Two of the primary limitations of IPMCs are unstable operation in air due to solvent vaporizing and low solvent breakdown voltage. To overcome these limitations, Bennett and Leo (2004) proposed using highly stable ionic liquids to serve as solvent of IPMC instead of commonly used water. Ionic liquids had advantages over water such as low vapor pressure and greater electrochemical stability. A 1-ethyl-3-methylimidazolium trifluoromethanesulfonate ionic liquid was used in their study. Experimental results indicated that the use of the ionic liquid improved the stability of Nafion transducers. The major limitation associated with the use of the ionic liquid was the slow speed of response compared to the case of water as solvent. Later, Akle et al (2006) studied the electrode composition for IPMCs with ionic liquid as solvent. The electrode composition was studied as a function of the surface to volume ratio and conductivity of the metal particulates. Their results showed that the surface to volume ratio of the metal particulate was critical to increasing the capacitance of the IPMC transducer. Increased conductivity of the metal particulates improved the IPMC response at frequencies higher than 10 Hz. By increasing the capacitance of IPMC, more than 2 percent strain can be achieved at voltage level of 3-volt. More recently, Bennett et al (2006) examined the mechanism of electromechanical transduction in ionic liquid-swollen Nafion based IPMCs. The morphology and relevant ion associations within the membranes were investigated by using small angle X-ray scattering, Fourier transform infrared spectroscopy and nuclear magnetic resonance spectroscopy. Results indicated that

Charter 2 A Review on Smart Materials

the ionic liquid interacted with the membrane in much the same way as water did and the counter ions of the Nafion membrane were the primary charge carriers in the ionic liquid-swollen transducers.

Bonomo et al (2005) developed a system to characterize IPMC membranes as motion sensors experimentally. The system was built to study the IPMC reaction under mechanical bending in a wide frequency range.

Toi and Kang (2005) presented a two-dimensional finite element formulation based on Galerkin method to model the electrochemical-mechanical behaviors of IPMC beams with two pairs of electrodes. The electrochemical solutions for the case of unidirectional voltages agreed well with that of one-dimensional solutions by finite difference method. The two-dimensional electrochemical response and three-dimensional deformation for bidirectional voltage were qualitatively reasonable.

Akle and Leo (2005) studied the relationship between ion conduction and electromechanical coupling of IPMC through a series of experiments on three types of ionomeric materials, Nafion, BPSH and PATS. An approximate linear correlation between the strain response of the ionomeric transducer and the capacitance of the transducer was found. This correlation was independent of polymer composition and the plating parameters. A strong relationship between surface charge accumulation and mechanical deformation in ionomeric actuators was concluded from this correlation.

Weiland and Leo (2005a) developed a computational micromechanics model to assess the impact of uniform ion distribution on spherical clusters of IPMC ionomer. They also employed a Monte Carlo style approach to study the effects of pendant chain stiffness and charge balance of the equilibrium state of a single cluster in ionic polymer (Weiland and Leo, 2005b).

Matthews et al (2006) presented a multiscale modeling approach for the prediction of material stiffness of Nafion polymer. The simulation model was developed by

Charter 2 A Review on Smart Materials

combination of traditional rotational isomeric state theory and Monte Carlo method. The probability density function was estimated and was used as an input parameter to enhance existing energetics-based models.

Nemat-Nasser and Wu (2006) presented novel methods to tailor the electromechanical response of IPMC to optimize the actuation performance. Optimal actuation activities are identified by introducing various monovalent or multivalent cations and cations combinations. Experimental results showed a good accord with the nano-scaled physical model. It was found that the bending motion could be tailored by proper changing of the time-variation function of the applied potential. For Nafion based IPMC, the initial bending towards the anode could be controlled and eliminated by linearly increasing electric potential at certain rate. The tip displacement of Flemion based IPMCs was always linearly related to the cation charge accumulation at the cathode.

More recently, Nemat-Nasser and Zanamì (2006a, 2006b) studied the effect of various solvent on the behavior of IPMC. A series of tests are conducted on both Nafion and Flemion based IPMCs with various organic solvents such as ethylene glycol, glycerol and crown ethers (Nemat-Nasser and Zanamì, 2006a). By employing these solvents, higher operation voltages and hydration rate were obtained compared to the condition under water as solvent. They could work in air for longer time and at low temperature environments. Their slow responses allowed better observation of physical characteristics of actuation process. In Nemat-Nasser and Zanamì (2006b), the nano-scale hybrid actuation model proposed by Nemat-Nasser (2002) was applied to model the initial fast motion and subsequent relaxation of Nafion based IPMCs under various solvents. The model successfully matched the experimental observations both qualitatively and quantitatively.

Charter 2 A Review on Smart Materials

2.3.3 Implemented and potential applications

Although the mechanism of IPMC has not yet been fully understood, research on applications of IPMC has attracted considerable attention from various disciplines. IPMC offers many advantages over the conventional EAP materials, such as compliance, light weight, low operation voltage and capability of working in aqueous environments. These properties make it promising for numerous applications in biomedical, naval, robotic and microelectromechanical system (MEMS) engineering.

Shahinpoor (1992) proposed of using ionic polymer gel for autonomous swimming robotic structures. A conceptual design for such structures was presented followed by a discussion on the kinematics and dynamics of such structures.

Shahinpoor and Kim (2005) presented many potential applications of IPMC such as heart compression band, four-finger gripper and artificial fish as shown in Figs.2.8-2.10, respectively.

Paquette and Kim (2004) investigated potential applications of IPMC for naval applications. Comparisons were made between IPMC and other smart materials for biomimetic propulsor applications.

Yamakita et al (2004) developed an artificial muscle linear actuator using IPMCs for biped walking robot application. The unit structure is shown in Fig.2.11. The linear actuator effectively transforms bending motion of IPMCs into longitudinal motion. More applications can be found in references Bar-Cohen (2001, 2004 and 2006) and the WorldWide Electroactive Polymer Webhub established by Dr. Bar-Cohen at <http://ndeeaa.jpl.nasa.gov/nasa-nde/lommas/eap/EAP-web.htm>.

Charter 2 A Review on Smart Materials

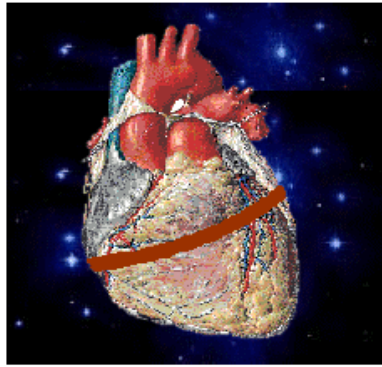


Figure 2.8 A heart with IPMC compression band (Shahinpoor and Kim, 2004)

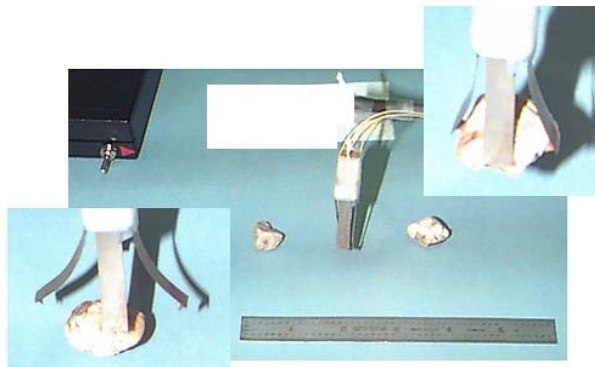


Figure 2.9 Four-finger gripper (Shahinpoor and Kim, 2004)

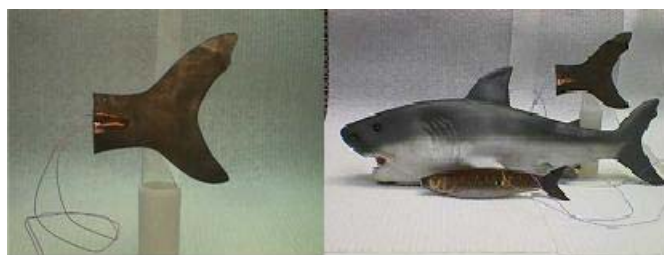


Figure 2.10 Artificial fish (Shahinpoor and Kim, 2004)

Charter 2 A Review on Smart Materials

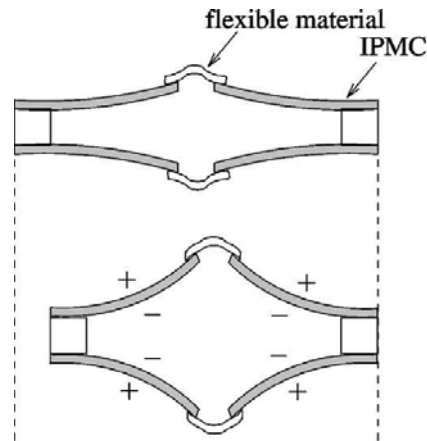


Figure 2.11 An IPMC linear actuator (Yamakita et al, 2004)

2.4 Concluding Remarks

This chapter gives a general review of smart materials, focusing on piezoelectric materials and IPMCs. Fundamentals of piezoelectricity theory, research on piezoelectric actuators, actuator-structure interaction and optimal placements of actuators have been presented. Research development on the mechanism of IPMC actuation and sensing and its applications were reviewed.

It is evident that both of the two types of smart materials, piezoelectric materials and ionic polymer-metal composites, have the ability to serve as sensors and actuators. In this thesis, the two kinds of smart materials are studied by focusing on their actuation properties. Potential biomedical applications of the two EAMs are discussed and prototype models are developed. Chapter 3 and 4 will present the actuation characteristics of piezoelectric materials bonded on plate and shell structures and Chapter 5 and 6 will concentrate on the dynamic behaviors of IPMCs and their potential applications in biomedical engineering.

Chapter 3 Modeling of Piezoelectric Material Actuated Plate and Shell

3.1 Introduction

As discussed in Chapter 2, most of previous researches on piezoelectric actuated structures have been concentrated on beam and plate vibration control. However, in many engineering applications, plates are frequently placed on elastic media which can be viewed as elastic foundations, and they are subjected to in-plane forces due to the assembly process. For such a plate subject to in-plane forces bonded on an elastic foundation with surface-bonded piezoelectric actuators, no report has been found in the existing literature.

In this chapter, piezoelectric materials actuated structures are studied. The piezoelectric material considered is PZT ceramic which is assumed to be perfectly bonded on the surface of structures by epoxy. The host structures are the simply supported pre-stressed plate and cylindrical shell bonded on elastic foundation. By applying alternative electric potentials, the structures are excited leading to vibration at driving frequency. The dynamic behaviors of plate and shell under piezoelectric actuation are studied. Analytical solutions are obtained to account for the transverse vibration of the plate and shell. In-plane vibration of plate is also investigated by finite difference method. Calculation examples are provided for better illustration.

Charter 3 Modeling of Piezoelectric Material Actuated Plate and Shell

3.2 Piezoelectric actuated plate

3.2.1 Problem formulation

Fig.3.1 shows a rectangular plate with length a , width b and thickness h , bonded on an elastic foundation. It is bonded with a PZT actuator of thickness h_p on the surface. The PZT actuator is assumed to be perfectly bonded and its stiffness is neglected due to its limited contribution to the dynamic behavior of the plate. x , y and z are the global coordinates defined in the mid-plane of the plate and ξ and η are the normalized coordinates in xy plane.

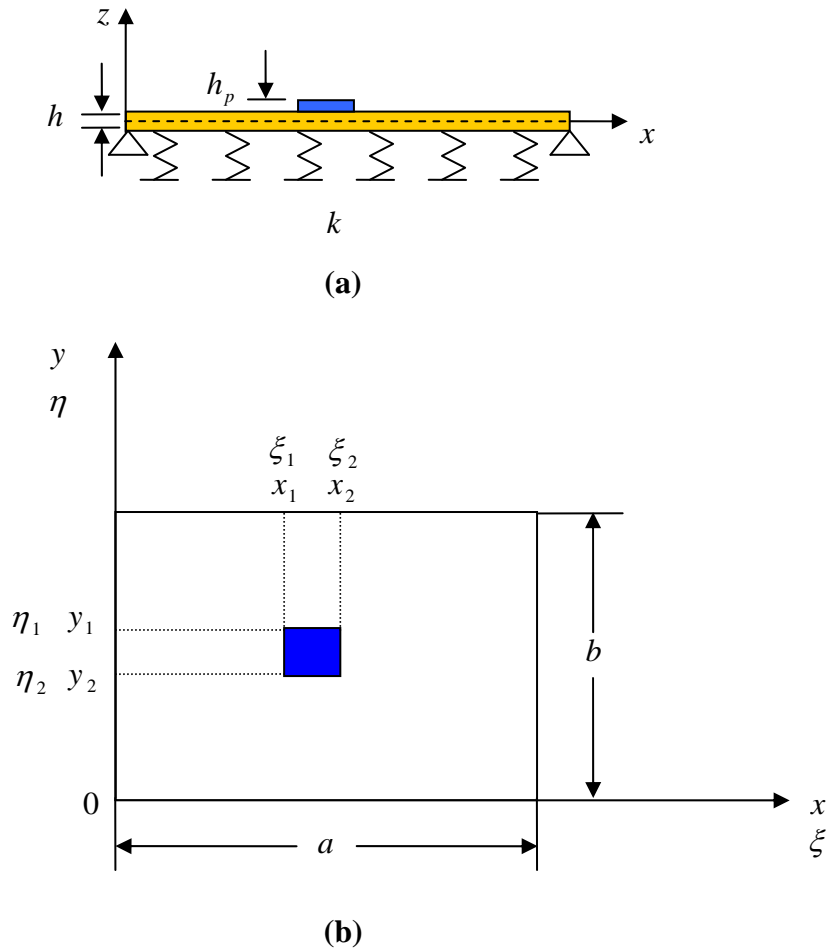


Figure 3.1 (a) Plate and PZT actuator system (b) Plate and PZT actuator coordinate system

Charter 3 Modeling of Piezoelectric Material Actuated Plate and Shell

The governing equation of the plate vibration can be obtained by the Hamiltonian energy principle, which can be expressed as

$$\delta \int_{t_0}^{t_1} (U - K - W) dt = 0 \quad (3.1)$$

where U is the strain energy; K is the kinetic energy and W is the work done by external forces.

Under the plane stress condition, the constitutive relations of the plate are

$$\begin{bmatrix} \sigma_{xx} \\ \sigma_{yy} \\ \sigma_{xy} \end{bmatrix} = \frac{E}{1-\nu^2} \begin{bmatrix} 1 & \nu & 0 \\ \nu & 1 & 0 \\ 0 & 0 & 1-\nu \end{bmatrix} \begin{bmatrix} \varepsilon_{xx} \\ \varepsilon_{yy} \\ \varepsilon_{xy} \end{bmatrix} \quad (3.2)$$

where σ_{xx} , σ_{yy} and σ_{xy} are the normal stress in the x direction, normal stress in the y direction and shear stress in the xy plane, respectively; ε_{xx} , ε_{yy} and ε_{xy} are the corresponding normal and shear strains; E is the Young's modulus of the plate; and ν is the Poisson's ratio of the plate.

The strain-displacement relations of von Karman's plate theory (Rao, 1999) are,

$$\begin{bmatrix} \varepsilon_{xx} \\ \varepsilon_{yy} \\ \varepsilon_{xy} \end{bmatrix} = \begin{bmatrix} \frac{\partial u}{\partial x} - z \frac{\partial^2 w}{\partial x^2} + \frac{1}{2} \left(\frac{\partial w}{\partial x} \right)^2 \\ \frac{\partial v}{\partial y} - z \frac{\partial^2 w}{\partial y^2} + \frac{1}{2} \left(\frac{\partial w}{\partial y} \right)^2 \\ \frac{\partial u}{\partial y} + \frac{\partial v}{\partial x} - 2z \frac{\partial^2 w}{\partial x \partial y} + \frac{\partial w}{\partial x} \frac{\partial w}{\partial y} \end{bmatrix} \quad (3.3)$$

where u , v and w are the displacements of mid-plane of the plate in the x , y and z directions, respectively.

Charter 3 Modeling of Piezoelectric Material Actuated Plate and Shell

Hence, the strain energy can be expressed as

$$U = \iiint_V \frac{1}{2} (\sigma_{xx} \varepsilon_{xx} + \sigma_{yy} \varepsilon_{yy} + \sigma_{xy} \varepsilon_{xy}) dx dy dz \quad (3.4)$$

The kinetic energy in this problem is

$$K = \iint_S \frac{1}{2} \rho h \left[\left(\frac{\partial u}{\partial t} \right)^2 + \left(\frac{\partial v}{\partial t} \right)^2 + \left(\frac{\partial w}{\partial t} \right)^2 \right] dx dy \quad (3.5)$$

where ρ is the material density of the plate.

The work done by external load, including the contribution of the PZT actuator, the material damping, the elastic foundation and the in-plane tensile forces can be expressed as

$$W = - \iint_S [(q_1(x, y, t)u + q_2(x, y, t)v + q_3(x, y, t)w + c \frac{\partial w}{\partial t} w + \frac{1}{2} kw^2] dx dy \\ - \oint N_x^0 \frac{\partial u}{\partial x} dl - \oint N_y^0 \frac{\partial v}{\partial y} dl \quad (3.6)$$

where $q_1(x, y, t)$, $q_2(x, y, t)$ and $q_3(x, y, t)$ are the loads applied by the PZT actuator in the x , y and z directions, respectively; c is the plate damping per unit area; k is the stiffness of elastic foundation; N_x^0 and N_y^0 are the in-plane tensile forces per unit length in the x and y directions, respectively.

Substituting the variations of the above energies into Eq.(3.1), and integrating by parts, the governing equation can be derived as

$$-\frac{Eh}{1-\nu^2} \frac{\partial^2 u}{\partial x^2} - \frac{Eh}{2(1+\nu)} \frac{\partial^2 u}{\partial y^2} - \frac{Eh}{2(1-\nu)} \frac{\partial^2 v}{\partial x \partial y} + \rho h \frac{\partial^2 u}{\partial t^2} = -q_1(x, y, t) \quad (3.7)$$

Charter 3 Modeling of Piezoelectric Material Actuated Plate and Shell

$$-\frac{Eh}{1-\nu^2} \frac{\partial^2 v}{\partial y^2} - \frac{Eh}{2(1+\nu)} \frac{\partial^2 v}{\partial x^2} - \frac{Eh}{2(1-\nu)} \frac{\partial^2 u}{\partial x \partial y} + \rho h \frac{\partial^2 v}{\partial t^2} = -q_2(x, y, t) \quad (3.8)$$

$$\begin{aligned} D \nabla^4 w - \frac{\partial}{\partial x} (N_x \frac{\partial w}{\partial x}) - \frac{\partial}{\partial y} (N_y \frac{\partial w}{\partial y}) - \frac{\partial}{\partial y} (N_{xy} \frac{\partial w}{\partial x}) + \frac{\partial}{\partial x} (N_{xy} \frac{\partial w}{\partial y}) \\ + \rho h \frac{\partial^2 w}{\partial t^2} + c \frac{\partial w}{\partial t} + kw = -q_3(x, y, t) \end{aligned} \quad (3.9)$$

where $D = Eh^3/[12(1-\nu^2)]$ is the bending rigidity of the plate; $N_x = \int_{-h/2}^{h/2} \sigma_{xx} dz$, $N_y = \int_{-h/2}^{h/2} \sigma_{yy} dz$ and $N_{xy} = \int_{-h/2}^{h/2} \sigma_{xy} dz$ are the stress resultants in the x , y and xy directions, respectively; and the in-plane forces $q_1(x, y, t)$ and $q_2(x, y, t)$ applied by the PZT actuator are,

$$q_1(x, y, t) = -E_p d_{31} V(t) [\delta(x - x_1) - \delta(x - x_2)] \cdot [H(y - y_1) - H(y - y_2)] \quad (3.10)$$

$$q_2(x, y, t) = -E_p d_{31} V(t) [H(x - x_1) - H(x - x_2)] \cdot [\delta(y - y_1) - \delta(y - y_2)] \quad (3.11)$$

where E_p is the Young's modulus of the PZT actuator; d_{31} is the piezoelectric constant; $V(t)$ is the voltage applied on the PZT actuator; x_1, x_2, y_1 and y_2 are the coordinates of the four corners of the PZT actuator, as shown in Fig.1(a); $\delta(\cdot)$ is the Dirac delta function defined as

$$\delta(x - a) = \begin{cases} \infty & x = a \\ 0 & \text{else} \end{cases} ; \quad (3.12)$$

$H(\cdot)$ is the Heaviside function defined as

$$H(x - a) = \begin{cases} 0 & x < a \\ 1 & x \geq a \end{cases} ; \quad (3.13)$$

Charter 3 Modeling of Piezoelectric Material Actuated Plate and Shell

$q_3(x, y, t) = \frac{\partial^2 M_{px}}{\partial x^2} + \frac{\partial^2 M_{py}}{\partial y^2}$ with M_{px} and M_{py} being the moments applied by the

PZT actuator which can be expressed as

$$M_{px} = -E_p d_{31} V(t) \frac{h_p + h}{2} [H(x - x_1) - H(x - x_2)] \cdot [H(y - y_1) - H(y - y_2)] \quad (3.14)$$

$$M_{py} = -E_p d_{31} V(t) \frac{h_p + h}{2} [H(y - y_1) - H(y - y_2)] \cdot [H(x - x_1) - H(x - x_2)] \quad (3.15)$$

Since the transverse vibration is the main concern of this study, by assuming that the plate is subject to constant in-plane forces as $N_x = N_x^0$, $N_y = N_y^0$ and $N_{xy} = 0$, Eq.(3.9) can be simplified as

$$D \nabla^4 w - N_x^0 \frac{\partial^2 w}{\partial x^2} - N_y^0 \frac{\partial^2 w}{\partial y^2} + \rho h \frac{\partial^2 w}{\partial t^2} + c \frac{\partial w}{\partial t} + k w = -q_3(x, y, t) \quad (3.16)$$

Following the non-dimensionalizing procedure as in Gorman (1982), Eq.(3.16) can be normalized by letting $\xi = \frac{x}{a}$, $\eta = \frac{y}{b}$ and $\beta = \frac{a}{b}$,

$$\begin{aligned} & \frac{\partial^4 w}{\partial \xi^4} + 2\beta^2 \frac{\partial^4 w}{\partial \xi^2 \partial \eta^2} + \beta^4 \frac{\partial^4 w}{\partial \eta^4} - a^2 \frac{N_x^0}{D} \frac{\partial^2 w}{\partial \xi^2} - a^2 \beta^2 \frac{N_y^0}{D} \frac{\partial^2 w}{\partial \eta^2} \\ & + a^4 \frac{\rho h}{D} \frac{\partial^2 w}{\partial t^2} + a^4 \frac{c}{D} \frac{\partial w}{\partial t} + a^4 \frac{k}{D} w = -a^4 \frac{q_3(\xi, \eta, t)}{D} \end{aligned} \quad (3.17)$$

where

$$\begin{aligned} q_3(\xi, \eta, t) &= \frac{\partial^2 M_{p\xi}}{a^2 \partial \xi^2} + \frac{\beta^2 \partial^2 M_{p\eta}}{a^2 \partial \eta^2} \\ &= \frac{-E_p d_{31} V(t) (h_p + h)}{2a^2} \{ [\delta'(\xi - \xi_1) - \delta'(\xi - \xi_2)] \cdot [H(\eta - \eta_1) - H(\eta - \eta_2)] \\ & \quad + \beta^2 [\delta'(\eta - \eta_1) - \delta'(\eta - \eta_2)] \cdot [H(\xi - \xi_1) - H(\xi - \xi_2)] \} \end{aligned} \quad (3.18)$$

Charter 3 Modeling of Piezoelectric Material Actuated Plate and Shell

where ξ_1, ξ_2, η_1 and η_2 are the normalized coordinates of the four corners of the PZT actuator as shown in Fig.1(a); and $\delta'(\cdot)$ is the derivative of the Dirac delta function.

The governing equation of Eq.(3.17) is applicable to all thin plates regardless of the boundary conditions. In the next section, the solution of Eq.(3.17) for a simply supported plate will be presented.

3.2.2 Analytical solution

Eq.(3.17) can be solved by the method of separation of variables. In this method, the solution can be assumed as the product of a function of position $\Phi(\xi, \eta)$ and a function of time $f(t)$. For a simply supported plate, the solution can be expressed as

$$w(\xi, \eta, t) = \sum_{n=1}^{\infty} \sum_{m=1}^{\infty} \sin(m\pi\xi) \sin(n\pi\eta) f_{mn}(t) \quad (3.19)$$

Substituting the solution into Eq.(3.17), multiplying both sides with

$$\int_0^1 \int_0^1 \sin(m^* \pi \xi) \sin(n^* \pi \eta) d\xi d\eta \text{ and using the mode orthogonality namely,}$$

$$\int_0^1 \int_0^1 \sin(m\pi\xi) \sin(n\pi\eta) \sin(m^* \pi \xi) \sin(n^* \pi \eta) d\xi d\eta = \begin{cases} \frac{1}{4} & m = m^*, n = n^* \\ 0 & \text{else} \end{cases} \quad (3.20)$$

we have

$$\ddot{f}_{m^* n^*}(t) + \frac{c}{\rho h} \dot{f}_{m^* n^*}(t) + \frac{ka^4 + (D \cdot (m^{*4} \pi^4 + 2\beta^2 m^{*2} n^{*2} \pi^4 + \beta^4 n^{*4} \pi^4) + a^2 N_x^0 m^{*2} \pi^2 + a^2 \beta^2 N_y^0 n^{*2} \pi^2)}{a^4 \rho h} f_{m^* n^*}(t) = -\frac{4}{\rho h} \int_0^1 \int_0^1 q_3(\xi, \eta, t) \sin(m^* \pi \xi) \sin(n^* \pi \eta) d\xi d\eta \quad (3.21)$$

Charter 3 Modeling of Piezoelectric Material Actuated Plate and Shell

Letting $m = m^*$, $n = n^*$, $\Omega = \frac{c}{2\rho h}$,

$$\omega_{mn}^2 = \frac{1}{a^4 \rho h} [ka^4 + D \cdot (m^4 \pi^4 + 2\beta^2 m^2 n^2 \pi^4 + \beta^4 n^4 \pi^4) + (a^2 N_x^0 m^2 \pi^2 + a^2 \beta^2 N_y^0 n^2 \pi^2)] \quad (3.22)$$

and

$$Q_{mn}(\xi, \eta, t) = -\frac{4}{\rho h} \int_0^1 \int_0^1 q_3(\xi, \eta, t) \sin(m\pi\xi) \sin(n\pi\eta) d\xi d\eta \quad (3.23)$$

Eq.(3.21) can be rewritten in a simple form as

$$\ddot{f}_{mn}(t) + 2\Omega \dot{f}_{mn}(t) + \omega_{mn}^2 f_{mn}(t) = Q_{mn}(\xi, \eta, t) \quad (3.24)$$

where ω_{mn} is the natural frequency of plate and $Q_{mn}(\xi, \eta, t)$ represents the excitation force provided by the PZT actuator.

The homogeneous solution to Eq.(3.24) is

$$f_{mn}^h(t) = \begin{cases} C_1 e^{(-\Omega - \sqrt{\Omega^2 - \omega_{mn}^2})t} + C_2 e^{(-\Omega + \sqrt{\Omega^2 - \omega_{mn}^2})t} & \Omega^2 - \omega_{mn}^2 \neq 0 \\ (C_1 + C_2 t) e^{-\Omega t} & \Omega^2 - \omega_{mn}^2 = 0 \end{cases} \quad (3.25)$$

If the PZT actuator is driven by a sinusoidal voltage, i.e., $V(t) = V_0 \sin(\omega t)$ and thus

$Q_{mn}(\xi, \eta, t) = Q_{mn}(\xi, \eta) \sin(\omega t)$, the particular solution can be written as

$$f_{mn}^p(t) = C_3 \sin(\omega t) + C_4 \cos(\omega t) \quad (3.26)$$

where ω is the angular driving frequency of the PZT actuator.

Substituting Eq.(3.26) into Eq.(3.24), we can obtain

Charter 3 Modeling of Piezoelectric Material Actuated Plate and Shell

$$f_{mn}^p(t) = R_{mn} \sin \omega t + \frac{2R_{mn}\Omega\omega}{\omega^2 - \omega_{mn}^2} \cos \omega t \quad (3.27)$$

where

$$R_{mn} = \frac{Q_{mn}(\xi, \eta)}{\omega_{mn}^2 - \omega^2 + 4\Omega^2\omega^2/(\omega_{mn}^2 - \omega^2)} \quad (3.28)$$

Substituting $f_{mn}(t) = f_{mn}^h(t) + f_{mn}^p(t)$ into Eq.(3.24) and incorporating the initial conditions of the problem shown below,

$$f_{mn}|_{t=0} = 0, \quad \frac{df_{mn}}{dt}|_{t=0} = 0 \quad (3.29)$$

C_1 and C_2 can be determined as

$$C_1 = \frac{-\omega Q_{mn}(\xi, \eta)}{2\sqrt{\Omega^2 - \omega_{mn}^2} (2\Omega^2 + \omega^2 - \omega_{mn}^2 + 2\Omega\sqrt{\Omega^2 - \omega_{mn}^2})} \quad (3.30)$$

$$C_2 = \frac{\omega Q_{mn}(\xi, \eta)}{2\sqrt{\Omega^2 - \omega_{mn}^2} (2\Omega^2 + \omega^2 - \omega_{mn}^2 - 2\Omega\sqrt{\Omega^2 - \omega_{mn}^2})} \quad (3.31)$$

Thus, the final solution $f_{mn}(t) = f_{mn}^h(t) + f_{mn}^p(t)$ can be obtained from Eqs.(3.25), (3.27), (3.28), (3.30) and (3.31).

If the damping of plate is negligible, i.e., $c = 0$, we have $\Omega = 0$, thus $\Omega^2 - \omega_{mn}^2 < 0$.

For this case, the plate deflection can be obtained as

$$w = \sum_{n=1}^{\infty} \sum_{m=1}^{\infty} \sin(m\pi\xi) \sin(n\pi\eta) \frac{Q_{mn}(\xi, \eta)}{\omega_{mn}^2 - \omega^2} \left[\sin \omega t - \frac{\omega}{\omega_{mn}} \sin \omega_{mn} t \right] \quad (3.32)$$

The steady-state response of the deflection is

Charter 3 Modeling of Piezoelectric Material Actuated Plate and Shell

$$w = \sum_{n=1}^{\infty} \sum_{m=1}^{\infty} \sin(m\pi\xi) \sin(n\pi\eta) \frac{Q_{mn}(\xi, \eta)}{\omega_{mn}^2 - \omega^2} \sin \omega t \quad (3.33)$$

From Eqs.(3.18) and (3.23), $Q_{mn}(\xi, \eta)$ in Eq.(3.33) is

$$\begin{aligned} Q_{mn}(\xi, \eta) = & \frac{-4M_0}{a^2 \rho h} \int_0^1 \int_0^1 \{ [\delta'(\xi - \xi_1) - \delta'(\xi - \xi_2)] \cdot [H(\eta - \eta_1) - H(\eta - \eta_2)] \\ & + \beta^2 [\delta'(\eta - \eta_1) - \delta'(\eta - \eta_2)] \cdot [H(\xi - \xi_1) - H(\xi - \xi_2)] \} \\ & \sin(m\pi\xi) \sin(n\pi\eta) d\xi d\eta \end{aligned} \quad (3.34)$$

where $M_0 = -E_p d_{31} V_0 (h_p + h) / 2$

After integration, we obtain

$$Q_{mn}(\xi, \eta) = \frac{4M_0}{a^2 \rho h} \left(\frac{m}{n} + \frac{n\beta^2}{m} \right) (\cos(m\pi\xi_2) - \cos(m\pi\xi_1)) (\cos(n\pi\eta_2) - \cos(n\pi\eta_1)) \quad (3.35)$$

By using the trigonometric formulas, the expression of the modal force can be transformed as

$$Q_{mn}(\xi, \eta) = \frac{16M_0}{a^2 \rho h} \left(\frac{m}{n} + \frac{n\beta^2}{m} \right) \sin(m\pi\xi_0) \sin(n\pi\eta_0) \sin(m\pi \cdot r_\xi) \sin(n\pi \cdot r_\eta) \quad (3.36)$$

where $\xi_0 = (\xi_1 + \xi_2) / 2$, $\eta_0 = (\eta_1 + \eta_2) / 2$, $r_\xi = (\xi_2 - \xi_1) / 2$ and $r_\eta = (\eta_2 - \eta_1) / 2$.

It is noted that ξ_0 and η_0 are the coordinates of the center of PZT actuator in the $\xi \eta$ plane and r_ξ and r_η are the half dimensions of PZT actuator in the ξ and η directions, respectively.

Therefore the steady-state solution to Eq.(3.17) with negligible plate damping is

Charter 3 Modeling of Piezoelectric Material Actuated Plate and Shell

$$w = \sum_{n=1}^{\infty} \sum_{m=1}^{\infty} \frac{16M_0}{a^2 \rho h} \frac{\sin \omega t}{\omega_{mn}^2 - \omega^2} \left(\frac{m}{n} + \frac{n\beta^2}{m} \right) \sin(m\pi\xi_0) \sin(n\pi\eta_0) \sin(m\pi \cdot r_{\xi}) \sin(n\pi \cdot r_{\eta}) \sin(m\pi\xi) \sin(n\pi\eta) \quad (3.37)$$

If $N_x^o = N_y^o = 0$ and $k = 0$, Eq.(3.37) remains unchanged in form, which is the steady solution to the forced vibration of a simply supported plate without the in-plane forces and elastic foundation. However, the natural frequency in Eq.(3.37) becomes $\omega_{mn}^2 = D(m^4\pi^4 + 2\beta^4 m^2 n^2 \pi^2 + \beta^4 n^4 \pi^4)/(a^4 \rho h)$, which is identical with Leissa's formula (Leissa, 1973). This result implicitly validates our solution.

3.2.3 Illustrative example

With the solution shown in Eq.(3.37), we can obtain the plate deflection at any specified time. Figs. 3.2 and 3.3 depict the deflections of a rectangular plate with $a=0.15m$ and $\beta=1.5$ excited by one PZT actuator at two different locations on the plate. The upper limits of m and n in Eq.(3.37) are set to be $m=50$ and $n=50$. The upper limits are chosen according to the convergence study as shown in Fig. 3.4. Figs. 3.2 and 3.3 are plotted at the time when the sinusoidal electric potential reaches its maximum value of 10 volts. The in-plane tensile force is $N_x^0 = N_y^0 = 10$ N/m and the foundation stiffness is $k = 7 \times 10^9$ N/m³. The material properties used in the calculation are listed in Table 3.1.

Table 3.1 Material properties and constants for plate and PZT

	Young's Modulus (N/m ²)	Material density (kg/m ³)	Poisson's ratio	Dimension (mm)	Electric potential (V)	d_{31} (m/V)
Plate	7.03×10^{10}	2700	0.34	$a = 150$ $h = 2$	N.A.	N.A.

Charter 3 Modeling of Piezoelectric Material Actuated Plate and Shell

PZT	7.94×10^{10}	N.A.	0.30	$l_{px} = 0.1a$ $l_{py} = 0.1a\beta$ $h_p = 0.2$	10	-1.3×10^{-10}
-----	-----------------------	------	------	--	----	------------------------

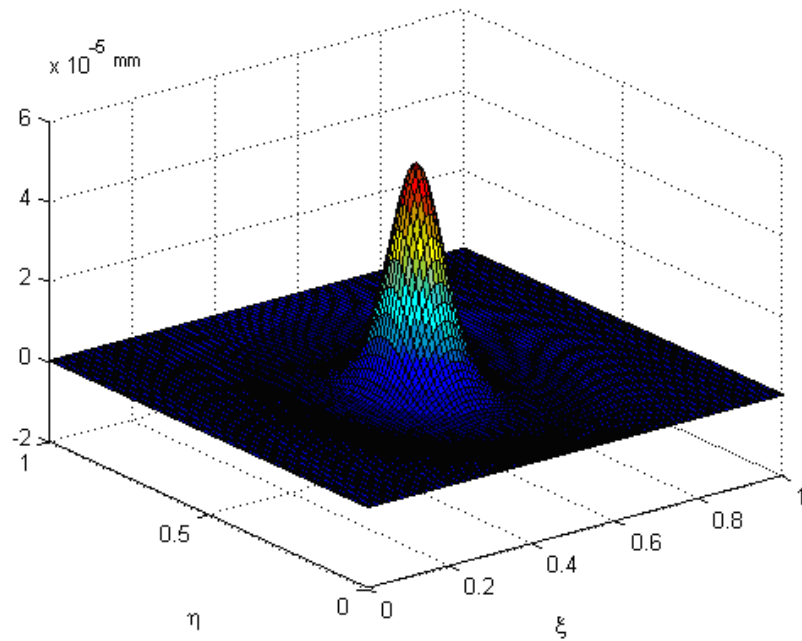


Figure 3.2 Deflection of rectangular plate actuated by one PZT actuator at center ($\omega=18849.6$ rad/s)

Charter 3 Modeling of Piezoelectric Material Actuated Plate and Shell

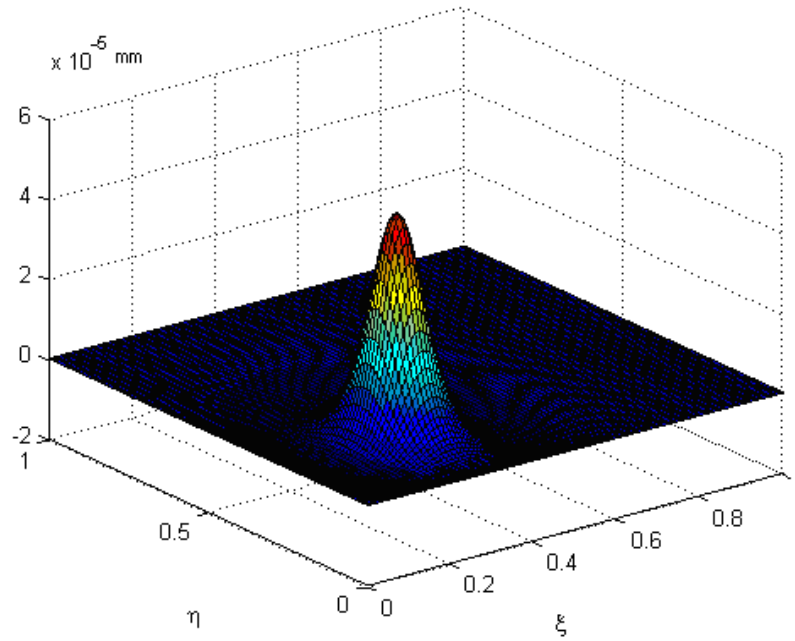


Figure 3.3 Deflection of rectangular plate actuated by one PZT actuator at $(\xi=\eta=0.3)$ ($\omega=18849.6$ rad/s)

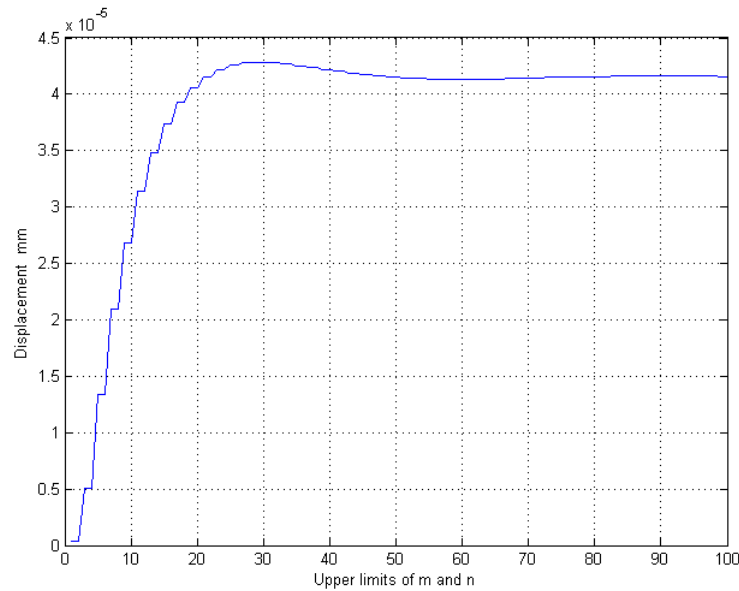


Figure 3.4 Convergence of Eq.(3.37) vs m and n

After obtaining the transverse displacement solution of plate, the pressure generated by plate on the elastic foundation can be obtained by integrating the foundation's reactions within the region of the plate area.

Charter 3 Modeling of Piezoelectric Material Actuated Plate and Shell

$$F = \int_0^1 \int_0^1 k \cdot w \cdot H(-w) d\xi d\eta \quad (3.38)$$

Substituting Eq.(3.37) into the Eq.(3.38), we obtain

$$F = \int_0^1 \int_0^1 k \cdot \sum_{n=1}^{\infty} \sum_{m=1}^{\infty} \frac{16M_0}{a^2 \rho h} \frac{\sin \omega t}{\omega_{mn}^2 - \omega^2} \left(\frac{m}{n} + \frac{n\beta^2}{m} \right) \sin(m\pi\xi_0) \sin(n\pi\eta_0) \sin(m\pi \cdot r_{\xi}) \sin(n\pi \cdot r_{\eta}) \sin(m\pi\xi) \sin(n\pi\eta) H(-w) d\xi d\eta \quad (3.39)$$

Integrating Eq.(3.39), we obtain

$$F = k \cdot \sum_{n=1}^{\infty} \sum_{m=1}^{\infty} \frac{16M_0}{a^2 \rho h} \frac{\sin \omega t}{\omega_{mn}^2 - \omega^2} \left(\frac{m}{n} + \frac{n\beta^2}{m} \right) \sin(m\pi\xi_0) \sin(n\pi\eta_0) \sin(m\pi \cdot r_{\xi}) \sin(n\pi \cdot r_{\eta}) \int_0^1 \int_0^1 \sin(m\pi\xi) \sin(n\pi\eta) H(-w) d\xi d\eta \quad (3.40)$$

Letting $\varsigma_{nm} = \int_0^1 \int_0^1 \sin(m\pi\xi) \sin(n\pi\eta) H(-w) d\xi d\eta$, Eq.(3.40) can be transformed as

$$F = k \cdot \sum_{n=1}^{\infty} \sum_{m=1}^{\infty} \frac{16M_0}{a^2 \rho h} \frac{\sin \omega t}{\omega_{mn}^2 - \omega^2} \left(\frac{m}{n} + \frac{n\beta^2}{m} \right) \sin(m\pi\xi_0) \sin(n\pi\eta_0) \sin(m\pi \cdot r_{\xi}) \sin(n\pi \cdot r_{\eta}) \varsigma_{nm} \quad (3.41)$$

Eq.(3.41) can be used to calculate the overall force generated by the plate on the elastic foundation with one PZT actuator. For example as shown in Fig.3.2, the total force generated is about 0.072 N. This small magnitude of generated force is due to the small deflection of the aluminum plate.

3.2.4 In-plane vibration of piezoelectric actuated plate

Compared to the much attention devoted to the transverse vibration of piezoelectric actuated plates in literature, relatively limited research has been done on in-plane

Charter 3 Modeling of Piezoelectric Material Actuated Plate and Shell

vibration due to piezoelectric actuation. Because of the coupling between the displacements in two orthogonal directions, solution of in-plane vibration can not be obtained in a closed-form. Therefore, in this section, the finite difference method is employed to solve the partial differential equations of in-plane vibration.

The in-plane vibration of the plate actuated by a piezoelectric actuator is governed by the hyperbolic partial differential equations as described in Eqs.(3.7) and (3.8).

Extracting the terms of $\partial^2(\cdot)/\partial t^2$, Eqs.(3.7) and (3.8) can be transformed as,

$$\frac{\partial^2 u}{\partial t^2} = \frac{E}{\rho(1-\nu^2)} \frac{\partial^2 u}{\partial x^2} + \frac{E}{2\rho(1+\nu)} \frac{\partial^2 u}{\partial y^2} + \frac{E}{2\rho(1-\nu)} \frac{\partial^2 v}{\partial x \partial y} + \frac{q_1(x, y, t)}{\rho h} \quad (3.42)$$

$$\frac{\partial^2 v}{\partial t^2} = \frac{E}{\rho(1-\nu^2)} \frac{\partial^2 v}{\partial y^2} + \frac{E}{2\rho(1+\nu)} \frac{\partial^2 v}{\partial x^2} + \frac{E}{2\rho(1-\nu)} \frac{\partial^2 u}{\partial x \partial y} + \frac{q_2(x, y, t)}{\rho h} \quad (3.43)$$

Fig.3.5 shows the central finite difference meshes used for this problem.

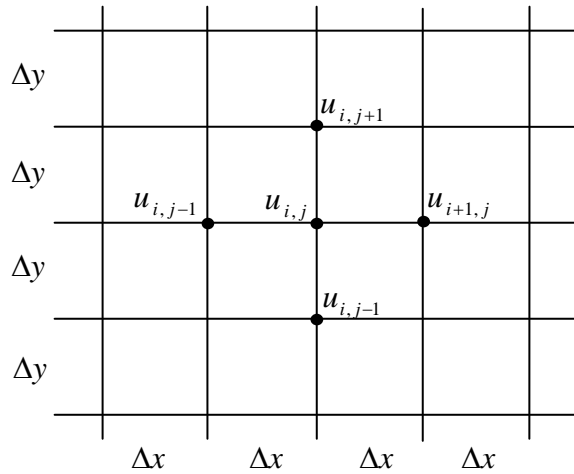


Figure 3.5 Central finite difference meshes

Assuming that the mesh size in both directions are equal, i.e., $\Delta x = \Delta y = \lambda$, the partial differential terms can be expressed as

Charter 3 Modeling of Piezoelectric Material Actuated Plate and Shell

$$\begin{aligned}
 \frac{\partial^2 u}{\partial x^2} &= \frac{u_{i+1,j}^k + u_{i-1,j}^k - 2u_{i,j}^k}{\lambda^2}, \quad \frac{\partial^2 u}{\partial y^2} = \frac{u_{i,j+1}^k + u_{i,j-1}^k - 2u_{i,j}^k}{\lambda^2} \\
 \frac{\partial^2 v}{\partial x^2} &= \frac{v_{i+1,j}^k + v_{i-1,j}^k - 2v_{i,j}^k}{\lambda^2}, \quad \frac{\partial^2 v}{\partial y^2} = \frac{v_{i,j+1}^k + v_{i,j-1}^k - 2v_{i,j}^k}{\lambda^2} \\
 \frac{\partial^2 u}{\partial x \partial y} &= \frac{(u_{i-1,j+1}^k + u_{i+1,j-1}^k) - (u_{i-1,j-1}^k + u_{i+1,j+1}^k)}{4\lambda^2} \\
 \frac{\partial^2 v}{\partial x \partial y} &= \frac{(v_{i-1,j+1}^k + v_{i+1,j-1}^k) - (v_{i-1,j-1}^k + v_{i+1,j+1}^k)}{4\lambda^2} \\
 \frac{\partial^2 u}{\partial t^2} &= \frac{u_{i,j}^{k+1} + u_{i,j}^{k-1} - 2u_{i,j}^k}{\Delta t^2}, \quad \frac{\partial^2 v}{\partial t^2} = \frac{v_{i,j}^{k+1} + v_{i,j}^{k-1} - 2v_{i,j}^k}{\Delta t^2}
 \end{aligned} \tag{3.44}$$

Using Eq.(3.44), Eqs.(3.42) and (3.43) can be discretized as

$$\begin{aligned}
 \frac{u_{i,j}^{k+1} + u_{i,j}^{k-1} - 2u_{i,j}^k}{(\Delta t)^2} &= \frac{E}{\rho(1-\nu^2)} \frac{u_{i+1,j}^k + u_{i-1,j}^k - 2u_{i,j}^k}{\lambda^2} \\
 &+ \frac{E}{2\rho(1+\nu)} \frac{u_{i,j+1}^k + u_{i,j-1}^k - 2u_{i,j}^k}{\lambda^2} + \\
 &\frac{E}{2\rho(1-\nu)} \frac{(v_{i-1,j+1}^k + v_{i+1,j-1}^k) - (v_{i-1,j-1}^k + v_{i+1,j+1}^k)}{4\lambda^2} \\
 &- \frac{E_p d_{31} V}{\rho h} [\delta(i\lambda - x_1) - \delta(i\lambda - x_2)] \cdot [H(j\lambda - y_2) - H(j\lambda - y_1)] \sin \omega k \Delta t
 \end{aligned} \tag{3.45}$$

$$\begin{aligned}
 \frac{v_{i,j}^{k+1} + v_{i,j}^{k-1} - 2v_{i,j}^k}{(\Delta t)^2} &= \frac{E}{\rho(1-\nu^2)} \frac{v_{i,j+1}^k + v_{i,j-1}^k - 2v_{i,j}^k}{\lambda^2} \\
 &+ \frac{E}{2\rho(1+\nu)} \frac{v_{i+1,j}^k + v_{i-1,j}^k - 2v_{i,j}^k}{\lambda^2} + \\
 &\frac{E}{2\rho(1-\nu)} \frac{(u_{i-1,j+1}^k + u_{i+1,j-1}^k) - (u_{i-1,j-1}^k + u_{i+1,j+1}^k)}{4\lambda^2} \\
 &- \frac{E_p d_{31} V}{\rho h} [\delta(j\lambda - y_1) - \delta(j\lambda - y_2)] \cdot [H(i\lambda - x_2) - H(i\lambda - x_1)] \sin \omega k \Delta t
 \end{aligned} \tag{3.46}$$

From Eqs.(3.45) and (3.46), $u_{i,j}^{k+1}$ and $v_{i,j}^{k+1}$ can be derived as,

Charter 3 Modeling of Piezoelectric Material Actuated Plate and Shell

$$\begin{aligned}
 u_{i,j}^{k+1} = & \frac{E}{\rho(1-\nu^2)} \frac{(\Delta t)^2}{\lambda^2} (u_{i+1,j}^k + u_{i-1,j}^k - 2u_{i,j}^k) \\
 & + \frac{E}{2\rho(1+\nu)} \frac{(\Delta t)^2}{\lambda^2} (u_{i,j+1}^k + u_{i,j-1}^k - 2u_{i,j}^k) \\
 & + \frac{E}{8\rho(1-\nu)} \frac{(\Delta t)^2}{\lambda^2} (v_{i-1,j+1}^k + v_{i+1,j-1}^k - v_{i-1,j-1}^k - v_{i+1,j+1}^k) \\
 & - \frac{E_p d_{31} V (\Delta t)^2}{\rho h} [\delta(i\lambda - x_1) - \delta(i\lambda - x_2)] \cdot [H(j\lambda - y_2) - H(j\lambda - y_1)] \sin \omega k \Delta t \\
 & - u_{i,j}^{k-1} + 2u_{i,j}^k
 \end{aligned} \tag{3.47}$$

$$\begin{aligned}
 v_{i,j}^{k+1} = & \frac{E}{\rho(1-\nu^2)} \frac{(\Delta t)^2}{\lambda^2} (v_{i,j+1}^k + v_{i,j-1}^k - 2v_{i,j}^k) \\
 & + \frac{E}{2\rho(1+\nu)} \frac{(\Delta t)^2}{\lambda^2} (v_{i+1,j}^k + v_{i-1,j}^k - 2v_{i,j}^k) \\
 & + \frac{E}{8\rho(1-\nu)} \frac{(\Delta t)^2}{\lambda^2} (u_{i-1,j+1}^k + u_{i+1,j-1}^k - u_{i-1,j-1}^k - u_{i+1,j+1}^k) \\
 & - \frac{E_p d_{31} V (\Delta t)^2}{\rho h} [\delta(j\lambda - y_1) - \delta(j\lambda - y_2)] \cdot [H(i\lambda - x_2) - H(i\lambda - x_1)] \sin \omega k \Delta t \\
 & - v_{i,j}^{k-1} + 2v_{i,j}^k
 \end{aligned} \tag{3.48}$$

The initial and boundary conditions of this problem can be expressed as

$$u_{i,j}^0 = u_{i,j}^1 = 0; \text{ and } u_{i,j}^k = 0 \quad \text{for nodes on the boundaries.} \tag{3.49}$$

The first condition is not strict in that $u_{i,j}^1$ is not equal to zero in fact. However, because both the velocity and acceleration are unknown, this approximate condition is applied. In addition, when the vibration becomes steady, the effect of the approximation would be negligible.

These system equations of Eqs.(3.47) and (3.48) have been investigated by Alterman and Loewenthal (1972) who showed that for stability the following relation applied

Charter 3 Modeling of Piezoelectric Material Actuated Plate and Shell

$$\frac{\Delta t}{\lambda} \leq \left[\frac{E(3-\nu)}{2\rho(1-\nu^2)} \right]^{-1/2} \quad (3.50)$$

The physical meaning of this requirement is that the in-plane wave shall not be able to propagate across one mesh spacing in less than one time step. The right hand side of Eq.(3.50) is the inverse of the wave velocity.

By using Eqs.(3.47)-(3.50), the in-plane vibration of the piezoelectric actuated plate illustrated in the previous section is calculated. The parameters are the same as listed in Table 3.1. Figs. 3.6 and 3.7 show the results of in-plane vibration in the x and y directions, respectively. Fig.3.8 illustrates the in-plane displacement field of the piezoelectric actuated plate with contour plot. It is observed from the results that the amplitude of in-plane vibration is in the order of 10^{-11} m, which is much smaller than that of transverse vibration which is in the order of 10^{-8} m. Therefore, the in-plane vibration of plate can be neglected.

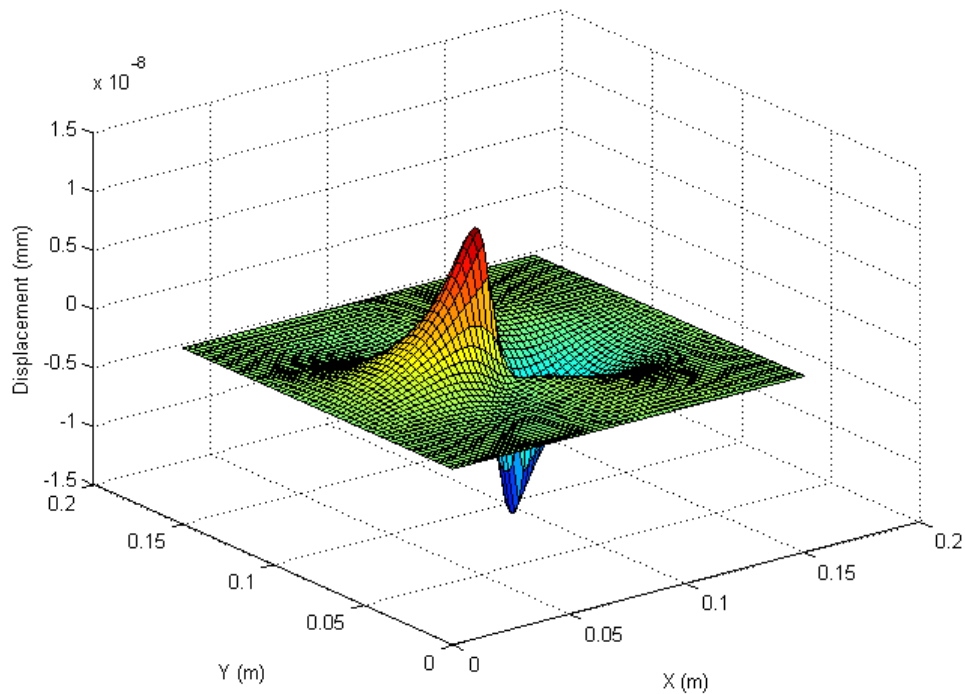


Figure 3.6 In-plane displacement of plate in x direction

Charter 3 Modeling of Piezoelectric Material Actuated Plate and Shell

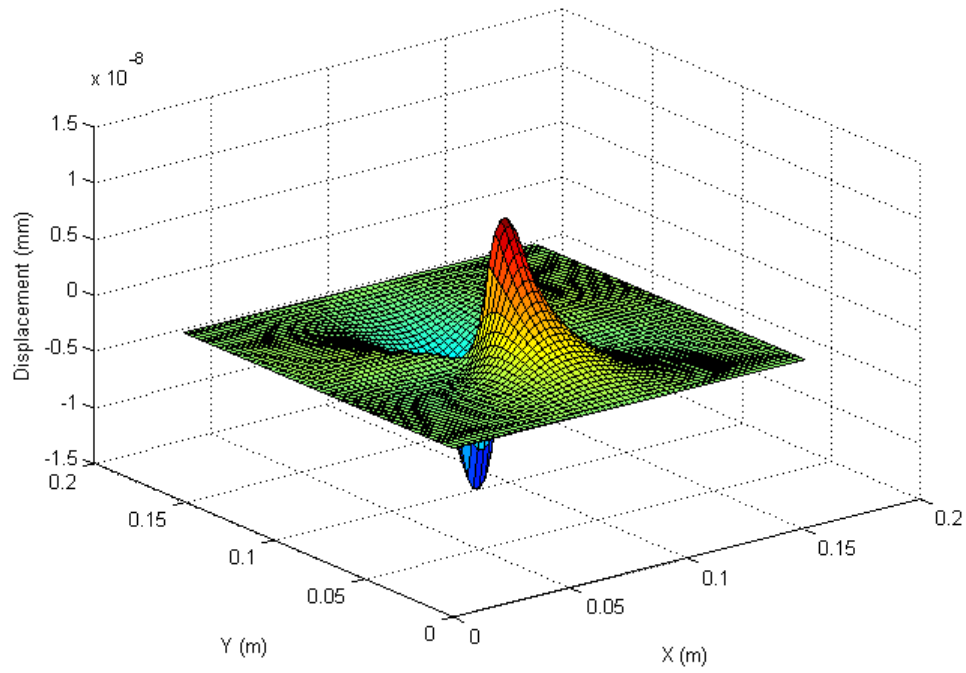


Figure 3.7 In-plane displacement of plate in y direction

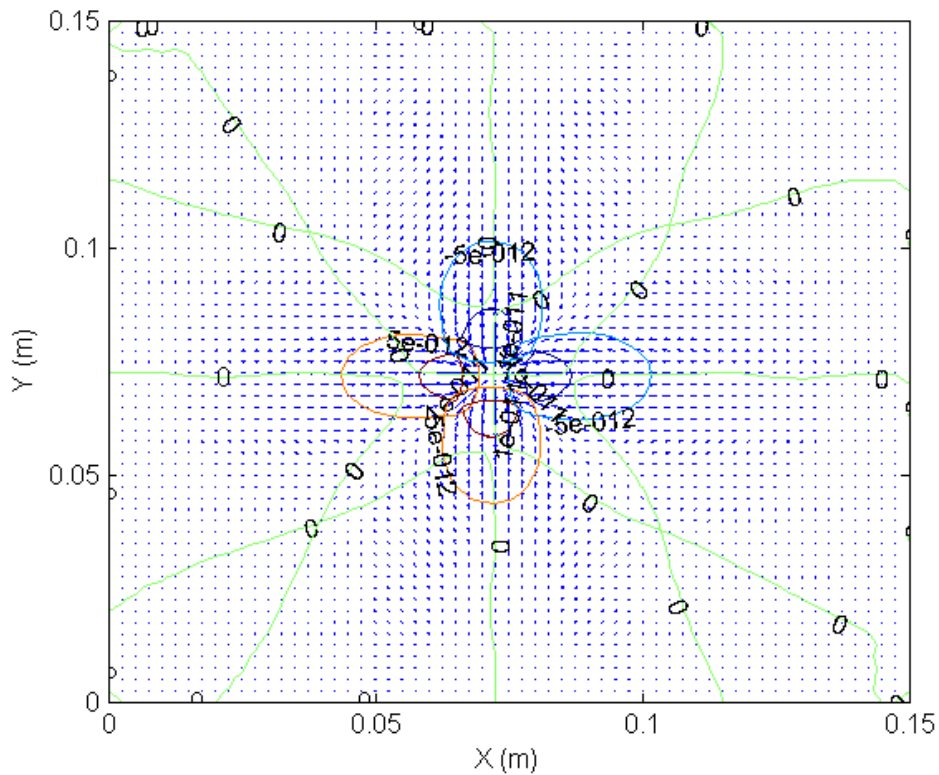


Figure 3.8 In-plane displacement field of plate with contour plot

Charter 3 Modeling of Piezoelectric Material Actuated Plate and Shell

3.3 Vibration of piezoelectric actuated cylindrical shell

After solving the vibration problem of piezoelectric actuated plate, the formulation and solution procedure can be readily extended to piezoelectric actuated shell structures.

Consider a thin cylindrical shell segment of length L , radius R , total cutout angle Φ and thickness h . The shell is bonded on an elastic foundation with stiffness of k and bonded with a pair of collocated PZT actuators with length l_p , width $R\theta_p$ and thickness h_p , which are driven by equal but opposite electric fields. The PZT actuators are assumed to be small and perfectly bonded, thus their stiffness are neglected.

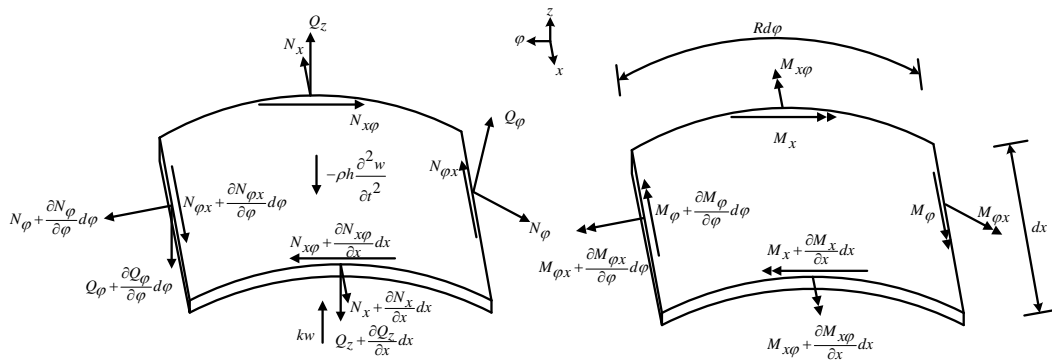


Figure 3.9 Stress resultants on a shell element

Fig.3.9 illustrates the stress resultants acting on a differential element of the cylindrical shell, where Q_x and Q_ϕ are the shear force resultants of shear stresses τ_{xz} and $\tau_{\phi z}$, respectively; N_x , N_ϕ and $N_{x\phi}$ are the membrane forces in the x , ϕ and $x\phi$ directions, respectively; w is the transverse displacement of the shell; ρ is the material density; t is time; and M_x , $M_{x\phi}$ and M_ϕ are the bending moments in

Charter 3 Modeling of Piezoelectric Material Actuated Plate and Shell

the φz plane, twisting moment in the $x\varphi$ plane and bending moment in the zx plane, respectively.

According to the equilibrium of the shell element in the radial direction, we have

$$R \frac{\partial Q_x}{\partial x} + \frac{\partial Q_\varphi}{\partial \varphi} + N_\varphi - R\rho h \frac{\partial^2 w}{\partial t^2} - Rkw = 0 \quad (3.51)$$

$$Q_x = \frac{\partial M_x}{\partial x} + \frac{1}{R} \frac{\partial M_{\varphi x}}{\partial \varphi} \quad (3.52)$$

$$Q_\varphi = -\frac{\partial M_{x\varphi}}{\partial x} + \frac{1}{R} \frac{\partial M_\varphi}{\partial \varphi} \quad (3.53)$$

Substituting Eqs.(3.52) and (3.53) into Eq.(3.51) and considering that the moments M_x and M_φ , and the force N_φ should include the contribution of the PZT actuators bonded on the shell, we can obtain

$$\begin{aligned} R \frac{\partial^2 (M_x - M_x^a)}{\partial x^2} + 2 \frac{\partial^2 M_{\varphi x}}{\partial \varphi \partial x} + \frac{1}{R} \frac{\partial^2 (M_\varphi - M_\varphi^a)}{\partial \varphi^2} + N_\varphi - N_\varphi^a \\ - R\rho h \frac{\partial^2 w}{\partial t^2} - Rkw = 0 \end{aligned} \quad (3.54)$$

where M_x^a , M_φ^a and N_φ^a are the bending moments and in-plane force provided by the PZT actuators. Since the PZTs are collocated and driven by opposite and equal electric fields, the membrane force $N_\varphi^a = 0$.

Using the Donnell-Mushtari's shell theory (Markus, 1988) and considering the displacement relation for pure bending, $u = -z \frac{\partial w}{\partial x}$ and $v = -\frac{z}{R} \frac{\partial w}{\partial \varphi}$, the motion equation can be obtained from Eq.(3.54) as

Charter 3 Modeling of Piezoelectric Material Actuated Plate and Shell

$$\begin{aligned}
 & R^2 \frac{\partial^4 w}{\partial x^4} + 2 \frac{\partial^4 w}{\partial x^2 \partial \varphi^2} + \frac{1}{R^2} \frac{\partial^4 w}{\partial \varphi^4} - \frac{\nu}{2} \frac{\partial^2 w}{\partial x^2} + \frac{6}{h^2} w + \frac{R^2}{2D} \rho h \frac{\partial^2 w}{\partial t^2} + \frac{R^2}{2D} k w \\
 & = -\frac{R^2}{2D} F_r
 \end{aligned} \tag{3.55}$$

where $F_r = \frac{\partial^2 M_x^a}{\partial x^2} + \frac{1}{R^2} \frac{\partial^2 M_\varphi^a}{\partial \varphi^2}$; $D = \frac{Eh^2}{12(1-\nu^2)}$; E and ν are the Young's modulus

and Poisson's ratio of the shell, respectively. Letting $x = \xi L$ and $\varphi = \theta \Phi$, Eq.(3.55) can be normalized as

$$\begin{aligned}
 & \frac{R^2}{L^4} \frac{\partial^4 w}{\partial \xi^4} + \frac{2}{L^2 \Phi^2} \frac{\partial^4 w}{\partial \xi^2 \partial \theta^2} + \frac{1}{R^2 \Phi^4} \frac{\partial^4 w}{\partial \theta^4} - \frac{2\nu}{L^2} \frac{\partial^2 w}{\partial \xi^2} + \frac{6}{h^2} w + \frac{R^2}{2D} \rho h \frac{\partial^2 w}{\partial t^2} + \frac{R^2}{2D} k w \\
 & = -\frac{R^2}{2D} \bar{F}_r
 \end{aligned} \tag{3.56}$$

where

$$\bar{F}_r = \frac{\partial^2 M_\xi^a}{L^2 \partial \xi^2} + \frac{1}{R^2 \Phi^2} \frac{\partial^2 M_\theta^a}{\partial \theta^2} \tag{3.57}$$

and

$$M_\xi^a = 2M_\xi^* [H(\xi - \xi_1) - H(\xi - \xi_2)] \cdot [H(\theta - \theta_1) - H(\theta - \theta_2)] e^{i\omega t} \tag{3.58}$$

$$M_\theta^a = 2M_\theta^* [H(\theta - \theta_1) - H(\theta - \theta_2)] \cdot [H(\xi - \xi_1) - H(\xi - \xi_2)] e^{i\omega t} \tag{3.59}$$

where M_ξ^* and M_θ^* are the amplitudes of distributed moments in the x and φ directions, respectively, which can be expressed as $M^a = M_\xi^* = M_\theta^* = E_p d_{31} V (h_p + h) / 2$, where E_p is the Young's modulus of PZT actuators; d_{31} is the piezoelectric constant; V is the voltage applied on the PZT actuators; ω is the angular frequency of the electric field; ξ_1 , ξ_2 , θ_1 and θ_2 are the normalized coordinates of the four corners of the PZT actuators.

Charter 3 Modeling of Piezoelectric Material Actuated Plate and Shell

Eq.(3.56) can also be solved by the method of separation of variables. For the simply supported shell, the solution can be expressed as

$$w = \sum_{m=1}^{\infty} \sum_{n=1}^{\infty} C_{mn} \sin(m\pi\xi) \sin(n\pi\theta) e^{i\omega t} \quad (3.60)$$

Substituting Eq.(3.60) into Eq.(3.56), multiplying both sides by $\sin(m^*\pi\xi)\sin(n^*\pi\theta)$ and integrating on the shell domain, the solution to Eq.(3.56) is obtained as

$$w = \sum_{m=1}^{\infty} \sum_{n=1}^{\infty} \frac{4B_{mn} \sin(n\pi\theta_0) \sin(m\pi\xi_0)}{\omega_{mn}^2 - \omega^2} \sin(m\pi\xi) \sin(n\pi\theta) e^{i\omega t} \quad (3.61)$$

where $\omega_{mn}^2 = \frac{2D}{\rho h} [(\frac{m^2\pi^2}{L^2} + \frac{n^2\pi^2}{R^2\Phi^2})^2 + \frac{2\nu m^2\pi^2}{R^2L^2} + \frac{6}{R^2h^2} + k]$ is the natural frequency

of the shell; $B_{mn} = \frac{4M^a}{\rho h} (\frac{m}{nL^2} + \frac{n}{mR^2\Phi^2}) \sin(m\pi\frac{l_\xi}{2}) \sin(n\pi\frac{\theta_p}{2})$; $\xi_0 = (\xi_1 + \xi_2)/2$;

$\theta_0 = (\theta_1 + \theta_2)/2$; $l_\xi = \xi_2 - \xi_1$; and $\theta_p = \theta_2 - \theta_1$.

Eq.(3.61) is the solution of the radial displacement of the cylindrical shell actuated by a pair of collocated piezoelectric actuators. It is evident that Eq.(3.61) has the same form as Eq.(3.37).

Fig. 3.10 shows the deformation of cylindrical shell actuated by a pair of collocated PZT actuators located at the center of the shell. The radial displacement is in the order of 10^{-3} mm.

Charter 3 Modeling of Piezoelectric Material Actuated Plate and Shell

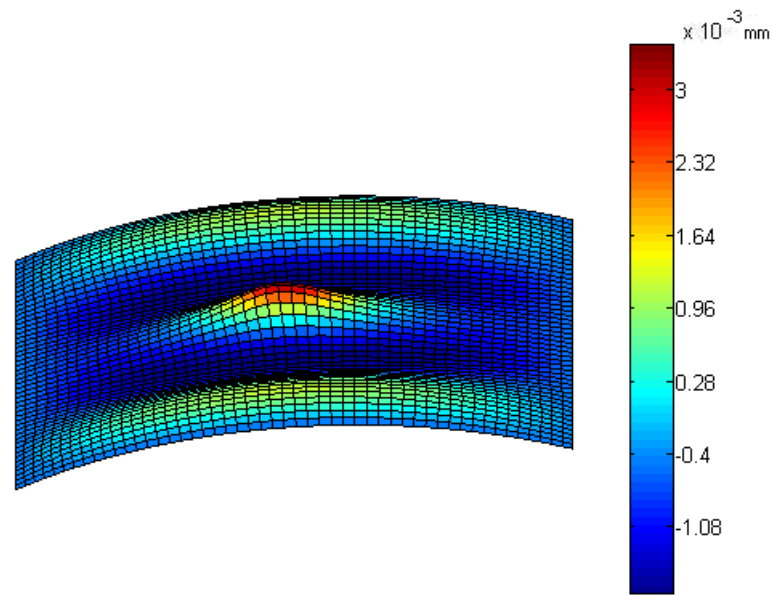


Figure 3.10 Deformation of cylindrical shell segment actuated by a pair of PZT actuators at center ($\omega = 5155$ rad/s)

Table 3.2 Material properties and constants for shell and PZT

	Young's Modulus (N/m ²)	Material density (kg/m ³)	Poisson's ratio	Dimension (mm)	Electric potential (V)	d_{31} (m/V)
Shell	7.03×10^{10}	2700	0.34	$L = 500$ $R = 1000$ $\Phi = \pi / 3$ $h = 2$	N.A.	N.A.
PZT	7.94×10^{10}	N.A.	0.30	$l_p = 50$ $\theta_p = \pi / 30$ $h_p = 0.5$	10	-1.3×10^{-10}

Chapter 3 Modeling of Piezoelectric Material Actuated Plate and Shell

3.4 Conclusions

In this chapter, a simply supported plate subject to in-plane forces, bonded on an elastic foundation and excited by a PZT actuator was investigated. Analytical solution was obtained to predict the deflection of the plate. The pressure generated on the elastic foundation was evaluated. The in-plane vibration was also studied by finite difference method. It was observed that the in-plane vibration was negligible compared to the transverse vibration. The formulation and solution procedures were applied to a simply supported cylindrical shell actuated by a pair of collocated PZT actuators. Closed form solution was obtained.

The vibration solutions obtained in this chapter will be used to investigate the optimal placement of PZT actuators on plate and shell in Chapter 4.

Chapter 4 Optimal placement of piezoelectric actuators on plate and shell

4.1 Introduction

In Chapter 3, the vibration responses of plates and shells actuated by piezoelectric actuators were obtained. The concern in this chapter is how to optimally place the actuators on the host structures. Appropriate placement of actuators would promote system efficiency, improve controllability and observability as well as save materials and energy. As discussed in Chapter 2, previous researches on optimal placement of sensors and actuators have focused on beam and plate vibration control. In certain applications, excitation of vibration is desirable, such as loud speakers and piezoelectric buzzers. Therefore, it is meaningful to study the optimal placement of actuators from the perspective of maximizing the plate vibration. However, in the literature, this kind of optimal placements of PZT actuators has received little attention.

In this chapter, the optimal placement of the PZT actuator in terms of maximizing the plate and shell vibration is studied based on the analytical solutions obtained in Chapter 3. The effect of PZT actuator's dimensions is also discussed. A simple yet general procedure to determine the optimal excitation locations of the PZT actuator is presented.

4.2 Optimal placement of PZT actuator on plate

In this chapter, the optimal placement of the PZT actuator in terms of maximizing the plate deflection is of interest. When the electric potential reaches its maximum

Chapter 4 Optimal placement of piezoelectric actuators on plate and shell

value, the maximum plate deflection may be positive or negative. To eliminate this effect, the absolute value of plate deflection $|w|$ is considered.

A computer program has been developed to calculate the plate deflection according to Eq.(3.37). In the calculation, a 19×19 grid is used to represent the PZT locations. The PZT actuator can be located at any grid node. At each location of the PZT actuator, the maximum deflection of plate is calculated. After obtaining the maximum deflections corresponding to all the 361 PZT actuator locations, the relationship between the maximum plate deflection and PZT actuator locations can be revealed. The parameters used in calculation are listed in Table 3.1.

4.2.1 Driving frequencies close to natural frequencies

- **Numerical results of PZT optimal locations**

Fig.4.1 shows the results when the driving frequencies are close to the resonant/natural frequencies of first nine vibration modes. The driving frequencies are set to be 5 Hz less than the natural frequencies. The contour plots in Fig.4.1 illustrate the relationship between the maximum plate deflection and the PZT actuator location. This relationship is associated with the optimal location pattern of the PZT actuator. For a specific PZT actuator location, the maximum plate deflection is represented by the color of this location which can be read through the color bar. Fig.4.2 shows the first nine vibration mode shapes with the absolute values of mode shapes being adopted. Comparing Fig.4.1 with Fig.4.2, it can be observed that the pattern of optimal location of the PZT actuator with driving frequency close to the natural frequency of mode (m,n) is identical with the vibration mode shape (m,n) , for $m,n \in \{1,2,3\}$.

Chapter 4 Optimal placement of piezoelectric actuators on plate and shell

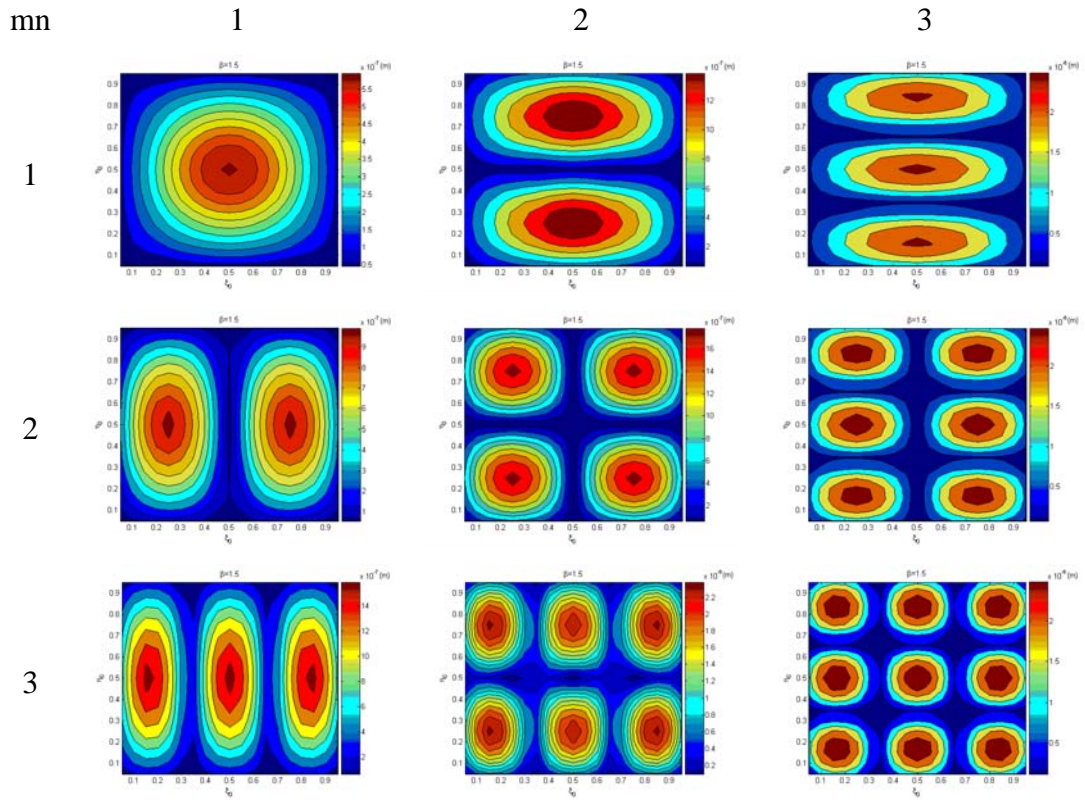
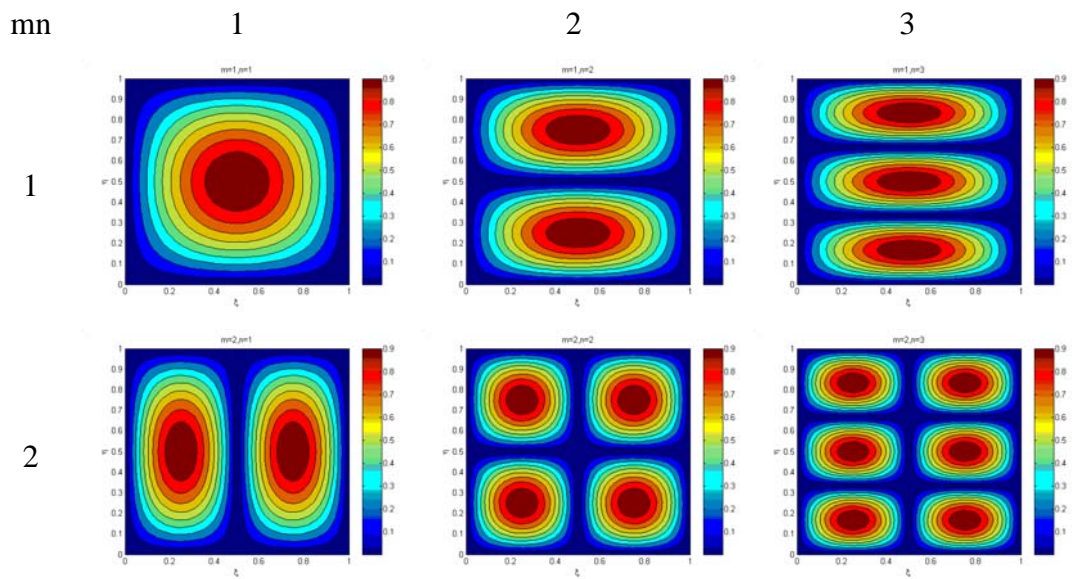


Figure 4.1 Optimal location patterns of a PZT actuator on a rectangular plate with $\beta = 1.5$ at driving frequencies close to natural frequencies



Chapter 4 Optimal placement of piezoelectric actuators on plate and shell

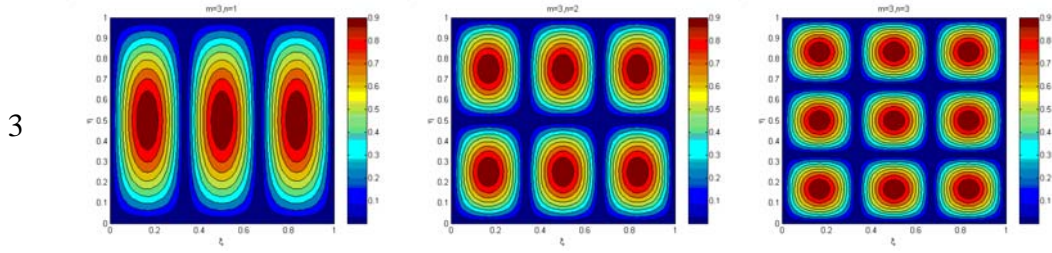


Figure 4.2 First nine mode shapes of rectangular plate

- Combined position mode function (CPMF)

The process of finding the optimal locations of the PZT actuator is essentially equivalent to maximizing the plate deflection $|w|$ by altering the four variables ξ_0, η_0, ξ and η , the values of which can be determined by the following equations,

$$\frac{\partial w}{\partial \xi_0} = \sum_{n=1}^{\infty} \sum_{m=1}^{\infty} A_{mn} m\pi \cos(m\pi\xi_0) \sin(n\pi\eta_0) \sin(m\pi\xi) \sin(n\pi\eta) = 0 \quad (4.1)$$

$$\frac{\partial w}{\partial \eta_0} = \sum_{n=1}^{\infty} \sum_{m=1}^{\infty} A_{mn} n\pi \sin(m\pi\xi_0) \cos(n\pi\eta_0) \sin(m\pi\xi) \sin(n\pi\eta) = 0 \quad (4.2)$$

$$\frac{\partial w}{\partial \xi} = \sum_{n=1}^{\infty} \sum_{m=1}^{\infty} A_{mn} m\pi \sin(m\pi\xi_0) \sin(n\pi\eta_0) \cos(m\pi\xi) \sin(n\pi\eta) = 0 \quad (4.3)$$

$$\frac{\partial w}{\partial \eta} = \sum_{n=1}^{\infty} \sum_{m=1}^{\infty} A_{mn} n\pi \sin(m\pi\xi_0) \sin(n\pi\eta_0) \sin(m\pi\xi) \cos(n\pi\eta) = 0 \quad (4.4)$$

where $A_{mn} = \frac{16M_0}{a^2 \rho h} \frac{\sin \omega t}{\omega_{mn}^2 - \omega^2} \left(\frac{m}{n} + \frac{n\beta^2}{m} \right) \sin(m\pi \cdot r_\xi) \sin(n\pi \cdot r_\eta)$.

Subtracting Eq.(4.1) from Eq.(4.3), and Eq.(4.2) from Eq.(4.4), we obtain

$$\sum_{n=1}^{\infty} \sum_{m=1}^{\infty} A_{mn} m\pi \sin(n\pi\eta_0) \sin(n\pi\eta) \sin(m\pi(\xi - \xi_0)) = 0 \quad (4.5)$$

Chapter 4 Optimal placement of piezoelectric actuators on plate and shell

$$\sum_{n=1}^{\infty} \sum_{m=1}^{\infty} A_{mn} n\pi \sin(m\pi\xi_0) \sin(m\pi\xi) \sin(n\pi(\eta - \eta_0)) = 0 \quad (4.6)$$

Since $\sin(n\pi\eta_0)$ and $\sin(n\pi\eta)$ should not be zero when $|w|$ reaches maximum, it is evident that for any A_{mn} , Eq.(4.5) holds only for $\xi - \xi_0 = K_m/m$, where K_m is an integer in domain $(-m, m)$. From Eq.(4.6), $\eta - \eta_0 = K_n/n$ can also be concluded, where K_n is an integer in domain $(-n, n)$. By adding Eq.(4.1) to Eq.(4.3), and Eq.(4.2) to Eq.(4.4), another set of relations can be obtained as $\xi + \xi_0 = K'_m/m$ and $\eta + \eta_0 = K'_n/n$, where K'_m and K'_n are integers in domains $(0, 2m)$ and $(0, 2n)$, respectively. The two sets of relations result in four combinations of possible values of (ξ, η) , which are $(K_m/m + \xi_0, K_n/n + \eta_0)$, $(K_m/m + \xi_0, K'_n/n - \eta_0)$, $(K'_m/m - \xi_0, K_n/n + \eta_0)$ and $(K'_m/m - \xi_0, K'_n/n - \eta_0)$. Substituting these relations into $|w|$, the maximum plate deflection can be expressed as

$$|w_M| = \left| \sum_{n=1}^{\infty} \sum_{m=1}^{\infty} A_{mn} (-1)^{K_m + K_n} \sin^2(m\pi\xi_0) \sin^2(n\pi\eta_0) \right| \quad (4.7)$$

$$|w_M| = \left| \sum_{n=1}^{\infty} \sum_{m=1}^{\infty} A_{mn} (-1)^{K_m + K'_n - 1} \sin^2(m\pi\xi_0) \sin^2(n\pi\eta_0) \right| \quad (4.8)$$

$$|w_M| = \left| \sum_{n=1}^{\infty} \sum_{m=1}^{\infty} A_{mn} (-1)^{K'_m + K_n - 1} \sin^2(m\pi\xi_0) \sin^2(n\pi\eta_0) \right| \quad (4.9)$$

$$|w_M| = \left| \sum_{n=1}^{\infty} \sum_{m=1}^{\infty} A_{mn} (-1)^{K'_m + K'_n - 2} \sin^2(m\pi\xi_0) \sin^2(n\pi\eta_0) \right| \quad (4.10)$$

The maximum of Eqs.(4.7)-(4.10) is the equation that the optimal locations of PZT actuator should satisfy. Since Eqs.(4.7)-(4.10) also satisfy the inequality of

$$|w_M| \leq \sum_{n=1}^{\infty} \sum_{m=1}^{\infty} |A_{mn}| \sin^2(m\pi\xi_0) \sin^2(n\pi\eta_0) \quad (4.11)$$

Chapter 4 Optimal placement of piezoelectric actuators on plate and shell

where the equal sign holds only when all coefficients of $\sin^2(m\pi\xi_0)\sin^2(n\pi\eta_0)$ in Eqs.(4.7)-(4.10) have the same sign. Thus, the optimal locations of PZT actuator is governed by

$$|w_M| = \sum_{n=1}^{\infty} \sum_{m=1}^{\infty} |A_{mn}| \sin^2(m\pi\xi_0) \sin^2(n\pi\eta_0) \quad (4.12)$$

The PZT actuator location (ξ_0, η_0) which maximizes Eq.(4.12) is the optimal locations of the PZT actuator. Since the term $\chi_{mn} = \sin^2(m\pi\xi_0)\sin^2(n\pi\eta_0)$ in Eq.(4.12) is a function of locations of the PZT actuator, it is named as “position mode function” (PMF) in this work.

For a rectangular plate, a natural frequency ω_{mn} generally corresponds to a unique vibration mode (m, n) . Thus, when the PZT driving frequency ω approaches ω_{mn} , only one PMF $\chi_{mn} = \sin^2(m\pi\xi_0)\sin^2(n\pi\eta_0)$ is amplified. Neglecting all the other terms that are not amplified in Eq.(4.12), the optimal locations of PZT actuator can be found by

$$\frac{\partial \chi_{mn}}{\partial \xi_0} = 0 \quad \text{and} \quad \frac{\partial \chi_{mn}}{\partial \eta_0} = 0 \quad (4.13)$$

in the conditions of $\begin{vmatrix} \frac{\partial^2 \chi_{mn}}{\partial \xi_0 \partial \eta_0} & \frac{\partial^2 \chi_{mn}}{\partial \xi_0^2} \\ \frac{\partial^2 \chi_{mn}}{\partial \eta_0^2} & \frac{\partial^2 \chi_{mn}}{\partial \xi_0 \partial \eta_0} \end{vmatrix} < 0, \frac{\partial^2 \chi_{mn}}{\partial \xi_0^2} < 0 \text{ and } \frac{\partial^2 \chi_{mn}}{\partial \eta_0^2} < 0$. The solutions

are $\xi_0 = \frac{4N \pm 1}{2m}$ and $\eta_0 = \frac{4N \pm 1}{2n}$, where $N = 0, 1, 2, \dots$ and $0 < \xi_0, \eta_0 < 1$. These

solutions coincide with the optimal locations shown in Fig.4.1. For example, if the driving frequency is close to the natural frequency of vibration mode (1,2), the optimal location of the PZT actuator are (1/2, 1/4) and (1/2, 3/4), which are consistent with the results in Fig.4.1.

Chapter 4 Optimal placement of piezoelectric actuators on plate and shell

The optimal locations are actually identical with the anti-nodes of respective vibration modes. This observation agrees with the finite element results of optimal positions of a piezoelectric patch on a simply supported rectangular plate of Ip and Tse (2001). Their optimal locations were obtained from the controllability perspective, in which the objective function of controllability was equivalent to maximizing the maximum transverse vibration of plate, which is also the focus of this chapter. The difference lies in the methods used. Ip and Tse used finite element method to study this problem while in this chapter an analytical method is employed.

For certain rectangular plates, two or more different vibration modes, $(m_1, n_1), (m_2, n_2), \dots, (m_N, n_N)$, may have the same or very close natural frequency. When the driving frequency approaches this natural frequency, all these vibration modes will be amplified. For this case, the optimal locations of PZT can be found through a combination of PMFs of these vibration modes, i.e., $\Psi = |A_{m_1 n_1}| \chi_{m_1 n_1} + |A_{m_2 n_2}| \chi_{m_2 n_2} + \dots + |A_{m_N n_N}| \chi_{m_N n_N}$, which can be named as the combined position mode function (CPMF). The optimal locations of the PZT actuator can be obtained by

$$\frac{\partial \Psi}{\partial \xi_0} = 0 \text{ and } \frac{\partial \Psi}{\partial \eta_0} = 0 \quad (4.14)$$

in the conditions of $\left| \begin{array}{cc} \frac{\partial^2 \Psi}{\partial \xi_0 \partial \eta_0} & \frac{\partial^2 \Psi}{\partial \xi_0^2} \\ \frac{\partial^2 \Psi}{\partial \eta_0^2} & \frac{\partial^2 \Psi}{\partial \xi_0 \partial \eta_0} \end{array} \right| < 0$, $\frac{\partial^2 \Psi}{\partial \xi_0^2} < 0$ and $\frac{\partial^2 \Psi}{\partial \eta_0^2} < 0$. Generally, the

analytical solution to Eq.(4.14) is not attainable. However, the CPMF can be plotted in the $\xi_0 \eta_0$ -plane, through which the PZT optimal locations can be identified.

Fig.4.3 illustrates an example for such a case. The natural frequency of vibration mode (2,2) is equal to that of vibration mode (4,1), which is 45294.85 rad/s. It is observed that the optimal location patterns are neither similar to vibration mode (2,2) nor vibration mode (4,1). Nevertheless, the plot of CPMF, $\Psi = \chi_{22} + \chi_{41}$, as

Chapter 4 Optimal placement of piezoelectric actuators on plate and shell

shown in Fig.4.4, agrees well with the pattern obtained by the computer program when $A_{22} = A_{41}$, as shown in Fig.4.3.

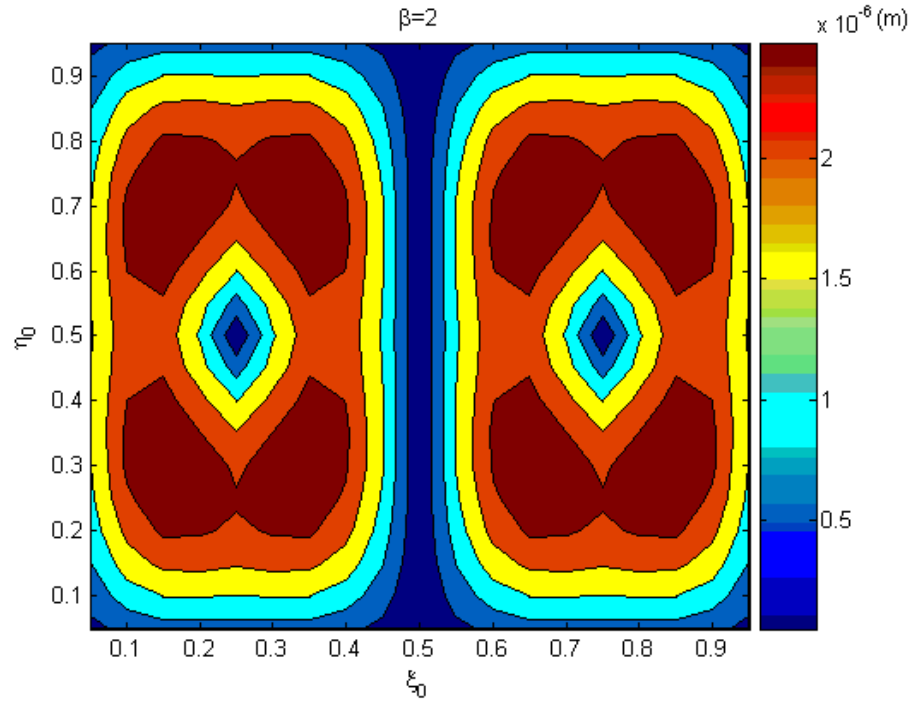


Figure 4.3 Optimal locations of a PZT actuator on rectangular plate with driving frequency closes to natural frequency of vibration modes (2,2) and (4,1)

Chapter 4 Optimal placement of piezoelectric actuators on plate and shell

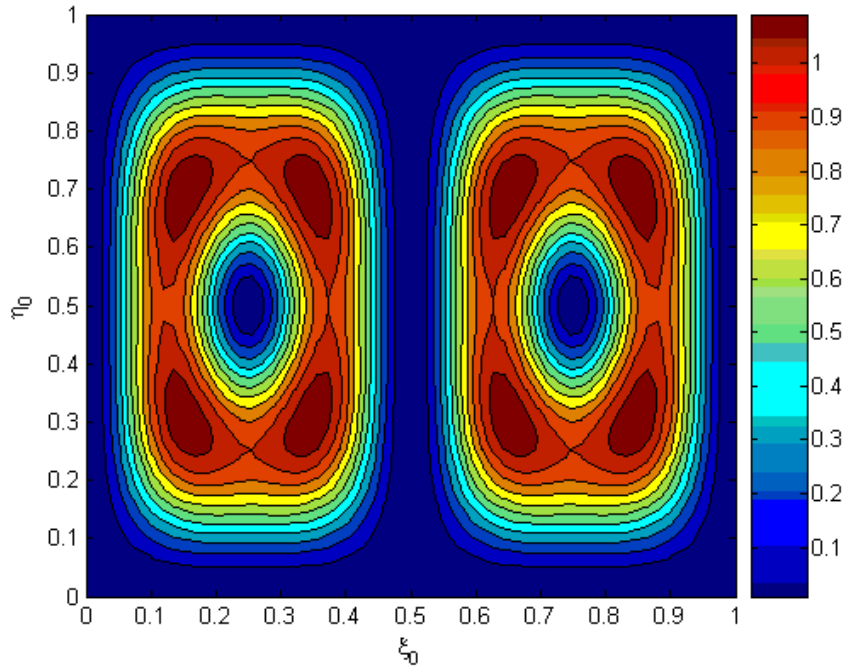


Figure 4.4 Plot of CPMF $\Psi = \chi_{22} + \chi_{41}$

As a special case of the rectangular plate, any two symmetric vibration modes of a square plate share the same natural frequency. Therefore, the CPMF for a square plate can be expressed as $\Psi = |A_{mn}| \chi_{mn} + |A_{nm}| \chi_{nm}$. Since $r_\xi = r_\eta$ and $\omega_m = \omega_n$ for the square plate, $A_{mn} = A_{nm}$. Thus, the CPMF can be simplified as $\Psi = \chi_{mn} + \chi_{nm}$. Fig.4.6 shows the contour plots of the CPMFs for $m, n \in \{1, 2, 3\}$. Compared with the results from the computer program as shown in Fig.4.5, it is evident that the patterns indicated in Fig.4.6 are almost the same as those in Fig.4.5 and the optimal locations in Fig.4.6 are exactly the same as those determined from Fig.4.5. This means that the CPMFs can be used to determine the optimal placement of the PZT actuator.

For the square plate, the modal shapes are identical as those shown in Fig.4.2. It is worth noting that for a vibration mode (m, n) , the optimal location pattern in Fig.4.5 or Fig.4.6 is different from the modal shape in Fig.4.2 for $m \neq n$, and they are the same for $m=n$, unlike the rectangle plate where the optimal location patterns are always identical with their corresponding modal shapes (Figs.4.1 and 4.2). This

Chapter 4 Optimal placement of piezoelectric actuators on plate and shell

observation can be explained as follows. For the rectangular plate, the optimal location pattern can be determined from a single PMF $\chi_{mn} = \sin^2(m\pi\xi_0)\sin^2(n\pi\eta_0)$ which has the same plot as the mode shape (m,n) . However, for the square plate, the optimal location pattern is determined by the CPMF $\Psi = \chi_{mn} + \chi_{nm} = \sin^2(m\pi\xi_0)\sin^2(n\pi\eta_0) + \sin^2(n\pi\xi_0)\sin^2(m\pi\eta_0)$ which has different plot from the mode shape (m,n) when $m \neq n$, and has the same as the mode shape when $m = n$.

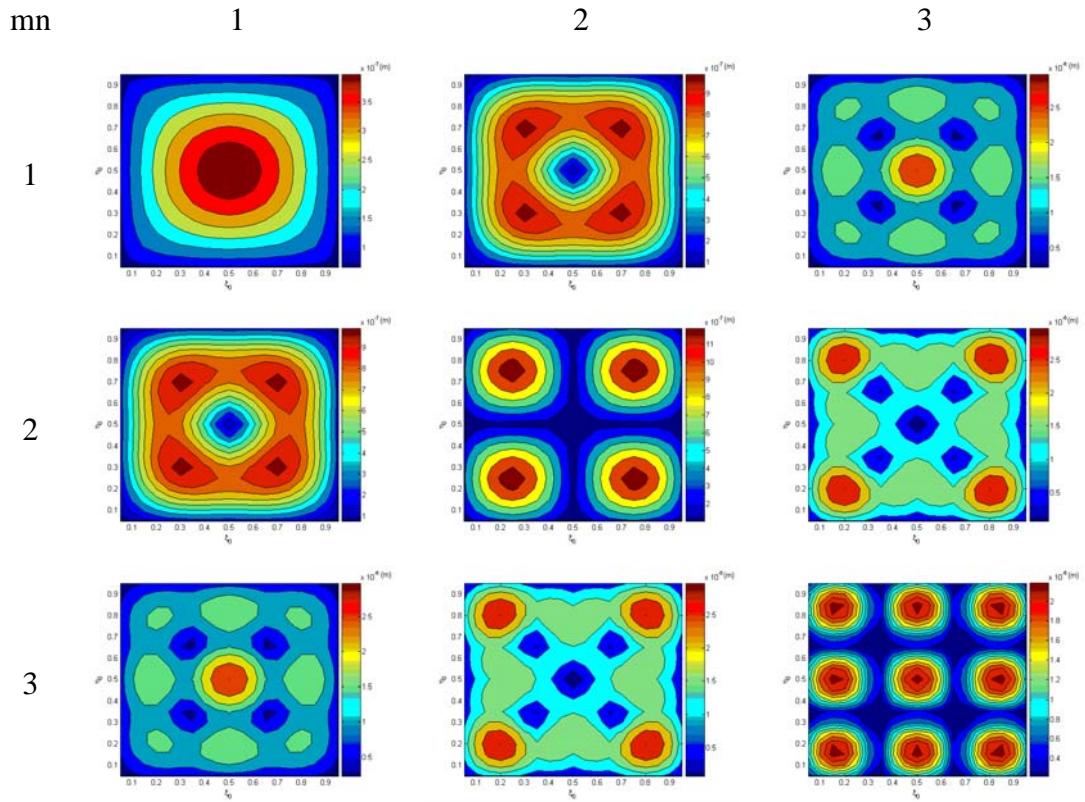


Figure 4.5 Optimal location patterns of a PZT actuator on a square plate at driving frequencies close to natural frequencies

Chapter 4 Optimal placement of piezoelectric actuators on plate and shell

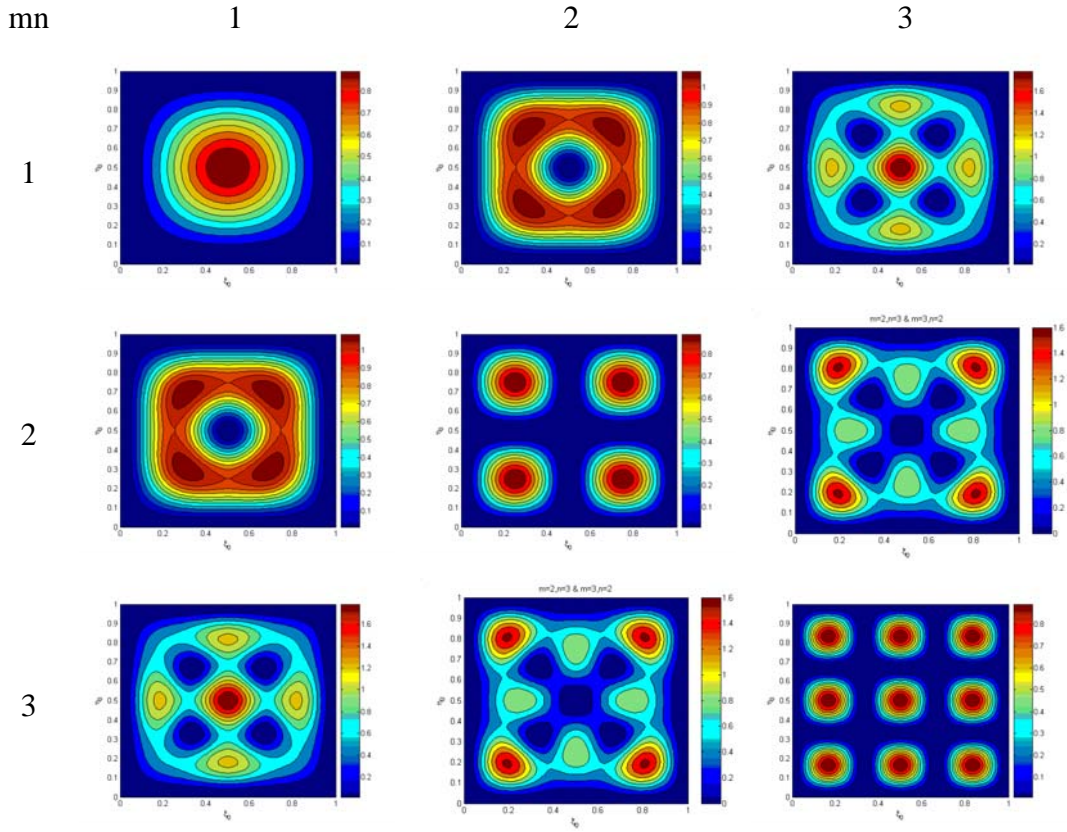


Figure 4.6 Plots of CPMFs for square plate

4.2.2 Driving frequencies not close to natural frequencies

In most situations, the driving frequencies may not be close to any natural frequency. In order to study the optimal locations of the PZT actuator on the rectangular plate, three frequencies within the interval of two adjacent natural frequencies are selected to be the driving frequencies. These three frequencies are $\omega_1 = \omega_{m_1 n_1} + (\omega_{m_2 n_2} - \omega_{m_1 n_1})/4$, $\omega_2 = (\omega_{m_1 n_1} + \omega_{m_2 n_2})/2$ and $\omega_3 = \omega_{m_1 n_1} + 3(\omega_{m_2 n_2} - \omega_{m_1 n_1})/4$, where $\omega_{m_1 n_1}$ and $\omega_{m_2 n_2}$ are the two adjacent natural frequencies and $\omega_{m_1 n_1} < \omega_{m_2 n_2}$.

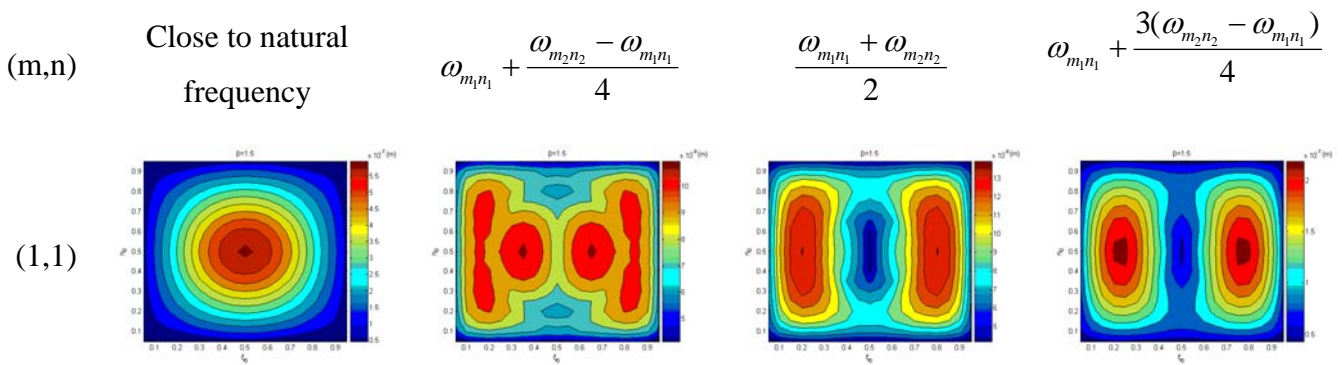
Fig.4.7 shows the results of optimal locations of the PZT actuator for the driving frequencies not close to the natural frequencies. For a specific mode in Fig.4.7, the

Chapter 4 Optimal placement of piezoelectric actuators on plate and shell

first row shows the optimal location patterns calculated from the computer program while the second row presents the predictions obtained from the CPMFs which are defined in the next paragraph. It is observed that the patterns of optimal locations are similar to each other within two adjacent natural frequencies. Transitions can be observed with driving frequencies changing from ω_1 to ω_3 . The optimal patterns of ω_1 are similar to the previous resonance patterns while the optimal patterns of ω_3 are similar to the next resonance patterns.

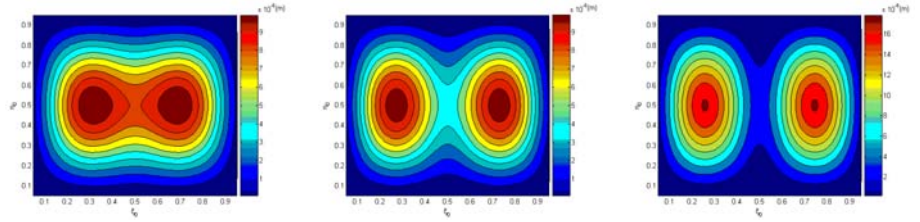
Assume that the driving frequency ω is not close to any natural frequency and $\omega_{m_1 n_1} < \omega < \omega_{m_2 n_2}$, where $\omega_{m_1 n_1}$ and $\omega_{m_2 n_2}$ are the two adjacent natural frequencies. In Eq.(4.12), the two adjacent PMFs $\chi_{m_1 n_1}$ and $\chi_{m_2 n_2}$ have the largest weights and contribute most to the deflection. Thus, the pattern of optimal locations can be approximately determined by the CPMF as $\Psi = |A_{m_1 n_1}| \chi_{m_1 n_1} + |A_{m_2 n_2}| \chi_{m_2 n_2}$.

The second row of each vibration mode in Fig.4.7 illustrates the predictions from the CPMFs. It can be observed that the optimal locations obtained by the CPMFs match well with those obtained by the computer program. Although the patterns are not exactly the same, the major optimal locations are quite similar. The same conclusion can be drawn for the square plate, where the results are shown in Fig.4.8. Both Figs.4.7 and 4.8 indicate that the CPMFs can successfully identify the optimal locations of the PZT actuator driven by non-resonant frequencies.

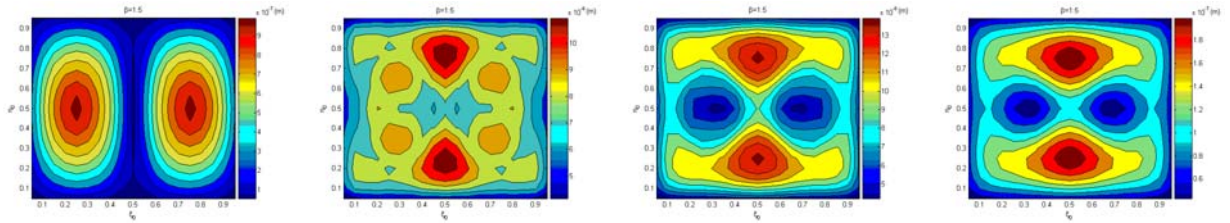


Chapter 4 Optimal placement of piezoelectric actuators on plate and shell

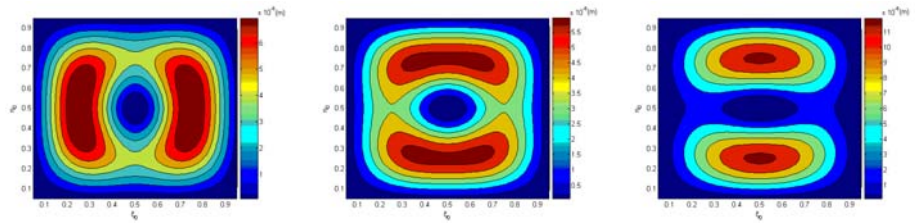
Predictions by
CPMFs



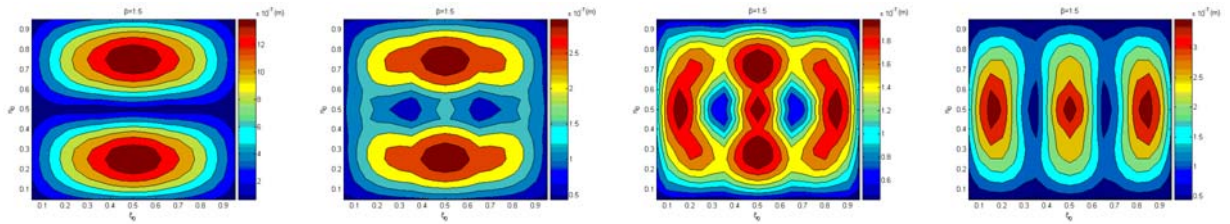
(2,1)



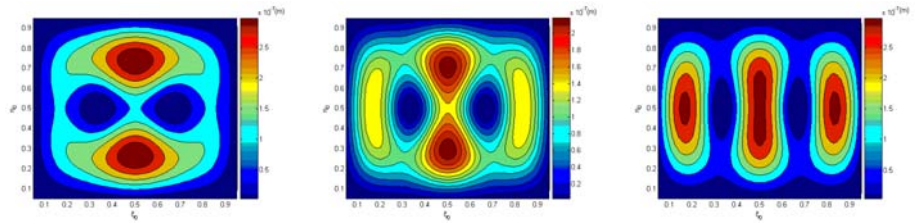
Predictions by
CPMFs



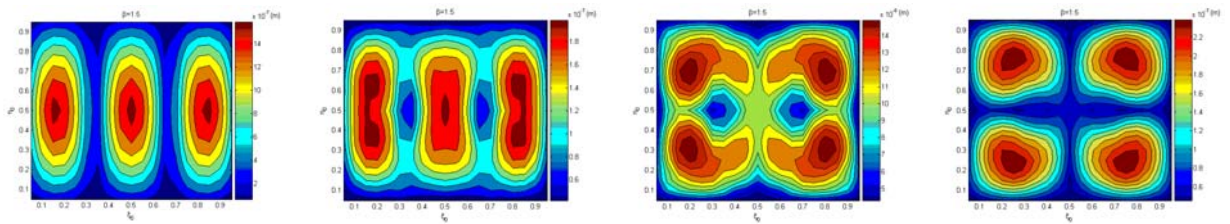
(1,2)



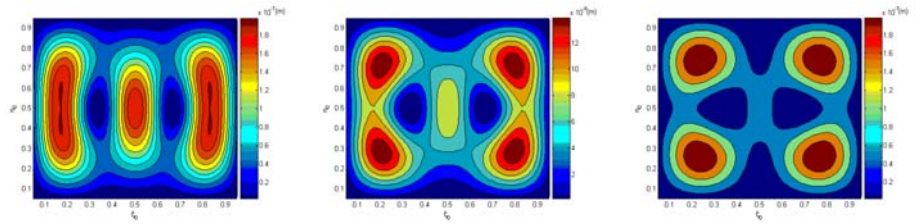
Predictions by
CPMFs



(3,1)

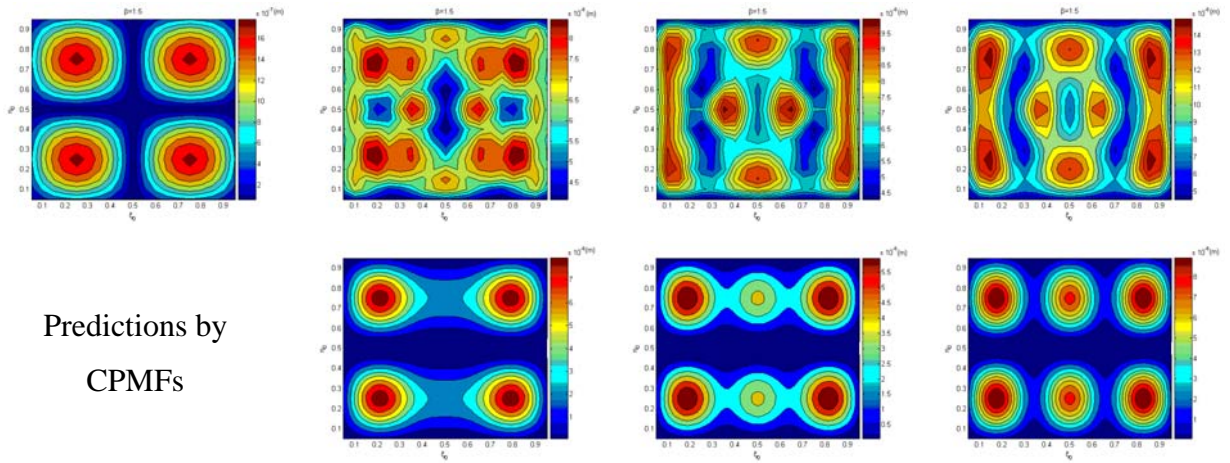


Predictions by
CPMFs

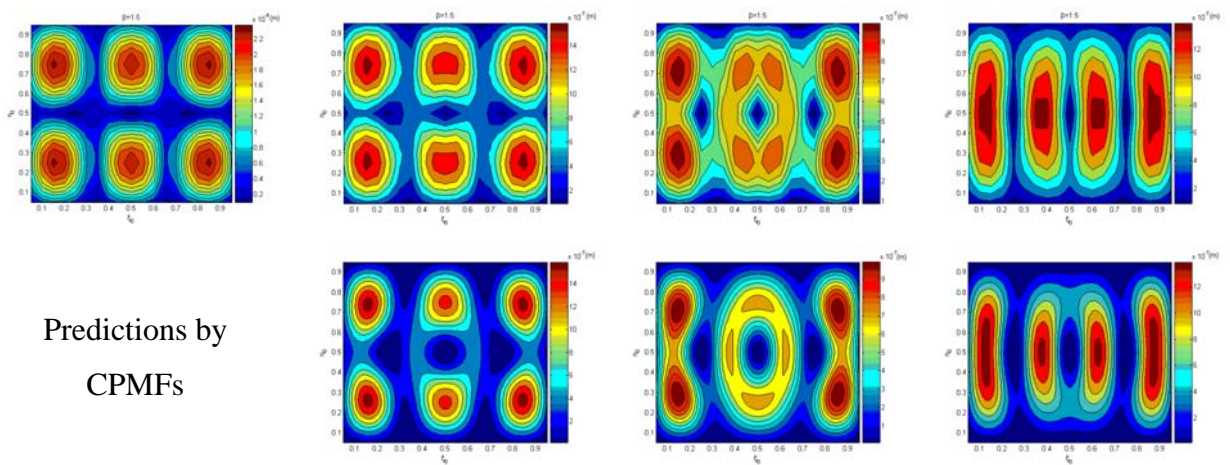


Chapter 4 Optimal placement of piezoelectric actuators on plate and shell

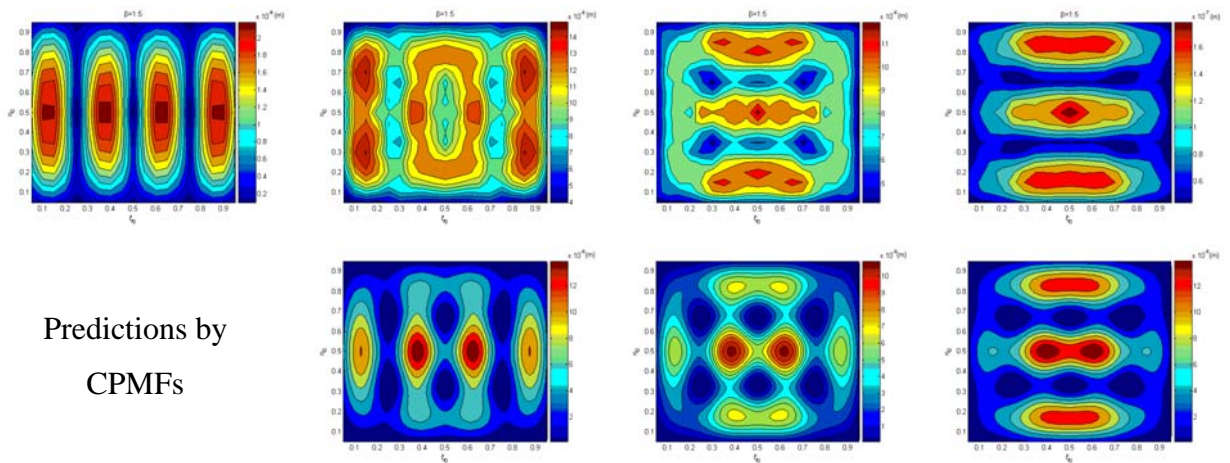
(2,2)



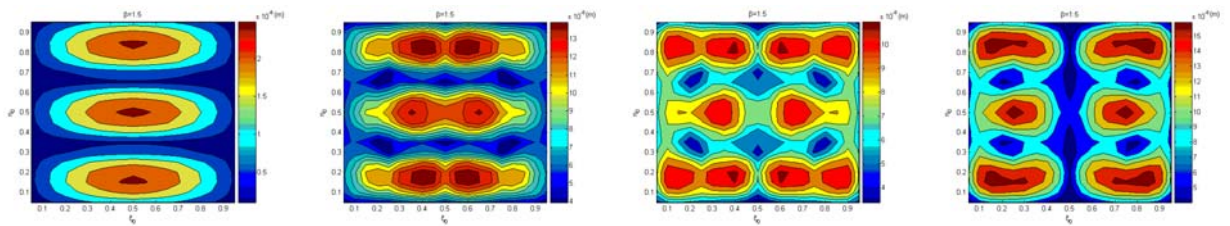
(3,2)



(4,1)

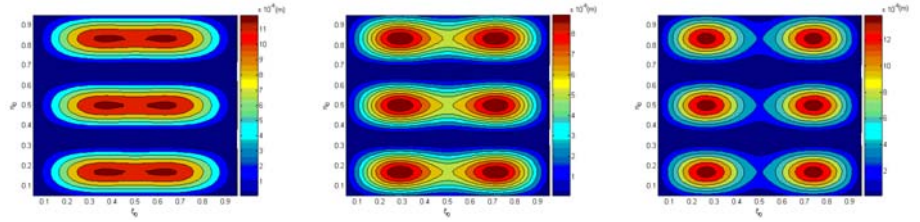


(1,3)

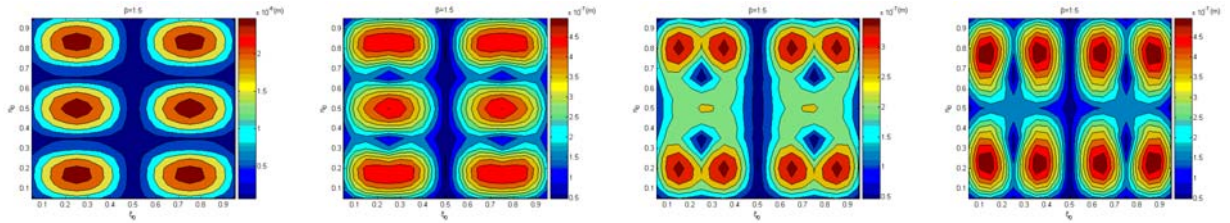


Chapter 4 Optimal placement of piezoelectric actuators on plate and shell

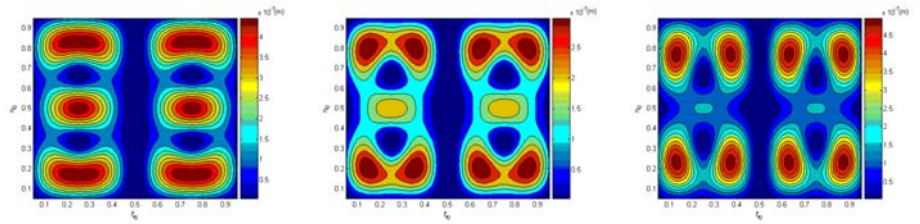
Predictions by
CPMFs



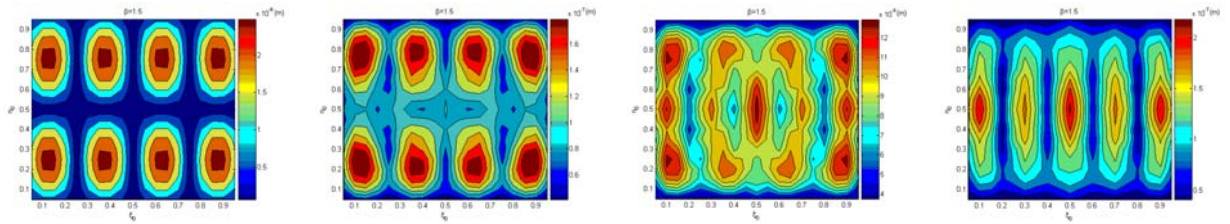
(2,3)



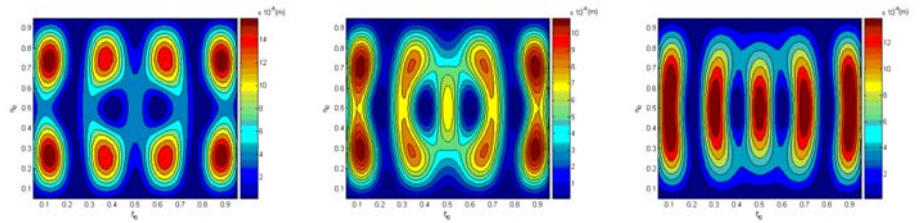
Predictions by
CPMFs



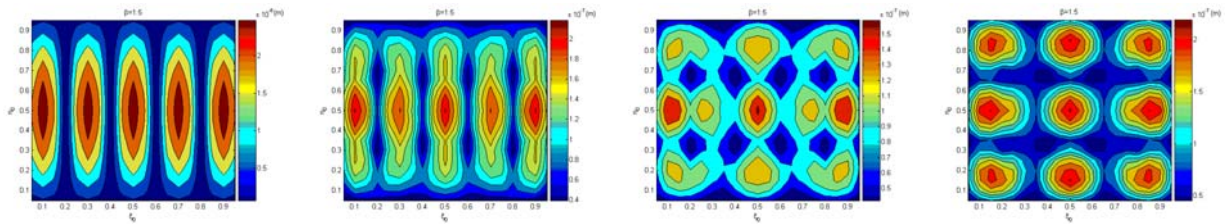
(4,2)



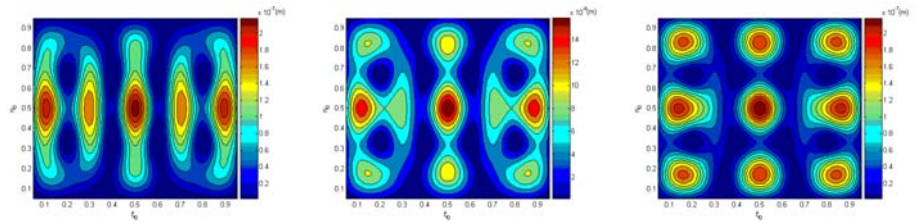
Predictions by
CPMFs



(5,1)



Predictions by
CPMFs



Chapter 4 Optimal placement of piezoelectric actuators on plate and shell

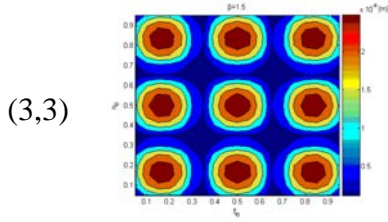
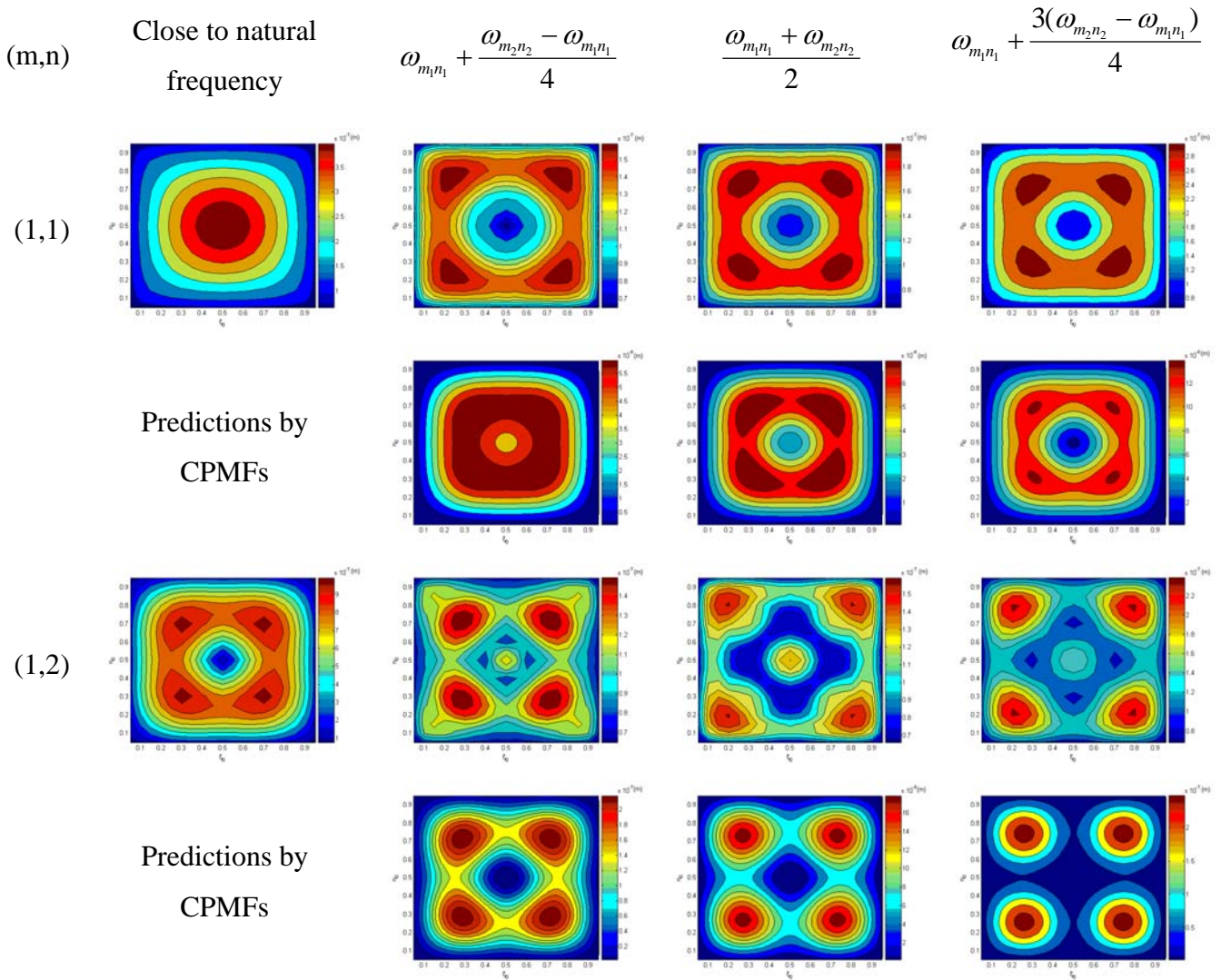
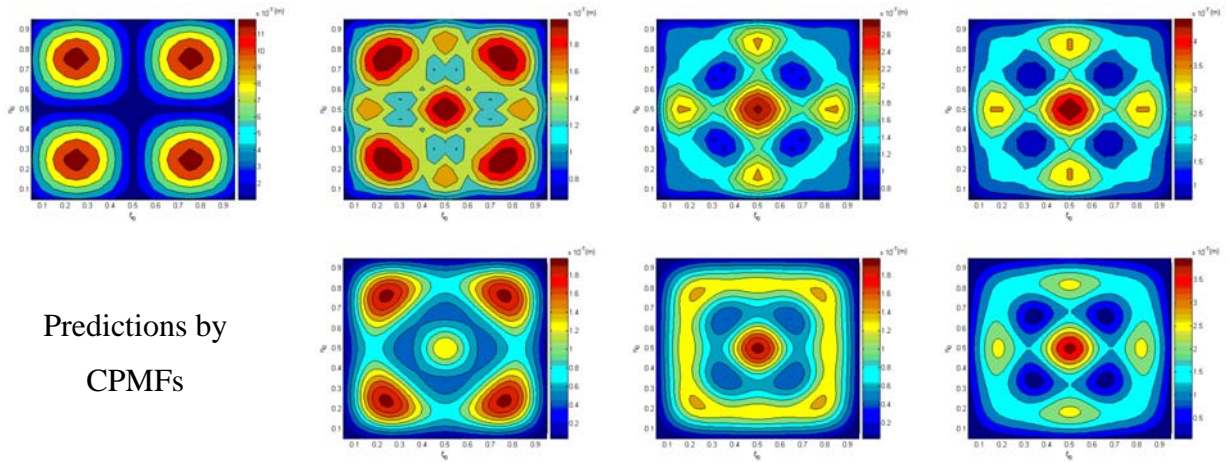


Figure 4.7 Optimal location patterns of a PZT actuator on a rectangular plate with driving frequencies not close to natural frequencies

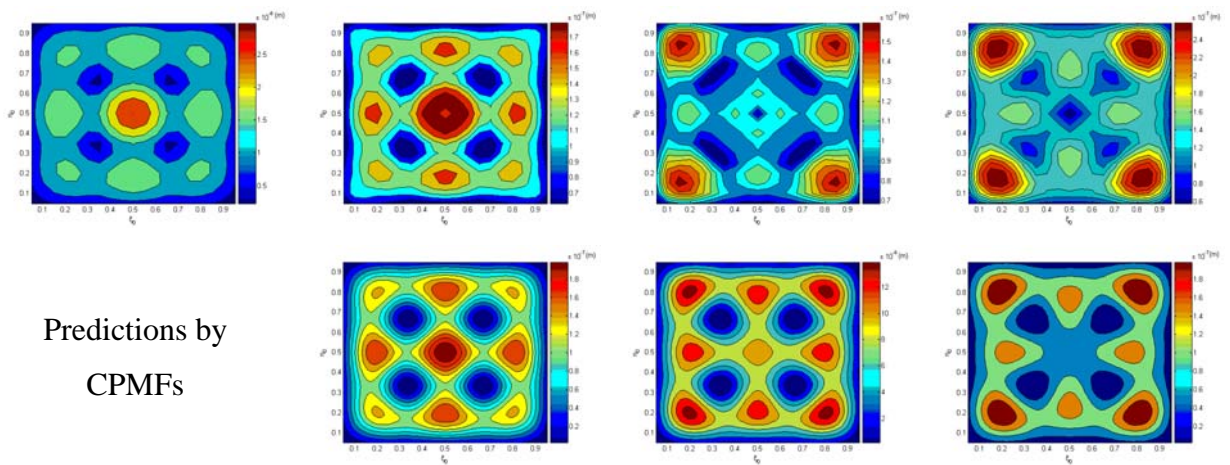


Chapter 4 Optimal placement of piezoelectric actuators on plate and shell

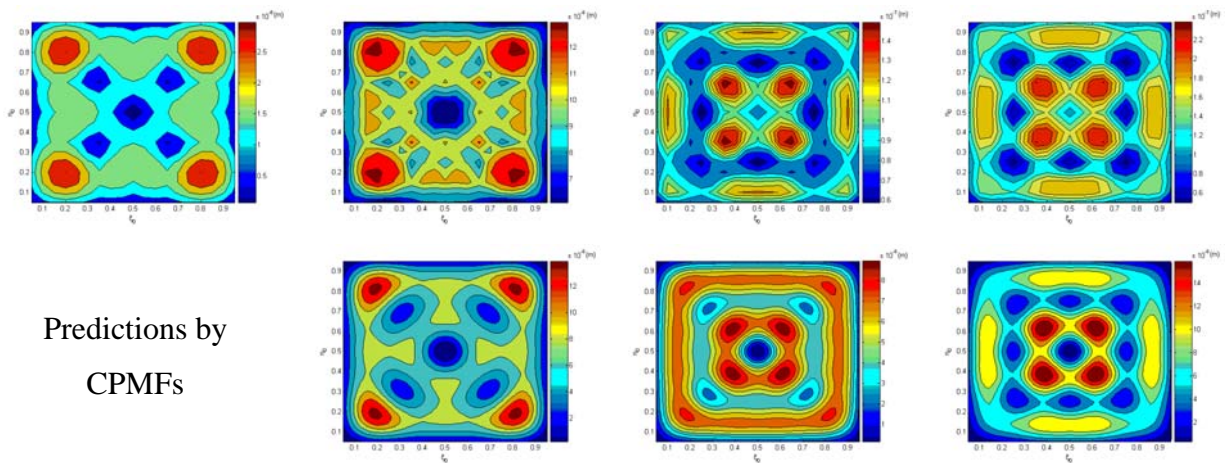
(2,2)



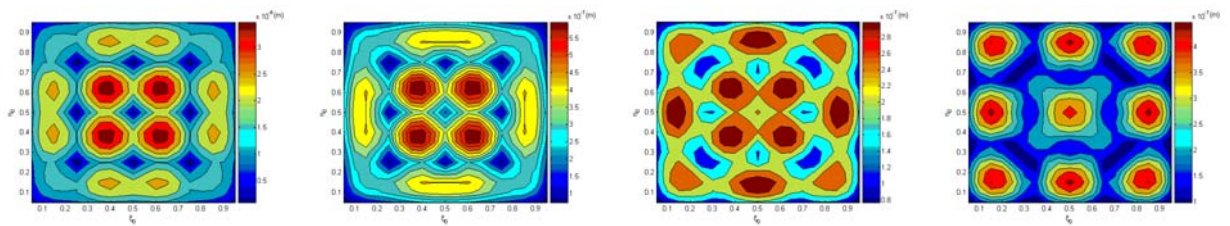
(1,3)



(2,3)



(1,4)



Chapter 4 Optimal placement of piezoelectric actuators on plate and shell

Predictions by
CPMFs

(3,3)

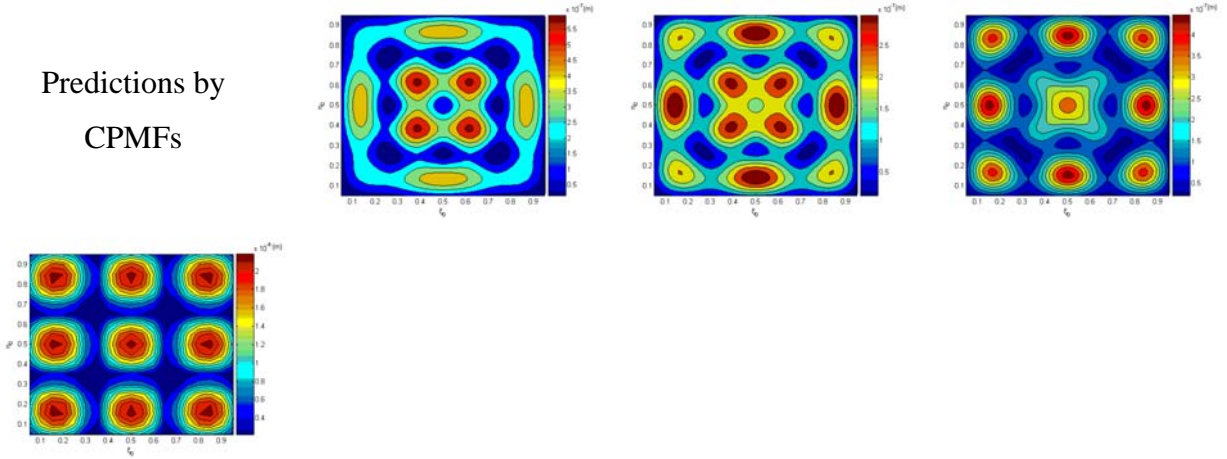


Figure 4.8 Optimal location patterns of a PZT actuator on a square plate with driving frequencies not close to natural frequencies

4.2.3 General procedure to determine PZT optimal locations via CPMF

In summary, the optimal location pattern of the PZT actuator can be represented by the CPMF, i.e., $\Psi = |A_{m_1 n_1}| \chi_{m_1 n_1} + |A_{m_2 n_2}| \chi_{m_2 n_2} + \dots + |A_{m_N n_N}| \chi_{m_N n_N}$. When the driving frequency is close to a natural frequency, the CPMF is the sum of all PMFs at resonance. When the driving frequency is not close to any natural frequency, the CPMF is composed of two PMFs whose corresponding natural frequencies are adjacent to the driving frequency. If more than one vibration modes share the same natural frequency, the corresponding PMFs should be added in the CPMF. Therefore, the general procedure to determine the optimal locations of a PZT actuator on a rectangular/square plate can be summarized as follows.

1. Determine the natural frequencies of plate by using Eq.(3.22) and find whether there are more than one vibration mode that shares the same natural frequency.
2. Construct the CPMF.

If the driving frequency ω is close to a natural frequency $\omega_{m_1 n_1}$, the CPMF consists of the corresponding PMF, i.e., $\Psi = \chi_{m_1 n_1}$. If two or more different

Chapter 4 Optimal placement of piezoelectric actuators on plate and shell

vibration modes, $(m_1, n_1), (m_2, n_2), \dots, (m_N, n_N)$ share the same natural frequency, the CPMF is expressed as

$$\Psi = |A_{m_1 n_1}| \chi_{m_1 n_1} + |A_{m_2 n_2}| \chi_{m_2 n_2} + \dots + |A_{m_N n_N}| \chi_{m_N n_N}.$$

If the driving frequency ω is not close to any natural frequency, i.e., $|\omega - \omega_{ij}| > \Delta$, where i, j are arbitrary natural numbers and Δ is an empirical quantity, say 31.4 (10Hz) for the examples in this chapter, and $\omega_{m_1 n_1} < \omega < \omega_{m_2 n_2}$, where $\omega_{m_1 n_1}$ and $\omega_{m_2 n_2}$ are the two adjacent natural frequencies. The CPMF is $\Psi = |A_{m_1 n_1}| \chi_{m_1 n_1} + |A_{m_2 n_2}| \chi_{m_2 n_2}$. If there are other modes share the same natural frequency as $\omega_{m_1 n_1}$ or $\omega_{m_2 n_2}$, the corresponding PMFs should be added in the CPMF.

3. Plot the CPMF in the $\xi_0 \eta_0$ -plane and the locations with the maximum values on the CPMF plot are the optimal locations of the PZT actuator on the plate.

The computer program developed earlier in this chapter uses Eq.(3.37) to calculate the plate deflections for all the possible PZT locations, where the natural frequencies must be obtained beforehand. Using the proposed general procedure, which only requires the calculation of natural frequencies of the plate and the CPMF, the computational cost can be significantly reduced.

4.3 Optimal placement of PZT actuator on shell

After determining the optimal locations of PZT actuator on plate, the procedure developed in Section 4.2 can be readily used for optimal placement of PZT actuator on shell.

The radial vibration solution of a simply-supported cylindrical shell actuated by a pair of collocated PZT actuators has been obtained in Chapter 3 as described in Eq.(3.61) as

$$w = \sum_{m=1}^{\infty} \sum_{n=1}^{\infty} \frac{4B_{mn} \sin(n\pi\theta_0) \sin(m\pi\xi_0)}{\omega_{mn}^2 - \omega^2} \sin(m\pi\xi) \sin(n\pi\theta) e^{i\omega t} \quad (4.15)$$

Chapter 4 Optimal placement of piezoelectric actuators on plate and shell

This solution is similar to the solution of plate vibration in form. Thus, the following relation can be used,

$$|w|_{\max} = \sum_{m=1}^{\infty} \sum_{n=1}^{\infty} |A_{mn}| \sin^2(n\pi\theta_0) \sin^2(m\pi\xi_0) e^{i\omega t} \quad (4.16)$$

where $\omega_{mn}^2 = \frac{2D}{\rho h} \left[\left(\frac{m^2\pi^2}{L^2} + \frac{n^2\pi^2}{R^2\Phi^2} \right)^2 + \frac{2vm^2\pi^2}{R^2L^2} + \frac{6}{R^2h^2} \right]$ is the natural frequency of the shell; $A_{mn} = \frac{16M^a}{\omega_{mn}^2 - \omega^2\rho h} \left(\frac{m}{nL^2} + \frac{n}{mR^2\Phi^2} \right) \sin(m\pi\frac{l_\xi}{2}) \sin(n\pi\frac{\theta_p}{2})$; $\xi_0 = (\xi_1 + \xi_2)/2$; $\theta_0 = (\theta_1 + \theta_2)/2$; $l_\xi = \xi_2 - \xi_1$; and $\theta_p = \theta_2 - \theta_1$.

The CPMF for the shell vibration is

$$\Psi = |A_{m_1n_1}| \chi_{m_1n_1} + |A_{m_2n_2}| \chi_{m_2n_2} \quad (4.17)$$

By plotting Eq.(4.17), the optimal locations of the PZT pair can be determined.

An example is calculated for illustration. The parameters are listed in Table 3.2.

Figs.4.9 and 4.10 show the optimal locations of the PZT pair on the cylindrical shell determined by the computer program and the CPMF, respectively. It is evident that all the six optimal locations determined by the computer program are also identified by the CPMF with reasonable accuracy. These results indicate that the CPMF is valid to be used to determine the optimal placement of PZT actuators on shell structures.

Chapter 4 Optimal placement of piezoelectric actuators on plate and shell

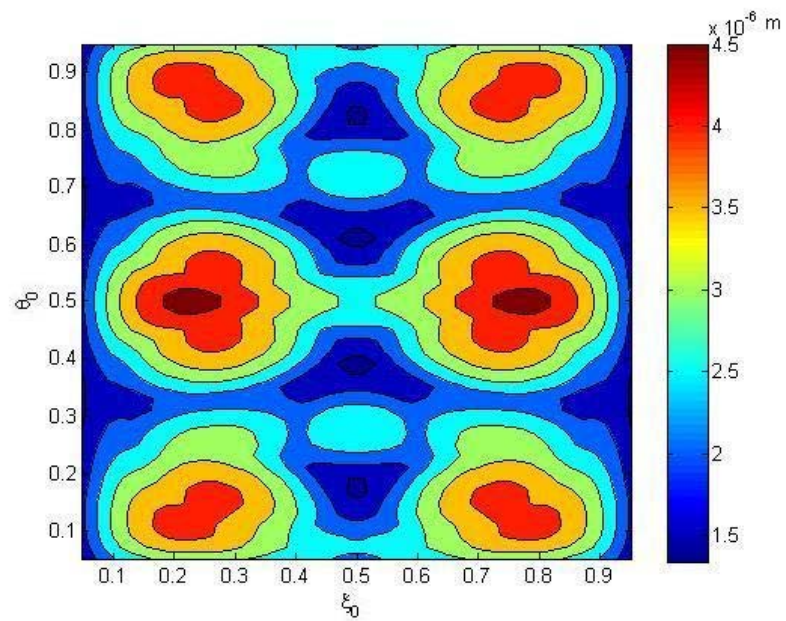


Figure 4.9 Numerical results of optimal location pattern of a pair of collocated PZTs when $\omega = 5155$ rad/s

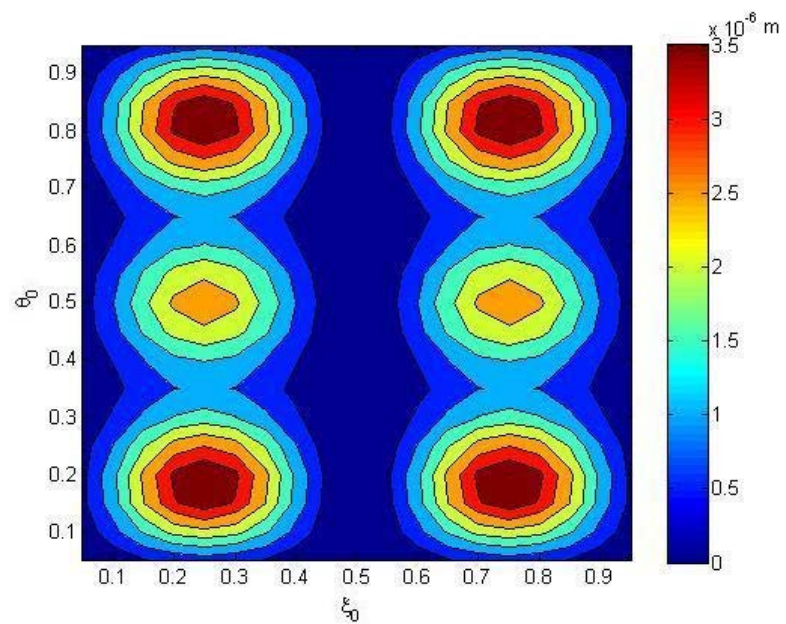


Figure 4.10 Optimal location pattern of a pair of collocated PZTs when $\omega = 5155$ rad/s determined by Eq.(4.17)

Chapter 4 Optimal placement of piezoelectric actuators on plate and shell

4.4 Discussions

4.4.1 Driving frequency lower than the first natural frequency

When the driving frequency is lower than the natural frequency of the first vibration mode, the optimal location pattern at very low driving frequency, i.e., near static condition, should be considered. Figure 4.11 shows the optimal locations of PZT when the driving frequency is 0.01 Hz. It is seen that the optimal locations of the PZT are located near the boundaries. Fig.4.12 shows the optimal location pattern of a PZT actuator when the driving frequency is 4000 Hz. It is observed that the two figures are similar. However, it is also observed that in most regions of the plate, the maximum plate deflection is not very sensitive to the location of the PZT actuator. The changes of maximum plate deflection with different PZT actuator locations are limited in a very small range.

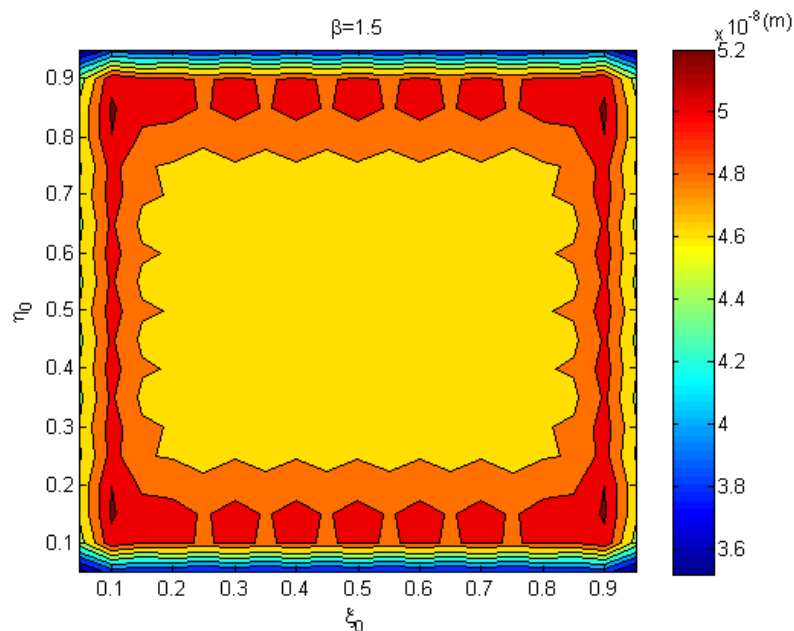


Figure 4.11 Optimal locations when driving frequency is near zero ($\omega=0.0628$ rad/s)

Chapter 4 Optimal placement of piezoelectric actuators on plate and shell

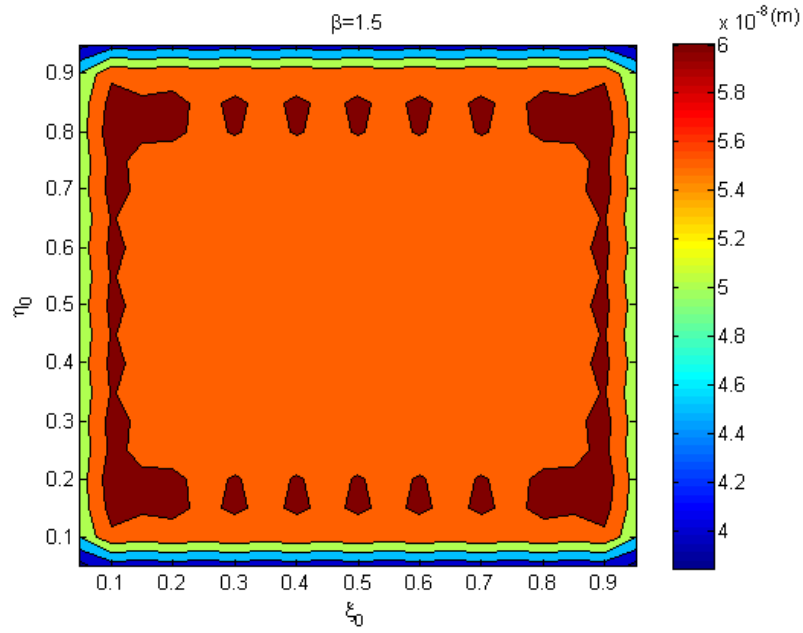


Figure 4.12 Optimal locations when driving frequency lower than the first natural frequency ($\omega=25133$ rad/s)

4.4.2 Effect of PZT size

According to the solution Eq.(3.37) in Chapter 3, when the dimensions of PZT actuator are set as certain values, some vibration modes will vanish. That is, certain vibration modes can be suppressed by varying the size of the PZT actuator. For example, when $r_\xi = \frac{N}{m}$ and/or $r_\eta = \frac{N}{n}$, the deflection of mode $(m,*)$ or $(n,*)$ becomes zero, where $N = 1, 2, 3, \dots$ and “*” stands for any positive integer. Similar observation was reported by Dimitriadis et al. (1991), who drew the conclusion from some numerical examples. This finding may be useful for vibration control with PZT actuators.

Chapter 4 Optimal placement of piezoelectric actuators on plate and shell

4.4.3 Effects of material properties, foundation stiffness and in-plane forces

From the discussion above, it is observed that the key factors determining the optimal locations of a PZT actuator on a rectangular plate are the driving frequency of PZT and the natural frequencies of plate. Since the natural frequencies of plate are determined by the material properties, foundation stiffness as well as the in-plane forces, as indicated in Eq.(3.22), variations in these parameters will cause changes in the natural frequencies. However, these variations will not affect the optimal location pattern of the PZT actuator. Since the proposed general procedure to determine the optimal locations of the PZT actuator is based on the relations between the driving frequency and the natural frequencies, changes in material properties, foundation stiffness and in-plane forces will not affect its applicability.

4.5 Conclusions

In this chapter, optimal placement of PZT actuator in terms of maximizing the plate and shell vibration was discussed. It was found that the optimal locations of the PZT actuator were dependent on the driving frequency of the actuator and the natural frequencies of the plate. The optimal locations of the actuator could be identified by the CPMF no matter whether the driving frequency was close to the natural frequencies or not. It was also found that the geometry of PZT actuator had the capacity of suppressing certain vibration modes. These findings provide guidelines for exciting plates and shells on elastic foundations by PZT actuators. It is worth mentioning that the solution procedure presented in this chapter is not only applicable to the simply supported plates and cylindrical shells but also to the plates and shells with other boundary conditions, such as the clamped plates and the cantilevered plates provided that the mode shape functions in the derivation are changed accordingly.

Chapter 5 Modeling of Ionic Polymer-Metal Composites

5.1 Introduction

Ionic polymer-metal composite (IPMC) is a type of wet electro-active polymer (EAP). It consists of a thin polyelectrolyte membrane and a type of noble metal, such as gold and platinum, chemically plated on both sides of the membrane. Fig.5.1 shows the cross section of a platinum-plated Nafion-based IPMC sample. The IPMC can undergo a large bending motion when a low electric potential is applied to its electrodes. Conversely, the IPMC can generate a measurable electric potential when it is subject to an imposed deformation. Thus, the IPMC can serve as both actuators and sensors. The IPMC offers many advantages over the conventional electronic EAMs, such as compliance, light weight, low operation voltage and capability of working in aqueous environments. These properties make the IPMC potentially for numerous applications in various areas.

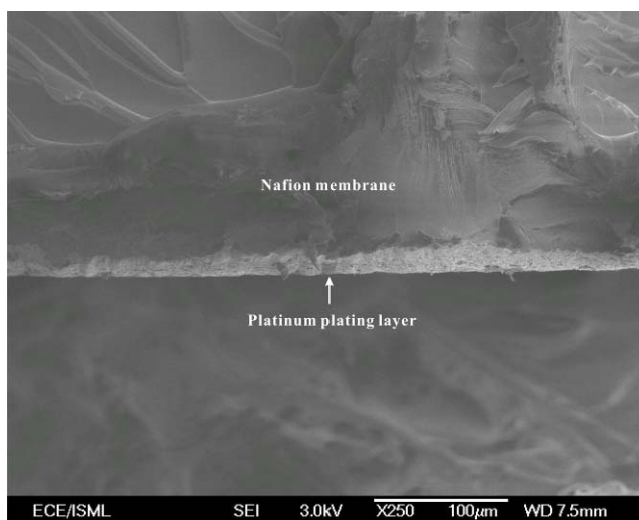


Figure 5.1 Cross section of a Pt-plated Nafion based IPMC

Chapter 5 Modeling of Ionic Polymer-Metal Composites

One of the common questions when a smart material is considered for certain application is how much effect it can provide. For the IPMC materials, the bending capacity of the IPMCs is usually a first concern when they are used as actuators. Thus, the actuation mechanism of the IPMC material should be studied. As stated in Chapter 2, although much effort has been devoted to understanding the actuation and sensing mechanism of IPMC materials, the actuation mechanism of IPMC has not yet been fully understood. Nevertheless, the existing models have already cast important insights into the mechanism research. Of all the first principle models developed, Nemat-Nasser (2002)'s hybrid model has been proved to be useful for IPMCs with different cation and solvent types (Nemat-Nasser, 2002, 2006b). The model parameters can be determined through experiments. This hybrid model has set up the framework of mechanism research toward a complete understanding of IPMCs' working mechanism. However, Nemat-Nassar's hybrid model does not provide an explicit bending moment expression. A computer program is generally required to perform the calculations. The inconvenience of computation actually hinders the applications of this model in practical use.

In view of this, in this chapter, Nemat-Nasser's hybrid actuation model is studied and simplified. Explicit bending moment expressions are derived based on this model by certain simplifications. The obtained bending moment expressions are applicable for both static and dynamic electric potentials.

5.2 Bending moment capacity of IPMC

5.2.1 Charge redistribution

Although the mechanism of IPMC has not yet been fully understood, it is known that the cation motion under the applied electric field is a key issue. Therefore, cation movement should be considered first before analyzing the stress development in the IPMC membrane.

Chapter 5 Modeling of Ionic Polymer-Metal Composites

The microstructure of the polyelectrolyte membrane of an IPMC sample is in the form of interconnected nano-scale clusters as shown in Fig.2.4. The nano-scale clusters are composed of the backbone perfluorinated copolymer of polytetrafluoroethylene with perfluorinated vinyl ether sulfonate pendants for Nafion based IPMCs and perfluorinated propyl ether carboxylate pendants for Flemion based IPMCs. When an IPMC sample is solvated, cations are free to move within or out of the clusters while anions are covalently fixed to the clusters. Thus, when an electric potential is applied to the electrodes of IPMC, cations will migrate to the cathode while anions remain stationary (Fig.2.7). Two boundary layers will form due to the cation movement, characterized as the anion dominant anode boundary layer (ABL) and the cation dominant cathode boundary layer (CBL) (Nemat-Nasser, 2002). The two boundary layers will effectively balance the electric field applied, resulting in the region between the two layers being shielded. Stresses will develop in the two layers, leading to the deformation of the IPMC material. It is the ABL and CBL that primarily contribute to the bending motion of IPMC. Therefore, it is essential to determine the thickness of the ABL and CBL prior to the calculation of the bending moment. To achieve this, the cation redistribution under an electric field should be considered first.

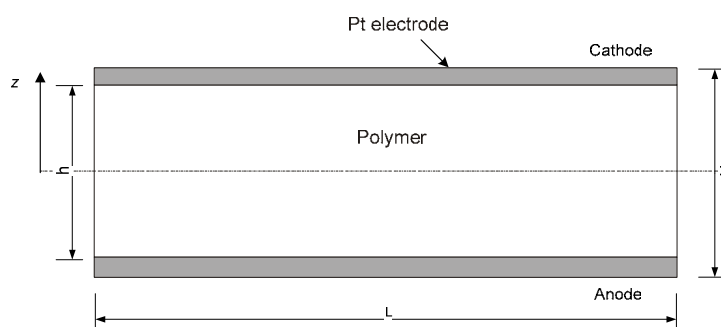


Figure 5.2 Schematic drawing of the cross-section of an IPMC sample

Consider an IPMC sample with thickness H and length L , as shown in Fig.5.2. The thickness of membrane part is h . The IPMC sample is driven by time-dependent electric potentials applied at the electrodes. It is assumed that the top electrode is the cathode and bottom electrode is the anode. The electric potentials applied at the

Chapter 5 Modeling of Ionic Polymer-Metal Composites

cathode and the anode are $\varphi_1(t)$ and $\varphi_2(t)$, respectively. When electric potentials are on, due to the cation movement within the IPMC membrane, the IPMC will vibrate at the driving frequency with certain phase lag.

The cation flux $J_i^+(z, t)$ of ion species i due to diffusion, migration and convection is determined by the Nernst-Planck equation as,

$$J_i^+(z, t) = -D_i^+ \left[\frac{\partial C_i^+(z, t)}{\partial z} + \frac{v_i^+ C_i^+(z, t) F}{RT} \frac{\partial \varphi(z, t)}{\partial z} \right] + C_i^+(z, t) v, \quad (5.1)$$

where the species i refers to a particular type of ion in the membrane, such as Na^+ or K^+ , marked as the i th type ion; D_i^+ is the cation diffusivity coefficient of species i ; v_i^+ is the valence of cations of species i ; $\varphi(z, t)$ is the electric potential; F is the Faraday's constant; R is the gas constant; T is the temperature and v is the solvent velocity. The solvent velocity v can be determined by the Darcy's Law as

$$v = D_h \left[v^- C^- F E(z, t) - \frac{\partial p}{\partial z} \right] \quad (5.2)$$

where D_h is the hydraulic permeability coefficient; v^- and C^- are the valence and density of anions, respectively, where C^- is approximately considered as constant since anions are fixed to the polymer backbone; $E(z, t)$ is the electric field and p is the fluid pressure.

Since only one type of cations is considered, the subscript i in Eq.(5.1) can be dropped. Rewriting Eq.(5.1), we can obtain,

$$J^+(z, t) = -D^+ \left[\frac{\partial C^+(z, t)}{\partial z} - \frac{v^+ C^+(z, t) F}{RT} \frac{\partial \varphi(z, t)}{\partial z} \right] + C^+(z, t) v, \quad (5.3)$$

Considering the mass conservation equation which is,

Chapter 5 Modeling of Ionic Polymer-Metal Composites

$$\frac{\partial C^+(z,t)}{\partial t} = -\frac{\partial J^+(z,t)}{\partial z} \quad (5.4)$$

Substituting Eq.(5.3) into Eq.(5.4), the following equation can be obtained,

$$\frac{\partial C^+(z,t)}{\partial t} = D^+ \frac{\partial^2 C^+(z,t)}{\partial z^2} - D^+ \frac{v^+ F}{RT} \left[\frac{\partial C^+(z,t)}{\partial z} \frac{\partial \phi(z,t)}{\partial z} + C^+(z,t) \frac{\partial^2 \phi(z,t)}{\partial z^2} \right] \quad (5.5)$$

The basic electrostatic equations associated with the problem are,

$$E(z,t) = -\frac{\partial \phi(z,t)}{\partial z} \quad (5.6)$$

$$D = \kappa_e E(z,t) \quad (5.7)$$

$$\frac{\partial D}{\partial z} = \rho_c \quad (5.8)$$

$$\rho_c = (v^+ C^+(z,t) - v^- C^-(z,t)) F \quad (5.9)$$

where κ_e is the electric permittivity; D is the electric displacement; and ρ_c is the net charge density.

The relationship between cation concentration and electric potential can be derived from Eqs.(5.6)-(5.9), which is the Poisson's as

$$\frac{\partial^2 \phi(z,t)}{\partial z^2} = -\frac{F}{\kappa_e} (v^+ C^+(z,t) - v^- C^-(z,t)) \quad (5.10)$$

Eqs.(5.5) and (5.10) are the governing equations of the cation transportation within the IPMC membrane.

Chapter 5 Modeling of Ionic Polymer-Metal Composites

Integrating Eq.(5.10) with respect to z , the electric field due to charge concentration can be obtained as

$$\frac{\partial \varphi(z, t)}{\partial z} = \int^z -\frac{F}{\kappa_e} (v^+ C^+(z, t) - v^- C^-(z, t)) dz + A(t) \quad (5.11)$$

The time-dependent function $A(t)$ in Eq.(5.11) can be viewed as the electric field induced by the electric potential applied on the IPMC membrane. Thus, Eq.(5.11) can be rewritten as,

$$\frac{\partial \varphi(z, t)}{\partial z} = \frac{\varphi_1(t) - \varphi_2(t)}{h} + \int_{-h/2}^z -\frac{F}{\kappa_e} (v^+ C^+(z, t) - v^- C^-(z, t)) dz \quad (5.12)$$

Substituting Eq.(5.12) into Eq.(5.5), we obtain

$$\begin{aligned} \frac{\partial C^+(z, t)}{\partial t} = & D^+ \frac{\partial^2 C^+(z, t)}{\partial z^2} - D^+ \frac{v^+ F}{RT} \frac{\partial C^+(z, t)}{\partial z} [f(t) + g(C^+(z, t))] \\ & - D^+ \frac{(v^+ F)^2}{\kappa_e RT} C^+(z, t) [C^+(z, t) - \frac{v^-}{v^+} C^-(z, t)] \end{aligned} \quad (5.13)$$

where $f(t) = \frac{\varphi_1(t) - \varphi_2(t)}{h}$ and $g(C^+(z, t)) = \int_{-h/2}^z -\frac{F}{\kappa_e} (v^+ C^+(z, t) - v^- C^-(z, t)) dz$.

The boundary and initial conditions for the problem are

$$\int_{-h/2}^{h/2} \rho_c dz = 0 \quad (5.14)$$

$$\varphi(h/2, t) = \varphi_1(t), \quad \varphi(-h/2, t) = \varphi_2(t) \quad (5.15)$$

$$J^+(\pm h/2, t) = 0 \quad (5.16)$$

$$\varphi_1(0) = 0, \quad \varphi_2(0), \quad \rho_c(z, 0) = 0 \quad (5.17)$$

Chapter 5 Modeling of Ionic Polymer-Metal Composites

As the governing equation is in terms of cation concentration, it is convenient to express the boundary conditions in terms of cation concentration rather than the electric potentials and cation flux. Integrating Eq.(5.10) from $z = -h/2$ to $z = h/2$, and noting the overall electroneutrality as prescribed in Eq.(5.14) $\int_{-h/2}^{h/2} \rho_c dz = 0$, the following relation can be obtained,

$$\frac{\partial \varphi(h/2, t)}{\partial z} = \frac{\partial \varphi(-h/2, t)}{\partial z} \quad (5.18)$$

This equation indicates that the electric fields at the two boundaries are the same. From Eq.(5.12) and Eq.(5.18), the electric fields at the boundaries can be determined as,

$$\frac{\partial \varphi(h/2, t)}{\partial z} = \frac{\partial \varphi(-h/2, t)}{\partial z} = \frac{\varphi_1(t) - \varphi_2(t)}{h} \quad (5.19)$$

Substituting Eq.(5.19) into Eq.(5.16), we can obtain,

$$C^+(\pm h/2, t) = \frac{v^- C^-}{v^+} e^{\mp [\varphi_1(t) - \varphi_2(t)] v^+ F / 2RT} \quad (5.20)$$

It is evident that Eq.(5.13) is a nonlinear partial differential equation. Due to the implicit nature of $g(C^+(z, t))$, analytical solution is difficult to derive. As for small ions such as Na^+ and Li^+ , the electric field caused by the ions is usually much smaller than the electric field due to the applied electric potential. Therefore, it is reasonable to drop the term of $g(C^+(z, t))$ in Eq.(5.13) to reduce its nonlinearity and Eq.(5.13) can be simplified as,

Chapter 5 Modeling of Ionic Polymer-Metal Composites

$$\begin{aligned} \frac{\partial C^+(z,t)}{\partial t} = D^+ \frac{\partial^2 C^+(z,t)}{\partial z^2} - D^+ \frac{v^+ F}{RT} f(t) \frac{\partial C^+(z,t)}{\partial z} \\ - D^+ \frac{(v^+ F)^2}{\kappa_e RT} C^+(z,t) \left[C^+(z,t) - \frac{v^-}{v^+} C^- \right] \end{aligned} \quad (5.21)$$

Passing t and z to the new variables t and $z^* = z - \int D^+ \frac{v^+ F}{RT} f(t) dt$, a simpler equation can be obtained as

$$\frac{\partial C^+(z^*,t)}{\partial t} = D^+ \frac{\partial^2 C^+(z^*,t)}{\partial z^{*2}} - D^+ \frac{(v^+ F)^2}{\kappa_e RT} C^+(z^*,t) \left[C^+(z^*,t) - \frac{v^-}{v^+} C^- \right] \quad (5.22)$$

A traveling wave solution is proposed for this problem. Introducing a moving coordinate where $C^+(z^*,t) = C(\varsigma)$ and $\varsigma = \pm k z^* + \lambda t$, Eq.(5.22) can be transformed as

$$\lambda \frac{dC^+(\varsigma)}{d\varsigma} = D^+ k^2 \frac{d^2 C^+(\varsigma)}{d\varsigma^2} - D^+ \frac{(v^+ F)^2}{\kappa_e RT} C^+(\varsigma) \left[C^+(\varsigma) - \frac{v^-}{v^+} C^- \right] \quad (5.23)$$

Rearranging Eq.(5.23), we can obtain a second order autonomous ordinary equation as

$$k^2 [C^+(\varsigma)]'' - \frac{\lambda}{D^+} [C^+(\varsigma)]' - \frac{(v^+ F)^2}{\kappa_e RT} C^+(\varsigma) \left(C^+(\varsigma) - \frac{v^-}{v^+} C^- \right) = 0 \quad (5.24)$$

Assuming $P(C^+(\varsigma)) = \frac{D^+ k^2}{\lambda} [C^+(\varsigma)]'$, Eq.(5.24) can be derived as the Abel equation of the second kind as

Chapter 5 Modeling of Ionic Polymer-Metal Composites

$$\begin{aligned}
 &P(C^+(\zeta))[P(C^+(\zeta))]' - P(C^+(\zeta)) - \frac{k^2}{\lambda^2} (D^+)^2 \frac{(v^+ F)^2}{\kappa_e RT} C^+(\zeta)^2 \\
 &+ \frac{k^2}{\lambda^2} (D^+)^2 \frac{(v^+ F)^2}{\kappa_e RT} \frac{v^-}{v^+} C^- C^+(\zeta) = 0
 \end{aligned} \tag{5.25}$$

Setting $k = \sqrt{\frac{25a}{6}}$ and $\lambda = k^2$ where $a = (D^+)^2 \frac{v^+ (F)^2}{\kappa_e RT} v^- C^-$, Eq.(5.25) can be expressed as

$$P(C^+(\zeta))[P(C^+(\zeta))]' - P(C^+(\zeta)) = -\frac{6}{25} C^+(\zeta) + \frac{6}{25} \frac{v^+}{v^- C^-} C^+(\zeta)^2 \tag{5.26}$$

The parametric solution for Eq.(5.26) is

$$\begin{aligned}
 P(C^+(\zeta)) &= a_1 \tau^3 \sqrt{\pm(4\wp^3 - 1)} + 2a_1 \tau^2 \wp \\
 C^+(\zeta) &= 5a_1 \tau^2 \wp \\
 a_1 &= \pm \frac{v^- C^-}{5v^+}
 \end{aligned} \tag{5.27}$$

where $\tau = \int \frac{d\wp}{\sqrt{\pm(4\wp^3 - 1)}} - C_0$ and C_0 is an arbitrary coefficient. For the upper sign, the inversion of τ is the classic Weierstrass \wp -function for $\wp(\tau + C_0, 0, 1)$.

With Eq.(5.27), the cation concentration can be finally obtained as

$$\begin{aligned}
 C^+(z, t) &= \frac{25v^- C^-}{v^+} \wp(5e^{\zeta(z, t)/5} + C_1, 0, C_2) e^{2\zeta(z, t)/5} \\
 \zeta &= \sqrt{\frac{25a}{6}} [z - \int D^+ \frac{v^+ F}{RT} f(t) dt] + \frac{25a}{6} t
 \end{aligned} \tag{5.28}$$

The coefficients C_1 and C_2 can be determined by the boundary condition Eq.(5.20).

Chapter 5 Modeling of Ionic Polymer-Metal Composites

Introducing the normalized charge density which is

$$Q(z,t) = \frac{v^+ C^+(z,t) - v^- C^-}{v^- C^-}, \quad (5.29)$$

the thicknesses of the ABL and CBL can be calculated as (Nemat-Nasser, 2002),

$$L_A = \int_{-h/2}^0 Q(z,t) dz \quad (5.30)$$

$$L_C = 2 \left[\frac{h}{2} - \frac{\int_0^{h/2} z \cdot Q(z,t) dz}{L_A} \right] \quad (5.31)$$

With Eqs.(5.30) and (5.31), the bending moment due to the electric potential can subsequently be derived. In the following section, explicit bending moment solutions are obtained based on Nemat-Nasser's (2002) hybrid actuation model.

5.2.2 Bending moment

Considering that the volumetric strains of clusters and hence the axial strain of IPMC is affected by the water uptake, the moment rate is expressed as (Nemat-Nasser, 2002),

$$\dot{M}^e(t) = \int_{-h/2}^{h/2} Y_b \dot{\varepsilon}_x \cdot z dz = \int_{-h/2}^{h/2} Y_b \frac{1}{3} \frac{\dot{w}(z,t)}{1 + w(z,t)} \cdot z dz \quad (5.32)$$

where Y_b is the effective Young's modulus of boundary layers in IPMC, i.e., the Young's modulus of polyelectrolyte membrane; ε_x is the axial strain in the x direction; $w(z,t)$ is the function accounting for the water uptake in clusters; and the dot above all symbols denotes the first derivative with respect to time.

Chapter 5 Modeling of Ionic Polymer-Metal Composites

Completing the integration at the right hand side of Eq.(5.32) by considering the thickness of ABL and CBL and neglecting the small terms, the bending moment rate can be written as

$$\dot{M}^e(t) = -\frac{Y_b h}{6} \left[\frac{\dot{w}_A(z, t)}{1 + w_A(z, t)} L_A - \frac{\dot{w}_C(z, t)}{1 + w_A(z, t)} L_C \right] \quad (5.33)$$

where w_A and w_C are the water uptake at ABL and CBL, respectively.

Integrating both sides of Eq.(5.33) over time and considering the initial condition $M^e(0) = 0$ when $w_A(z, 0) = w_C(z, 0) = w_0$, where w_0 is the initial water uptake before the application of electric potential, the bending moment for the beam with width b can be obtained as

$$M^e = -\frac{Y_b b h L_A}{6} \{ \ln[1 + w_A(z, t)] - \beta \ln[1 + w_C(z, t)] + (1 - \beta)(\ln(1 + w_0)) \} \quad (5.34)$$

where $\beta = L_C / L_A$.

Since the bending strain is small, the change of water uptake in clusters is also small. Thus, the bending moment can be approximated by expanding the right hand side of Eq.(5.34) at w_0 using Taylor's series with the higher-order terms neglected, as

$$M^e = -\frac{Y_b b h L_A}{6(1 + w_0)} [(w_A(t) - \beta w_C(t)) - (1 - \beta)w_0] \quad (5.35)$$

Once the water uptakes w_A and w_C are obtained, the bending moment due to electric potential can be determined by Eq.(5.35). The water uptakes at ABL and CBL are governed by the following two equations (Nemat-Nasser, 2002),

Chapter 5 Modeling of Ionic Polymer-Metal Composites

$$\frac{\dot{w}_A(z,t)}{1+w_A(z,t)} = D_A t_A \quad (5.36)$$

$$\frac{\dot{w}_C(z,t)}{1+w_C(z,t)} = D_C \bar{t}_C \quad (5.37)$$

where D_A and D_C are the constant coefficients accounting for the diffusion in ABL and CBL, respectively; t_A and \bar{t}_C are the pressure in clusters in ABL and CBL, respectively, which are defined as

$$t_A = \Pi_A + p_{AA} + p_{ADD} + \sigma_r(a_0, t) \quad (5.38)$$

$$\bar{t}_C = \bar{\Pi}_C + \bar{p}_{DC} + \bar{p}_{CDD} + \bar{\sigma}_r(a_0, t) \quad (5.39)$$

where $\Pi_A(t)$, p_{AA} , p_{ADD} and $\sigma_r(a_0, t)$ are the osmotic pressure, anion-anion electrostatic stress, dipole-dipole interaction stress and elastic stress in the polymer matrix in ABL, respectively; and $\bar{\Pi}_C$, \bar{p}_{DC} , \bar{p}_{CDD} and $\bar{\sigma}_r(a_0, t)$ are the average values of osmotic pressure, dipole-cation interaction stress, dipole-dipole interaction stress and elastic stress in the polymer matrix in CBL. They are defined as follows,

$$\Pi_A(t) = \frac{\phi Q_B^- K_0}{w_A(t)} [2 - g(t)] \quad (5.40)$$

$$p_{AA} = \frac{g(t)}{18\kappa_A} \frac{(Q_B^-)^2 R_0^2}{[w_A(t)]^2} \quad (5.41)$$

$$p_{ADD} = \frac{1 - g(t)}{3\kappa_A} \frac{[\alpha_A(t)]^2}{[w_A(t)]^2} (Q_B^-)^2 \quad (5.42)$$

Chapter 5 Modeling of Ionic Polymer-Metal Composites

$$\bar{\Pi}_c(t) = \frac{\phi Q_B^- K_0}{w_c(t)} \left[2 + \frac{g(t)}{\beta} \right] \quad (5.43)$$

$$\bar{p}_{DC} = \frac{2(Q_B^-)^2 R_0 \alpha_c(t)}{9\kappa_c [w_c(t)]^{5/3}} g(t) \quad (5.44)$$

$$\bar{p}_{CDD} = \frac{(Q_B^-)^2}{3\kappa_c} \frac{[\alpha_c(t)]^2}{[w_c(x,t)]^2} [1 - g(t)] \quad (5.45)$$

and

$$\sigma_r(a_0, t) = -p_0 + K(w/w_i)^{-4/3} \quad (5.46)$$

where

$$p_0 = K \left(\frac{w_0}{w_i} \right)^{-4/3} + p_c \quad (5.47)$$

$$K = p_c \frac{1 + w}{w_i I_n - \left(\frac{w_i}{w} \right)^{4/3}} \quad (5.48)$$

$$p_c = \frac{\nu \phi Q_B^- K_0}{w} + \frac{\pm [\alpha_A(t)]^2 (Q_B^-)^2}{3k_e w^2} \quad (5.49)$$

$$w_i = \frac{n_0}{1 - n_0}, \quad I_n = \frac{1 + 2An_0}{n_0(1 + An_0)^{1/3}} - \frac{1 + 2A}{(1 + A)^{1/3}}, \quad A = \frac{w}{w_i} - 1 \quad (5.50)$$

where ϕ is the osmotic factor; $g(t)$ is the time variation function; Q_B^- is the anion charge density of the dry bare membrane, defined as

Chapter 5 Modeling of Ionic Polymer-Metal Composites

$$Q_B^- = \frac{\rho_B F}{EW_{ion}} \quad (5.51)$$

where ρ_B is the density of bare membrane and EW_{ion} is the equivalent weight of ion content,

$$EW_{ion} = \frac{EW_{H^+} - 1.008 + FW_{ion}}{SF} \quad (5.52)$$

EW_{H^+} is the equivalent weight of the dry ionomer in proton form, FW_{ion} is the formula weight of the cation used and SF is a scaling factor accounting for added electrode mass; $K_0 = \frac{RT}{F}$; R_0 is the initial cluster size in dry condition; κ_A and κ_C are the effective electric permittivity of the cluster in ABL and CBL respectively; $\alpha_A(t)$ and $\alpha_C(t)$ are the effective dipole length at ABL and CBL, respectively, which are governed by the following equation,

$$\pm[\alpha(t)]^2 = \begin{cases} a_1 \cdot w + a_2 & m_w \leq CN \\ \pm\left(\frac{7+6f}{7-6f}\right)^2 (a_1 \cdot w + a_2) & m_w > CN \end{cases} \quad (5.53)$$

where a_1 and a_2 are coefficients; w is the water uptake; m_w is the number of mole water per mole ion within a cluster defined as,

$$m_w = \frac{EW_{ion} w}{18v\rho_B} \quad (5.54)$$

and

$$f = \frac{m_w - CN}{m_w} \quad (5.55)$$

Chapter 5 Modeling of Ionic Polymer-Metal Composites

where CN is the coordination number; n_0 is the initial porosity of dry membrane; and $\nu = 2$. Detailed definitions of the above notations can be readily found in (Nemat-Nasser, 2002).

It is difficult to solve Eqs.(5.36) and (5.37) due to their nonlinearity. By transferring $1 + w_A(z, t)$ and $1 + w_C(z, t)$ to the right hand sides of Eqs.(5.36) and (5.37), respectively, and expanding their right hand sides at w_0 using Taylor's series with higher order terms neglected, two linear partial differential equations are obtained,

$$\frac{\partial w_A(z, t)}{\partial t} = F_A(w_0, t) + F_{A1}(w_0, t) \cdot (w_A - w_0) \quad (5.56)$$

$$\frac{\partial w_C(z, t)}{\partial t} = F_C(w_0, t) + F_{C1}(w_0, t) \cdot (w_C - w_0) \quad (5.57)$$

where $F_A(w_0, t) = D_A(1 + w_0)t_A(w_0, t)$; $F_{A1}(w_0, t) = \frac{\partial F_A(w_A, t)}{\partial w_A} \Big|_{w_A=w_0}$;

$F_C(w_0, t) = D_C(1 + w_0)t_C(w_0, t)$; and $F_{C1}(w_0, t) = \frac{\partial F_C(w_C, t)}{\partial w_C} \Big|_{w_C=w_0}$.

The solutions of w_A and w_C can be obtained from Eqs.(5.56) and (5.57) as

$$w_A(z, t) = e^{\int F_{A1} dt} \cdot (C_1 + \int e^{-\int F_{A1} dt} \cdot (F_A - F_{A1}w_0) dt) \quad (5.58)$$

$$w_C(z, t) = e^{\int F_{C1} dt} \cdot (C_2 + \int e^{-\int F_{C1} dt} \cdot (F_C - F_{C1}w_0) dt) \quad (5.59)$$

where C_1 and C_2 are the integration constants. After simplification, the solutions of water uptakes are

$$w_A(z, t) = [C_1 \bar{h}_A(t) - \frac{f_A}{f_{A1}} - \frac{f_A f_{A2}}{f_{A1}} \bar{h}_A(t) \int \frac{1}{\bar{h}_A(t)} dt] + w_0 \quad (5.60)$$

Chapter 5 Modeling of Ionic Polymer-Metal Composites

$$w_C(z, t) = [C_2 \hbar_C(t) - \frac{f_C}{f_{C1}} - \frac{f_C f_{C2}}{f_{C1}} \hbar_C(t) \int \frac{1}{\hbar_C(t)} dt] + w_0 \quad (5.61)$$

where

$$f_A = D_A (1 + w_0) \left[-\frac{\phi Q_B^- K_0}{w_0} + \frac{(Q_B^-)^2}{18 \kappa_A} \frac{R_0^2}{w_0^{4/3}} - \frac{(Q_B^-)^2}{3 \kappa_A} \frac{\pm (\alpha_A(w_0))^2}{w_0^2} \right] \quad (5.62)$$

$$f_{A1} = D_A \{ (1 + w_0) \left[\frac{\phi Q_B^- K_0}{w_0^2} - \frac{2(Q_B^-)^2}{27 \kappa_A} \frac{R_0^2}{w_0^{7/3}} + \frac{2(Q_B^-)^2}{3 \kappa_A} \frac{\pm [\alpha_A(w_0)]^2}{w_0^3} \right. \right. \\ \left. \left. - \frac{(Q_B^-)^2}{3 \kappa_A w_0^2} \frac{d \pm [\alpha_A(w_A)]^2}{dw_A} \Big|_{w_A=w_0} \right] + t_A(w_0, t) \} \quad (5.63)$$

$$f_{A2} = D_A (1 + w_0) \left[-K \frac{4}{3 w_i} \left(\frac{w_0}{w_i} \right)^{-7/3} \right] \quad (5.64)$$

$$f_C = D_C (1 + w_0) \left\{ \frac{\phi Q_B^- K_0}{\beta w_0} + \frac{2(Q_B^-)^2}{9 \kappa_C} \frac{R_0 \alpha_C(w_0)}{w_0^{5/3}} - \frac{(Q_B^-)^2}{3 \kappa_C} \frac{\pm (\alpha_C(w_0))^2}{w_0^2} \right\} \quad (5.65)$$

$$f_{C1} = D_C \{ (1 + w_0) \left(-\frac{\phi Q_B^- K_0}{\beta w_0^2} - \frac{10}{3} \frac{(Q_B^-)^2}{9 \kappa_C} \frac{R_0 \alpha_C(w_0)}{w_0^{7/3}} \right. \right. \\ \left. \left. + \frac{2(Q_B^-)^2}{9 \kappa_C} \frac{R_0}{w_0^{5/3}} \frac{d \alpha_C(w_A)}{dw_A} \Big|_{w_A=w_0} \right. \right. \\ \left. \left. + \frac{2(Q_B^-)^2}{3 \kappa_C} \frac{\pm [\alpha_C(w_0)]^2}{w_0^3} - \frac{(Q_B^-)^2}{3 \kappa_C w_0^2} \frac{d \pm [\alpha_C(w_A)]^2}{dw_A} \Big|_{w_A=w_0} \right) + t_C(w_0, t) \} \quad (5.66)$$

$$f_{C2} = D_C (1 + w_0) \left[-K \frac{4}{3 w_i} \left(\frac{w_0}{w_i} \right)^{-7/3} \right] \quad (5.67)$$

$$\hbar_{(\bullet)}(t) = e^{\int [f_{\bullet 1} g(t) + f_{\bullet 2}] dt} \quad (5.68)$$

Chapter 5 Modeling of Ionic Polymer-Metal Composites

where the dot in the subscript stands for either A or C.

As $f_{\bullet 2}$ is negative, with the increase of time, $\dot{h}_{(\bullet)}(t)$ will diminish. For the steady state, i.e., t is sufficiently large, the following relation stands,

$$\dot{h}_{(\bullet)}(t) \int \frac{1}{\dot{h}_{(\bullet)}(t)} dt = -e^{\frac{f_{A1}}{\Omega} e^{j(\Omega t - \pi/2)}} / f_{\bullet 2} \quad (5.69)$$

Using the approximation of Eq.(5.69), Eqs.(5.60) and (5.61) can be further simplified as

$$w_A(z, t) = C_1 \dot{h}_A(t) + \frac{f_A}{f_{A1}} [e^{\frac{f_{A1}}{\Omega} e^{j(\Omega t - \pi/2)}} - 1] + w_0 \quad (5.70)$$

$$w_C(z, t) = C_2 \dot{h}_C(t) + \frac{f_C}{f_{C1}} [e^{\frac{f_{C1}}{\Omega} e^{j(\Omega t - \pi/2)}} - 1] + w_0 \quad (5.71)$$

Considering the initial conditions,

$$w_A(z, 0) = w_0, \quad w_C(z, 0) = w_0, \quad g(0) = 0 \quad (5.72)$$

the coefficients C_1 and C_2 can be obtained from Eqs.(5.56) and (5.57) as

$$C_1 = -\frac{f_A}{f_{A1}} [e^{\frac{f_{A1}}{\Omega} e^{-j\pi/2}} - 1] / \dot{h}_A(0) \quad (5.73)$$

$$C_2 = -\frac{f_C}{f_{C1}} [e^{\frac{f_{C1}}{\Omega} e^{-j\pi/2}} - 1] / \dot{h}_C(0) \quad (5.74)$$

As $\dot{h}_{(\bullet)}(t)$ will diminish with time, for the steady state vibration, $C_1 \dot{h}_A(t)$ and $C_2 \dot{h}_C(t)$ will eventually vanish. Finally, the solutions of water uptake functions are

Chapter 5 Modeling of Ionic Polymer-Metal Composites

$$w_A(z, t) = \frac{f_A}{f_{A1}} \left[e^{\left(\frac{f_{A1}}{\Omega} e^{j(\Omega t - \pi/2)} \right)} - 1 \right] + w_0 \quad (5.75)$$

$$w_C(z, t) = \frac{f_C}{f_{C1}} \left[e^{\left(\frac{f_{C1}}{\Omega} e^{j(\Omega t - \pi/2)} \right)} - 1 \right] + w_0 \quad (5.76)$$

Since the time variation of $w_A(z, t)$ and $w_C(z, t)$ should be $e^{j(\Omega t - \pi/2)}$, Eqs.(5.75) and (5.76) can be approximated as

$$w_A(z, t) = \frac{f_A}{f_{A1}} \left(e^{\frac{f_{A1}}{\Omega}} - 1 \right) e^{j(\Omega t - \pi/2)} + w_0 \quad (5.77)$$

$$w_C(z, t) = \frac{f_C}{f_{C1}} \left(e^{\frac{f_{C1}}{\Omega}} - 1 \right) e^{j(\Omega t - \pi/2)} + w_0 \quad (5.78)$$

Using the solutions of water uptake in Eqs.(5.77) and (5.78), the bending moment generated by the IPMC can be obtained from Eq.(5.35).

$$M^e = -\frac{Y_b b h L_A}{6(1 + w_0)} \left[\frac{f_A}{f_{A1}} \left(e^{\frac{f_{A1}}{\Omega}} - 1 \right) - \frac{\beta f_C}{f_{C1}} \left(e^{\frac{f_{C1}}{\Omega}} - 1 \right) \right] e^{j(\Omega t - \pi/2)} \quad (5.79)$$

It is worth noting that Eq.(5.79) is an explicit expression of bending moment including the effects of osmotic, electrostatic and elastic stresses of IPMC. This equation provides a convenient way to estimate the bending moment of IPMC at a given hydration rate. The frequency of the applied electric potential Ω appears in the expression of bending moment. It is evident that with the increase of driving frequency Ω , the generative bending moment and therefore the vibration amplitude of IPMC decreases. This conclusion agrees with the experimental observations by Shahinpoor and Kim (2001). In addition, a phase lag between the bending moment and the input signal is observed, i.e., $\delta_0 = \pi/2$. It is noted that this phase lag is obtained without considering the viscous properties of solvent. For different solvent, the phase lag should vary. To include the effect of viscous property of solvent in the

Chapter 5 Modeling of Ionic Polymer-Metal Composites

IPMC, Eqs.(5.32), (5.36) and (5.37) need modifications. The effect of viscosity of solvent can also be reflected in the overall damping coefficient of an IPMC sample which can be evaluated through experiments.

Since the thicknesses of the ABL and the CBL are derived from the condition of static electric potential and multiplied by the time variation function, they may be inaccurate for a high frequency electric field, especially for the CBL. This may result in an overestimation of bending moment from Eq.(5.79) since the time required for cation redistribution is neglected. However, as the time required for cation redistribution is very short, for low driving frequency, cations should have ample time to achieve a quasi-equilibrium state. Thus, Eq.(5.79) is more accurate for low frequency electric fields.

When Ω is very small, e.g., the DC signal is applied, Eq.(5.79) is not applicable anymore. However, the bending moment for this case can be easily obtained by setting the time variation function $g(t)$ in Eqs.(5.56) and (5.57) to unity. The bending moment under a DC signal is

$$M^e = -\frac{Y_b b h L_A}{6(1+w_0)} \left[\frac{f_A}{f_{A1} + f_{A2}} (e^{(f_{A1}+f_{A2})t} - 1) - \frac{\beta f_C}{f_{C1} + f_{C2}} (e^{(f_{C1}+f_{C2})t} - 1) \right] \quad (5.80)$$

For the transverse vibration of the IPMC beam, Eq.(5.79) should be used. For the static signal input, the bending moment is calculated from Eq.(5.80).

5.3 Validation and discussions

The essential assumption in the simplification procedure in Section 5.2.2 is small strains in clusters when actuation. The simplification procedure is to apply Taylor's series expression to Eqs. (5.36) and (5.37). Therefore, it is important to compare the results of the simplified solutions with the numerical solutions of Eqs. (5.36) and (5.37) and test whether the assumption is valid. As Eqs. (5.36) and (5.37) have the

Chapter 5 Modeling of Ionic Polymer-Metal Composites

same format, so do Eqs. (5.77) and (5.78), only Eqs. (5.36) and (5.77) are calculated and compared. The numerical solution to Eq. (5.36) is obtained by using the MATLAB function ode45. Fig 5.3 shows the results of water uptakes obtained from Eqs.(5.77) and (5.36). The parameters used are listed in Table 5.1. It is evident that the analytical solution Eq.(5.77) and the numerical solution of Eqs.(5.36) match well except that the peak values are slightly different. A $\pi/2$ lag is also observed by comparing the driving signal and the water uptake solution. This result indicates that the simplification procedure is valid.

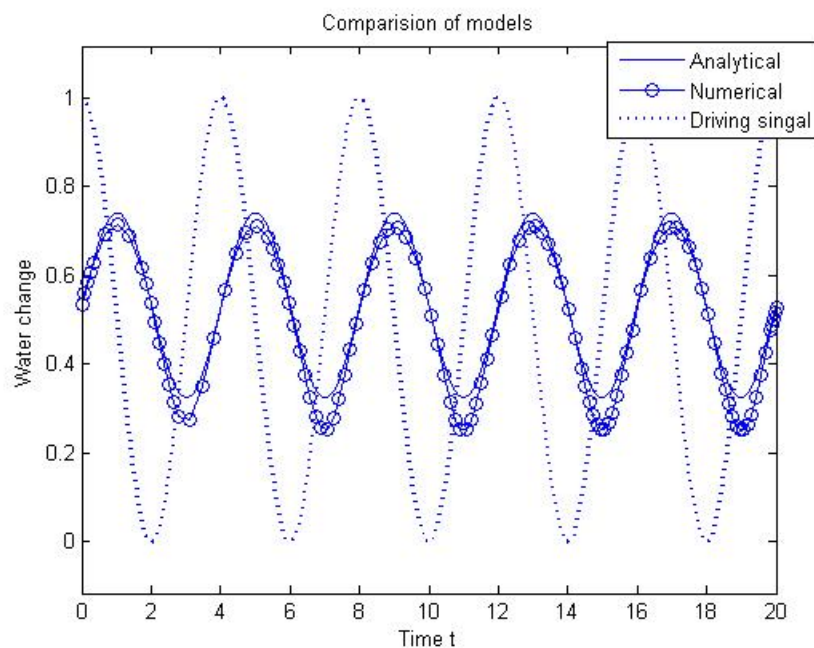


Figure 5.3 Comparison between analytical and numerical solutions

Before the above solutions can be used, the bending moment solution obtained in Section 5.2 will be validated first by comparing the tip displacement of a cantilevered beam with the results obtained by Nemat-Nasser (2002). Consider a Nafion based cantilevered IPMC beam in Li^+ form with length 18 mm, width 2 mm and thickness $224\text{ }\mu\text{m}$ as shown in Fig.5.4. The plating metal is platinum and the thickness of electrode is $6\text{ }\mu\text{m}$ for both top and bottom surfaces of the IPMC beam. Assume that the initial water uptake of IPMC is $w_0 = 0.533$ and the electric potential is a 1-volt DC signal. For simplicity, the viscous damping of the IPMC is

Chapter 5 Modeling of Ionic Polymer-Metal Composites

set as zero. Other material properties used in calculation are listed in Table 5.1. All the above parameters are the same as in (Nemat-Nasser, 2002).

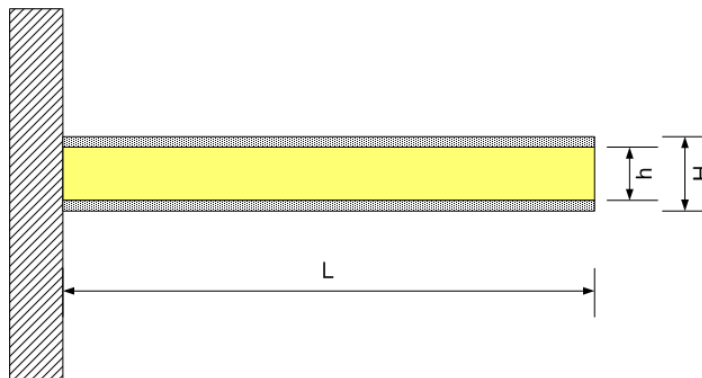


Figure 5.4 Configuration of an IPMC cantilevered beam

Table 5.1 Parameters, symbols and values for an IPMC sample with Li^+ as cation

Parameter	Symbol	Value	Parameter	Symbol	Value
IPMC Density	ρ	3385 kg/m ³	Temperature	T	300 K
Gas constant	R	8.3143 J/mol/K	Initial porosity	n_0	0.01
Faraday's constant	F	96487 C/mol	Inner radius of cluster at w_0	a	1.6×10^{-9} m
Bare membrane density	ρ_B	2.01×10^3 kg/m ³	Capacitance	Cap	12 F/m
Platinum density	ρ_p	21.45×10^3 kg/m ³	Effective permittivity at ABL	κ_A	1.7852×10^{-10} F/m
Effective permittivity at CBL	κ_C	5.31×10^{-11} F/m	Osmotic coefficient	ϕ	1

Chapter 5 Modeling of Ionic Polymer-Metal Composites

Coordination Number of Li^+	CN	6	Equivalent weight of bare Nafion in proton form	EW_{H^+}	1100 g/mol
Formula weight of Li^+	FW_{Li^+}	6.94 g/mol	Effective dipole length coefficient a_1	a_1	1.728×10^{-20}
Effective dipole length coefficient a_2	a_2	-0.0778×10^{-20}	Concentration factor	A_B	0.5
Coefficient D_A	D_A	1.0×10^{-8}	Dynamic solvation number	SN	0
Young's modulus of platinum	Y_M	1.50×10^{11} N/m ²	Mass scaling factor	SF	0.623

Since the signal is DC, the bending moment can be obtained from Eq.(5.80). The normalized tip displacement of the cantilevered beam can be expressed as

$$\frac{u_3}{L} = \frac{M^e L}{2YI} \quad (5.81)$$

where Y is the Young's modulus of the IPMC beam and I is the moment of inertia.

Fig.5.5 shows the comparison of normalized tip displacement from Eqs.(5.80) and (5.81) and the results in Nemat-Nasser (2002). It can be found that the present model is in good accordance with the data in Nemat-Nasser (2002) at the initial deformation stage. The final displacements after long time span also closely match to each other. Since Eq.(5.80) does not take into account the relaxation of the IPMC beam, the relaxation stage does not match well. But this does not affect the accuracy of Eq.(5.79) since it accounts for the continuous vibration of IPMC beam where the relaxation effect is negligible.

Chapter 5 Modeling of Ionic Polymer-Metal Composites

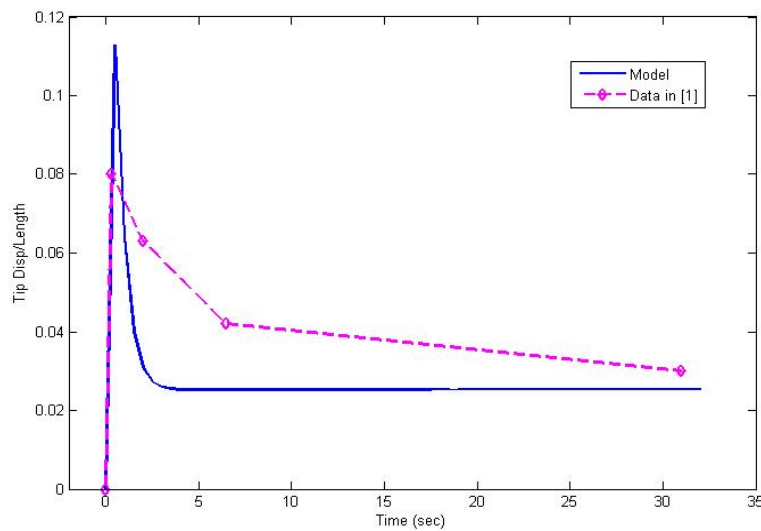


Figure 5.5 Comparison between calculated displacement and data in Nemat-Nasser (2002)

Despite the tip displacement of IPMC cantilevered beam, blocked force is generally another value of interest. The blocked force can be defined as a force required to prevent a deflection. The blocked force for an IPMC cantilevered beam can be estimated by considering the beam subjected to a point force at the tip. The blocked force can balance the bending moment caused by the electric field such that the tip displacement is zero. By using the Carstigliano's theorem, the blocked force can be derived as

$$F_b = \frac{3M^e}{2L} \quad (5.82)$$

For the 1-volt DC potential, the maximum blocked force is equivalent to 0.033 gram, which is about 1.211 times the self-weight of the IPMC beam. When the electric potential increases to 5 volts, the ratio of the blocked force to the beam weight is 4.37. This ratio is comparable with the experimental result obtained by Shahinpoor and Kim (2005) for the thin gold electrode IPMC. In their experiment, a 2 mm thick IPMC strip of weight 0.24 gram developed 1.2 gram force under 5-volt potential, where the force-weight ratio is 5.0. This comparison indicates that the results obtained are reasonable.

Chapter 5 Modeling of Ionic Polymer-Metal Composites

The above calculation validates the bending moment expression for static electric potential. To validate the bending moment expression for dynamic condition, consider a Nafion based IPMC cantilevered beam with length 30 mm and thickness 224 μm . The applied electric potential is a 1-volt sinusoidal signal with frequency of 0.25 Hz. The cation type is Na^+ and the solvent is water. Other parameters are shown in Table 5.2. When the electric potential is on, the IPMC cantilevered beam will vibrate at the driving frequency.

Table 5.2 Parameters, symbols and values for an IPMC sample with Na^+ as cation

PARAMETER	SYMBOL	VALUE	PARAMETER	SYMBOL	VALUE
Young's modulus of hydrated polymer	Y_b	89 MPa	Temperature	T	300 K
Young's modulus of IPMC	Y	0.186 GPa	Initial porosity	n_0	0.01
IPMC Density	ρ	3385 kg/m^3	Radius of cluster	a	1.65 nm
Gas constant	R	8.3143 J/mol K	Capacitance	Cap	15 F/m^2
Farad's constant	F	96487 C/mol	Effective permittivity at anode boundary	κ_A	2.1462×10^{-10} F/m
Effective permittivity at cathode boundary layer	κ_C	5.31×10^{-11} F/m	Formula weight of Na^+	FW_{Na^+}	23 g/mol
Bare membrane density	ρ_B	2010 kg/m^3	Equivalent weight of proton	EW_{H^+}	1100 g/mol
Osmotic coefficient	ϕ	1	Diffusion coefficient	D_A	10^{-2}
Effective dipole length coefficient a_1	a_1	1.5234×10^{-20}	Effective dipole length coefficient a_2	a_2	-0.0703×10^{-20}

Chapter 5 Modeling of Ionic Polymer-Metal Composites

Coordination number	CN	4.5	Solvation number	SN	0
------------------------	----	-----	---------------------	----	---

The transverse vibration of a cantilevered beam is governed by the following motion equation as

$$YI \frac{\partial^4 w}{\partial x^4} + \rho A \frac{\partial^2 w}{\partial t^2} = f(x, t) \quad (5.83)$$

where ρ is the material density; A is the cross section area and $f(x, t)$ is the load effect due to the IPMC actuation which is

$$f(x, t) = M_0 [\delta'(x - 0) - \delta'(x - L)] e^{j\Omega t} \quad (5.84)$$

where M_0 is the time independent part of Eq.(5.79).

Eq.(5.83) can be solved by the method of separation of variables. It is assumed that the solution is in the following form,

$$w = \sum_{n=1}^{\infty} A_n X_n(x) e^{j\Omega t} \quad (5.85)$$

where $X_n(x) = [\cos(k_n x) - \cosh(k_n x) - \sigma_n [\sin(k_n x) - \sinh(k_n x)]]$;

$\sigma_n = \frac{\cos(k_n L) + \cosh(k_n L)}{\sin(k_n L) + \sinh(k_n L)}$ and k_n is determined by the frequency equation

$$\cos(k_n L) \cosh(k_n L) = -1 \quad (5.86)$$

Substituting Eq.(5.85) into Eq.(5.83) and using the orthogonal properties of normal mode, the coefficient A_n can be obtained as

Chapter 5 Modeling of Ionic Polymer-Metal Composites

$$A_n = \frac{M_0}{L} \{2 \cdot (-1)^n + k_n [-\sin(k_n L) - \sinh(k_n L) + \sigma_n (\cos(k_n L) - \cosh(k_n L))]\} / (YIk_n^4 - \rho A \Omega^2) \quad (5.87)$$

Thus the solution to the IPMC cantilever beam vibration is obtained.

Figure 5.6 shows the deflection curves of the IPMC cantilever beam at three different time points, $t=1/12f$, $t=1/6f$ and $t=1/4f$, where f is the driving frequency which is 0.25 Hz. It is observed that the maximum tip displacement is 4.2% of the beam length. In Nemat-Nasser & Wu (2006), the experimental test showed that the maximum tip displacement of a cantilever beam of the same dimension under the same electric potential is 3.6% of the beam length. Considering the length of beam, the difference in vibration amplitude is only 0.18 mm. As the experimental data of IPMC generally vary a lot from case to case, the calculation result can be viewed as acceptable. This calculation also validates the proposed model.

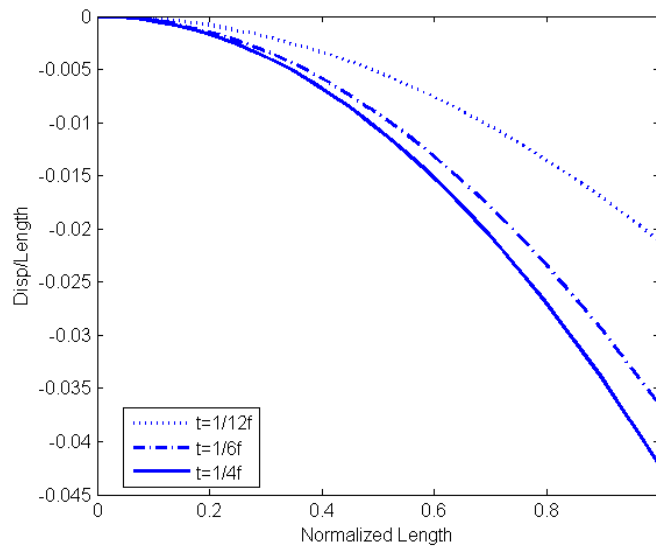


Figure 5.6 IPMC cantilever beam deflections at $t=1/(12f)$, $t=1/(6f)$ and $1/(4f)$

Chapter 5 Modeling of Ionic Polymer-Metal Composites

5.4 Conclusions

In this chapter, explicit bending moment expressions were derived from the Nemat-Nasser's hybrid actuation model for both dynamic and static electric potentials. Comparisons with the numerical solution and the experimental results in literature showed that the model was reasonably good in accuracy. The formulae provide an easy way to estimate the bending capacity of IPMC materials at a given hydration rate. The bending moment expressions will be used in the next chapter to model IPMC based structures for biomedical applications.

Chapter 6 Applications of Ionic Polymer-Metal Composites

6.1 Introduction

IPMC as an ionic EAP offers many advantages over the conventional EAP materials, such as good compliance, light weight, low operation voltage and capability of working in aqueous environments. These properties make it promising for numerous applications in biomedical, naval, robotic and microelectromechanical system (MEMS) engineering (Shahinpoor and Kim, 2005). One of the important applications of IPMCs is in the biomedical related instruments which contact with human organs or tissues, such as artificial ventricular muscles, surgical tools and active scleral bands. The configuration of IPMC materials could be in various forms including bands, rings or shells.

In this chapter, possible applications of IPMC material for biomedical engineering are explored. Three prototype models, i.e., an IPMC beam on human tissues, an IPMC ring with elastic medium and an IPMC cylindrical shell with flowing fluid, are developed. The explicit bending moment expressions obtained in Chapter 5 are used in modeling. Examples are presented for illustration.

6.2 IPMC beam structure on human tissues

One of the important applications of smart materials in biomedical engineering is the minimally invasive surgery (MIS) tools which contact with human tissues of organs. These surgery tools are generally expected to apply forces on tissues and organs or change shapes to adapt to small incisions. Many of the MIS tools are in the form of strips or beams and operated in dynamic electric potentials.

Chapter 6 Applications of Ionic Polymer-Metal Composites

In this section, an analytical model is developed to depict the vibration response of a simply-supported IPMC beam bonded on an elastic foundation under an alternative electric field. The elastic foundation is employed to simulate the effect of human tissues. Eq.(5.79) is incorporated into the motion equation to account for the applied alternative electric field. A closed-form solution is obtained to describe the transverse vibration of the IPMC beam subjected to the applied electric field. Based on this solution, the pressure generated on human tissue is calculated by numerical integration. To maximize the beam deflection and the total pressure generated, the optimal location and length of the single electrode on the IPMC beam are discussed. To increase the flexibility of the IPMC beam and the variety of beam motion, multiple-electrodes on the IPMC beam are also considered. The deflection curve and generative pressure of the IPMC beam with multiple electrodes are obtained. The developed model is useful not only for the biomedical devices that employ IPMC materials but also for any other applications that utilize the vibration of IPMC materials.

6.2.1 Modeling of IPMC beam on human tissues

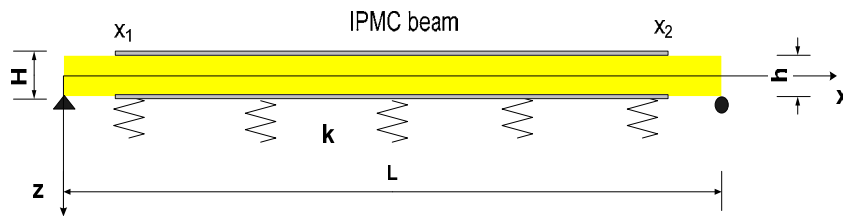


Figure 6.1 Configuration of an IPMC beam on human tissues

As shown in Fig.6.1, a Nafion based IPMC beam of length L , thickness H and width b is studied. The IPMC beam is chemically plated with platinum electrode on both sides, and x_1 and x_2 are the coordinates of the two ends of the electrode. The thickness of Nafion part of IPMC is denoted as h . The IPMC beam is assumed to be simply supported on human tissue. The effect of tissue is modeled as a Winkler foundation with stiffness k . Assume that the alternative electric potentials

Chapter 6 Applications of Ionic Polymer-Metal Composites

at top and bottom surfaces are $-\varphi_0 e^{j\Omega t} / 2$ and $\varphi_0 e^{j\Omega t} / 2$, respectively, where φ_0 is the time-independent magnitude of electric potential, Ω is the angular frequency and j is the imaginary unit. Due to the redistribution of cations and associated water under the applied electric field, the IPMC beam will vibrate at a frequency the same as that of the applied electric potential.

The motion equation of the beam can be obtained from Euler-Bernoulli's beam theory as (Soedel, 2004),

$$\frac{\partial^2 [M(x,t) - M^e(x,t)]}{\partial x^2} + \rho A \frac{\partial^2 u_3(x,t)}{\partial t^2} + c_v \frac{\partial u_3(x,t)}{\partial t} + k \cdot u_3(x,t) = 0 \quad (6.1)$$

where $M(x,t)$ is the bending moment in the IPMC beam; $M^e(x,t)$ is the bending moment due to the electric field; ρ is the material density of the IPMC beam; A is the cross-sectional area of the beam; c_v is the viscous damping coefficient of the IPMC beam and $u_3(x,t)$ is the transverse displacement of the beam.

Transferring the term due to electric field to the right hand side and utilizing the strain-stress and strain-displacement relations, the following equation can be obtained

$$YI \cdot \frac{\partial^4 u_3}{\partial x^4} + \rho A \frac{\partial^2 u_3}{\partial t^2} + c_v \frac{\partial u_3}{\partial t} + k u_3 = \frac{\partial^2 M^e(x,t)}{\partial x^2} \quad (6.2)$$

where Y and I are the Young's modulus and moment of inertia of the beam, respectively. Since the IPMC beam will undergo a pure bending at the frequency of applied electric potential, $M^e(x,t)$ can be expressed as

$$M^e(x,t) = M_0 \cdot [H(x - x_1) - H(x - x_2)] e^{j(\Omega t - \delta_0)} \quad (6.3)$$

Chapter 6 Applications of Ionic Polymer-Metal Composites

where $H(\cdot)$ is the Heaviside function; M_0 is the time-independent amplitude of bending moment and $\delta_0 = \pi/2$ is the phase difference between bending moment and applied electric potential which are determined by Eq.(5.79).

Using the method of separation of variables, the solution of Eq.(6.2). can be derived as

$$u_3(x, t) = \sum_{m=1}^{\infty} - \frac{2m\pi M_0^e [\cos(\frac{m\pi x_1}{L}) - \cos(\frac{m\pi x_2}{L})]}{\rho A L^2 \omega_m^2 \sqrt{(1 - \Omega^2 / \omega_m^2)^2 + [c_v \Omega / (\rho A \omega_m^2)]^2}} \sin(\frac{m\pi x}{L}) e^{j(\Omega t - \delta_m)} \quad (6.4)$$

where $\omega_m = \sqrt{(YI \cdot (m^4 \pi^4) / L^4 + k) / \rho A}$ is the natural frequency of the beam for zero damping; $\delta_m = \delta_0 + \tan^{-1} \frac{c_v \Omega / \rho A}{\omega_m^2 - \Omega^2}$ is the phase lag due to the viscous damping.

With the solution of Eq.(6.4), the total force generated by the IPMC beam can be readily obtained by

$$p = k \cdot \int_0^L u_3 H(u_3) dx \quad (6.5)$$

The computation of total pressure can be implemented by numerical integration.

6.2.2 Illustrative examples and discussions

6.2.2.1 Illustrative examples

Consider a Nafion based IPMC beam in Li^+ form with length 18mm, width 2 mm and thickness 224 μm . The plating metal is platinum and the thickness of electrode is 6 μm for both top and bottom surfaces of the IPMC beam. Assume that the initial water uptake of IPMC is $w_0 = 0.533$ and the electric potential is a 1-volt AC signal.

Chapter 6 Applications of Ionic Polymer-Metal Composites

For simplicity, the viscous damping of the IPMC is set as zero. Other material properties used in calculation are listed in Table 5.1.

The AC signal is a 1-volt sinusoidal potential with frequency of 0.25 Hz. The stiffness of tissue is set as 15 kPa, which is within the range of experimental data of the passive stiffness of hamster trabecula (Abe et al, 1996). By using Eqs.(6.4), the beam deflection curve at any time can be obtained. The total terms of summation used in Eqs.(6.4) is $m = 100$. Figs. 6.2 and 6.3 respectively illustrate the IPMC beam deflection and the pressure distribution on human tissue when the electric potential is at its maximum. It can be observed that the maximum deflection of IPMC beam is in the order of 0.01 mm and the maximum pressure is around 120 Pa. The total pressure can be evaluated by Eq.(6.5), which is 0.2298 gram for the pressure distribution in Fig.6.3. This pressure is equivalent to 0.4693 mmHg on the human tissue beneath the beam. Figs.6.4 and 6.5 show the beam deflection and pressure distribution for the tissue stiffness varying from 0 kPa to 20 kPa. It is evident that with the increase of stiffness, the displacement reduced. The maximum deflection of beam for zero foundation stiffness is about 0.45 mm. However, for the pressure distribution, the higher the tissue stiffness, the larger the maximum pressure value is. It is also noted that the displacement curve of beam for low stiffness (0 and 1kPa) is different from that of high stiffness (above 5kPa).

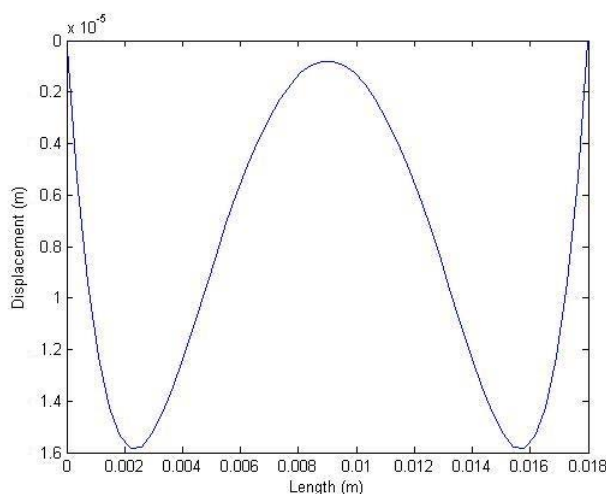


Figure 6.2 Deflection of IPMC beam under 1 volt sinusoidal potential ($k=15$ kPa)

Chapter 6 Applications of Ionic Polymer-Metal Composites

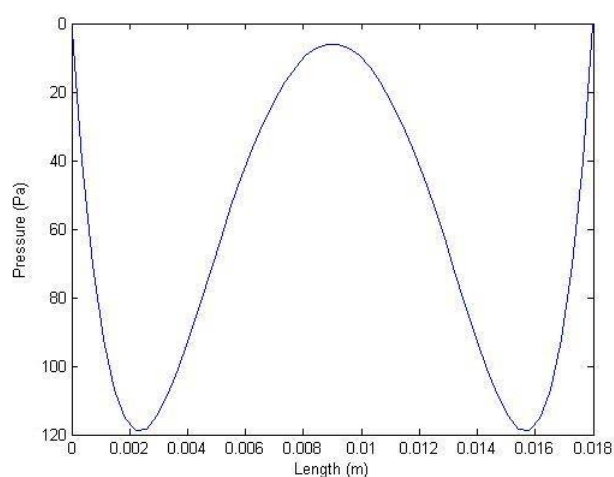


Figure 6.3 Pressure distribution on human tissue under 1 volt sinusoidal potential ($k=15\text{kPa}$)

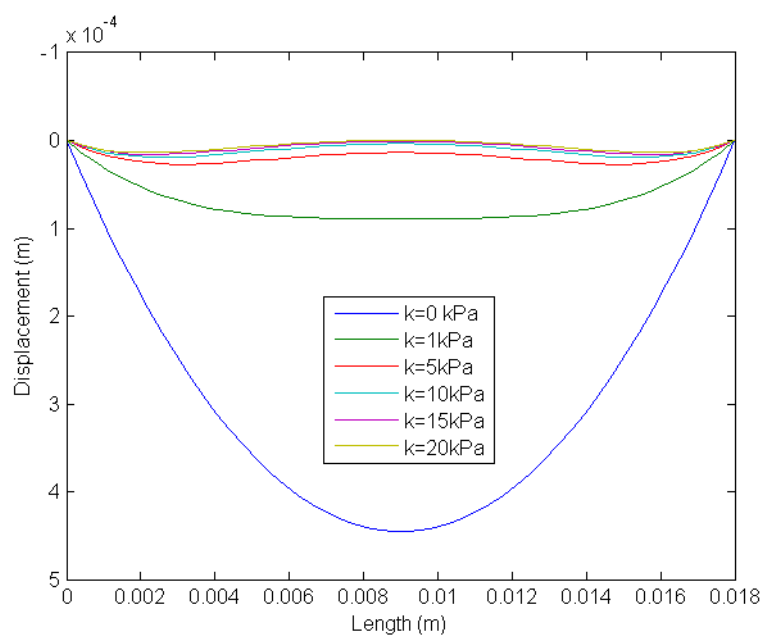


Figure 6.4 Displacements vs. tissue stiffness.

Chapter 6 Applications of Ionic Polymer-Metal Composites

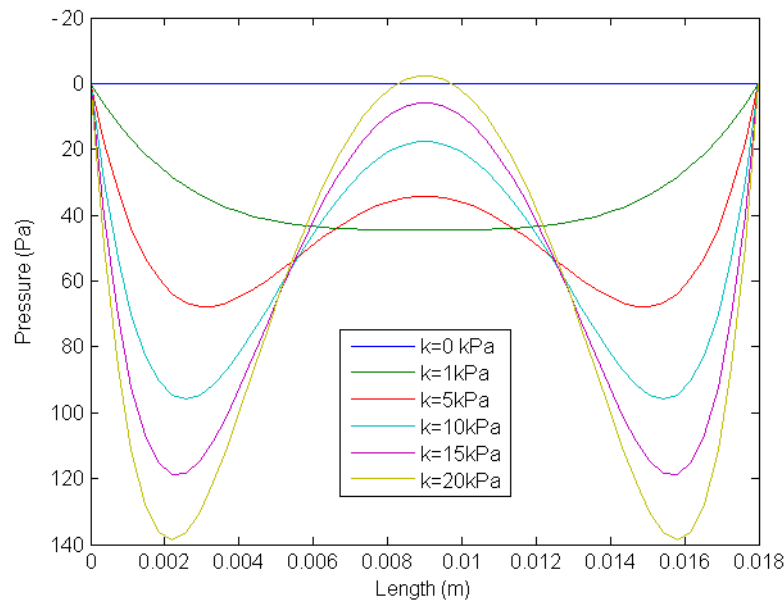


Figure 6.5 Pressure vs. tissue stiffness

6.2.2.2 Optimal electrode length

It is evident from Eq.(6.4) that for different values of x_1 and x_2 , which determine the position and the length of the electrode, the maximum transverse displacement and therefore the generative pressure is different. For biomedical applications of IPMCs, maximum deflection and maximum generative pressure may be required for different purposes. For examples, maximum pressure is needed for heart compression bands and maximum deflection is sometime necessary for surgical tools. To generate the maximum deflection or pressure, optimal values of coordinates of x_1 and x_2 can be calculated using the developed model. For ease of computation, we assume the stiffness of beam does not change due to the changes of electrode location and length. In Chapter 4, the optimal placement of a PZT actuator on a rectangular plate in terms of maximizing vibration amplitude has been studied. The natural frequency is used as a measure to determine the optimal location of PZT actuator. As an IPMC is generally actuated at low frequency, far below the first natural frequency of the beam, the predominant vibration mode is the first mode. Therefore, to maximize the first vibration mode, the values of x_1 and x_2

Chapter 6 Applications of Ionic Polymer-Metal Composites

should maximize the absolute value of $\cos(\frac{\pi x_1}{L}) - \cos(\frac{\pi x_2}{L})$, where $x_1 \neq x_2$, $x_1, x_2 \in [0, L]$. It is obvious that the solutions are $x_1 = 0$ and $x_2 = L$ or vice versa.

However, when the elastic foundation beneath the IPMC beam is stiff, all vibration modes will have similar and small contributions to the overall vibration. In this condition, the first mode may not appear to be dominant, such as the deflection curve in Fig.6.2. Fig.6.6 shows the influence of the electrode coordinates x_1 and x_2 on the maximum beam deflection for the case of Fig.6.2. The maximum beam deflection of any (x_1, x_2) combination is denoted by the color of the point which can be read from the color bar. It is observed that the optimal location of the electrode is at either end of the beam with the electrode length of $0.25L$ to $0.39L$, i.e., 4.5 mm to 7.0 mm. For higher foundation stiffness, say 40 kPa, the value of optimal length reduces. Fig.6.7 shows the relationship between the electrode coordinates and the maximum beam deflection for this case. The optimal electrode position is also close to either end of beam with the electrode length of $0.22L$ to $0.27L$. Fig.6.8 shows the optimal electrode coordinates for the IPMC beam with foundation stiffness 0.9 kPa. It is obvious that the optimal length of electrode is equal to the length of beam.

Therefore it can be concluded that for soft foundations, the electrode should cover the entire beam surface, while for stiff foundations, the electrode should be located near either end of the beam and the length of the electrode does not necessarily cover the entire beam.

Another issue is the optimal location and length of the electrode in terms of maximizing the total pressure. Figs. 6.9 to 6.11 illustrate the relationship between the electrode coordinates and the generative pressure for foundation stiffness of 0.9 kPa, 15 kPa and 40 kPa, respectively. All the results indicate that the optimal electrode length is equal to the length of beam. Thus, IPMC beam with fully covered electrode will generate the largest force compared to other electrode configuration for the simply supported condition.

Chapter 6 Applications of Ionic Polymer-Metal Composites

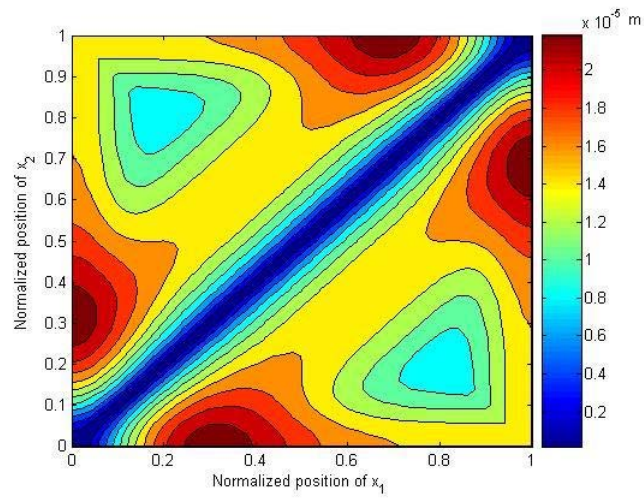


Figure 6.6 Relationship between electrode coordinates and maximum beam deflection ($k=15$ kPa)

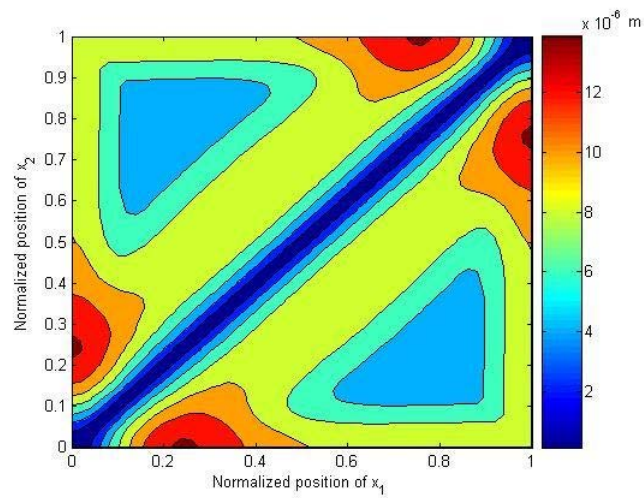


Figure 6.7 Relationship between electrode coordinates and maximum beam deflection ($k=40$ kPa)

Chapter 6 Applications of Ionic Polymer-Metal Composites

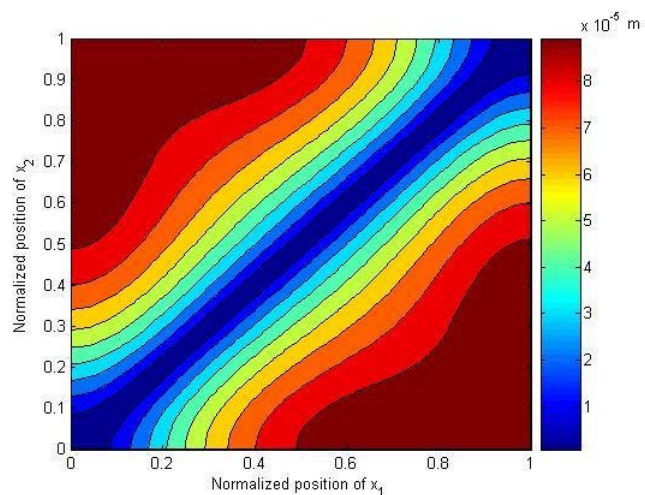


Figure 6.8 Relationship between electrode coordinates and maximum beam deflection ($k=0.9$ kPa)

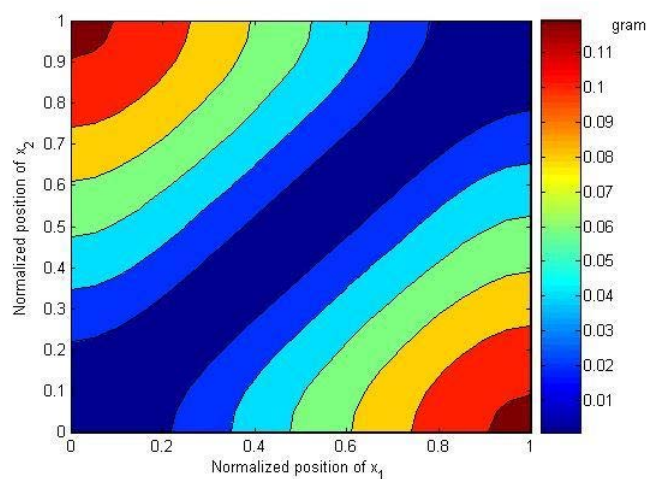


Figure 6.9 Relationship between electrode coordinates and pressure ($k=0.9$ kPa)

Chapter 6 Applications of Ionic Polymer-Metal Composites

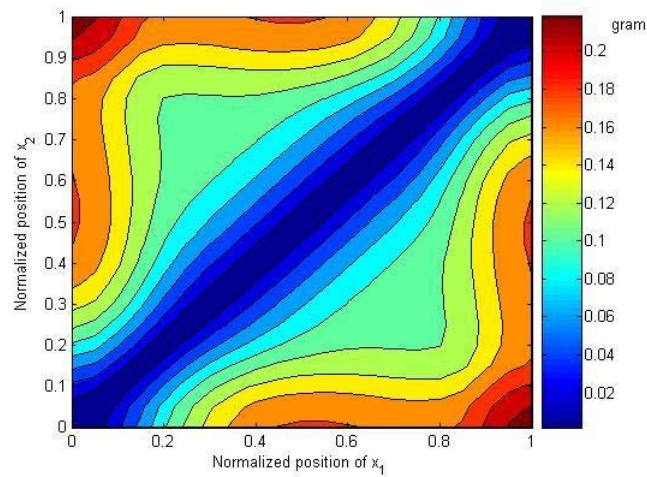


Figure 6.10 Relationship between electrode coordinates and pressure ($k=15$ kPa)

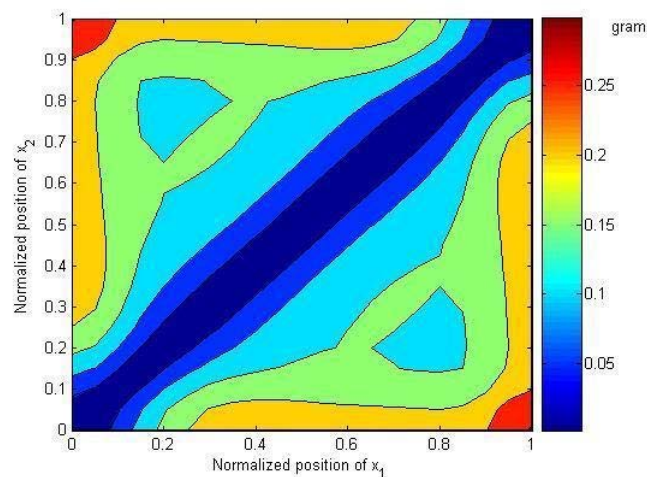


Figure 6.11 Relationship between electrode coordinates and pressure ($k=40$ kPa)

6.2.2.3 Multiple electrodes

If the IPMC beam is discretely plated with multiple electrodes and the applied electric potentials are different for each electrode, the IPMC beam will be more

Chapter 6 Applications of Ionic Polymer-Metal Composites

flexible. In such condition, the IPMC beam could be able to produce larger pressure or displacement on human tissue. For this case, Eq.(6.4) should be modified as

$$u_3(x, t) = \sum_{n=1}^s \sum_{m=1}^{\infty} - \frac{2m\pi M_0^e [\cos(\frac{m\pi x_{n1}}{L}) - \cos(\frac{m\pi x_{n2}}{L})]}{\rho A L^2 \omega_m^2 \sqrt{(1 - \Omega^2 / \omega_m^2)^2 + [c_v \Omega / (\rho A \omega_m^2)]^2}} \sin(\frac{m\pi x}{L}) f_n(t) \quad (6.6)$$

where s is the total number of discrete electrodes and $f_n(t)$ is the time variation function of the electric potential applied to the n th electrode. From Eq.(6.6), it can be deduced that larger transverse displacement could be achieved by multiple electrodes. However, multiple electrodes imply complexity and difficulty in operation and control system.

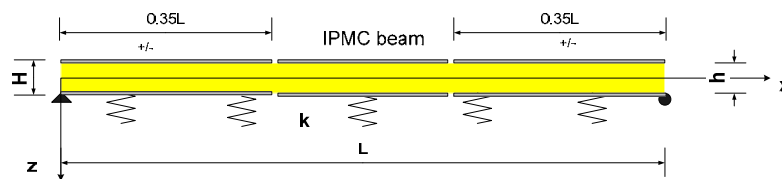


Figure 6.12 Configuration of two discrete electrodes

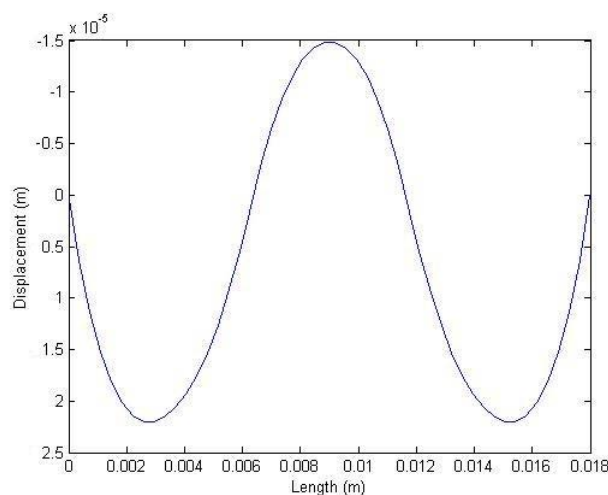


Figure 6.13 Deflection of beam with two electrodes under identical potentials

Chapter 6 Applications of Ionic Polymer-Metal Composites

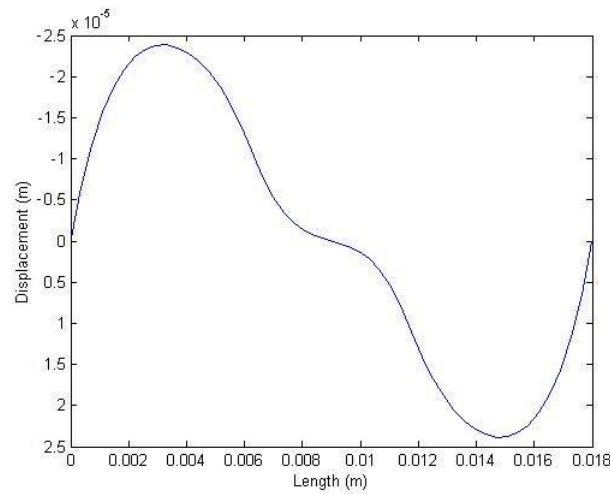


Figure 6.14 Deflection of beam with two electrodes under opposite potentials

A two-electrode IPMC beam is studied as illustrated in Fig.6.12. The two electrodes with the same length of $0.35L$ are located at the two ends of the beam. To avoid computational difficulty due to the change of beam stiffness, the region besides the electrodes is also considered to be plated with platinum but is isolated from electrodes by a negligible small interval. This can be achieved by chemical etching. The foundation stiffness is set as 15 kPa. Figs. 6.13 and 6.14 illustrate the deflections of beam under identical and opposite electric potentials, respectively. It is found that the opposite electric potential can produce larger transverse displacement. However, calculation shows that the generative pressure for Figs. 6.13 and 6.14 are 0.2935 gram and 0.1895 gram, respectively. This means that when the two electrodes are controlled by the identical potential, greater pressure will be generated on human tissue.

6.2.3 Concluding remarks

In this section, a dynamic IPMC beam model on human tissue was developed. An analytical solution was obtained to describe the vibration response of the IPMC beam to an electric potential. Based on the analytical solution, the beam deflection curve and the pressure distribution generated on human tissue were obtained. The

Chapter 6 Applications of Ionic Polymer-Metal Composites

optimal electrode location and length in terms of maximizing the deflection and generative pressure were discussed. It is found that to achieve the maximum deflection, the electrode should be located at either end of the beam, and to achieve higher total pressure, full length electrode should be used. The deflection curve and generative pressure for a multiple discrete electrode IPMC beam were also obtained. The developed model is useful not only for IPMC-related biomedical instruments interacting with human tissues but also for any other devices that utilize IPMC materials.

6.3 IPMC ring structure with elastic medium

Shahinpoor and Kim (2005) proposed using an IPMC ring structure to serve as a heart compression band and scleral band to apply supplementary pressure to human organs. In this section, an IPMC ring structure is studied. An analytical model is developed for the IPMC circular ring filled with elastic medium. The elastic medium is used to model human tissues or organs. A closed-form solution is obtained to depict the vibration response of the IPMC ring. Based on this solution, the characteristics of vibration are discussed. To increase the flexibility of the IPMC ring, a segmented IPMC ring is also considered.

6.3.1 Problem formulation

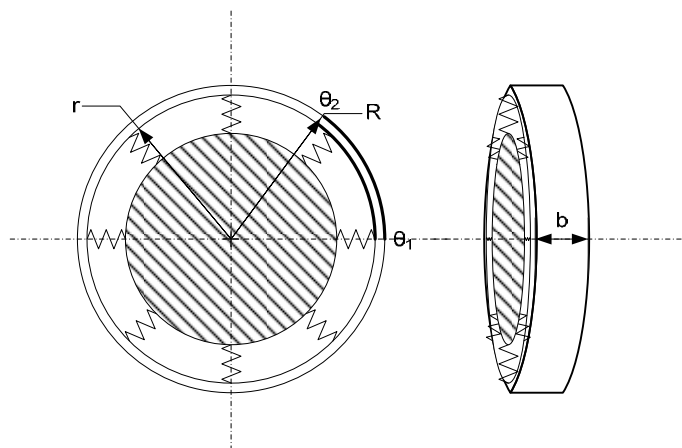


Figure 6.15 A circular IPMC ring filled with elastic medium

Chapter 6 Applications of Ionic Polymer-Metal Composites

Consider a thin IPMC circular ring with outer radius R , inner radius r and width b as shown in Fig.6.15. The electrode is located between θ_1 and θ_2 . The motion equation for a circular ring can be deduced from Love's shell theory as (Soedel, 2004),

$$\frac{1}{R} \frac{\partial(N_{\theta\theta} - N_{\theta\theta}^e)}{\partial\theta} + \frac{1}{R^2} \frac{\partial(M_{\theta\theta} - M_{\theta\theta}^e)}{\partial\theta} - \rho h \frac{\partial^2 u_\theta}{\partial t^2} = 0 \quad (6.7)$$

$$\frac{1}{R^2} \frac{\partial^2(M_{\theta\theta} - M_{\theta\theta}^e)}{\partial\theta^2} - \frac{N_{\theta\theta} - N_{\theta\theta}^e}{R} - kw - \rho h \frac{\partial^2 u_3}{\partial t^2} = 0 \quad (6.8)$$

where $N_{\theta\theta}$ and $N_{\theta\theta}^e$ are the membrane force resultants in the circumferential direction; $M_{\theta\theta}$ and $M_{\theta\theta}^e$ are the corresponding bending moments. The superscript e denotes the membrane force or bending moment due to the applied electric potential; ρ is the material density of the IPMC; $H = R - r$ is the thickness of the IPMC ring; u_θ and u_3 are the displacements in the circumferential and radial directions, respectively; k is the elastic foundation stiffness and t is time.

Transferring the terms due to the electric field to the right hand side, Eqs.(6.7) and (6.8) are converted to

$$\frac{1}{R} \frac{\partial N_{\theta\theta}}{\partial\theta} + \frac{1}{R^2} \frac{\partial M_{\theta\theta}}{\partial\theta} - \rho H \frac{\partial^2 u_\theta}{\partial t^2} = \frac{1}{R} \frac{\partial N_{\theta\theta}^e}{\partial\theta} + \frac{1}{R^2} \frac{\partial M_{\theta\theta}^e}{\partial\theta} \quad (6.9)$$

$$\frac{1}{R^2} \frac{\partial^2 M_{\theta\theta}}{\partial\theta^2} - \frac{N_{\theta\theta}}{R} - ku_3 - \rho H \frac{\partial^2 u_3}{\partial t^2} = \frac{1}{R^2} \frac{\partial^2 M_{\theta\theta}^e}{\partial\theta^2} - \frac{N_{\theta\theta}^e}{R} \quad (6.10)$$

The membrane forces and the corresponding bending moments in Eqs.(6.9) and (6.10) are defined by

$$N_{\theta\theta} = \int_{-H/2}^{H/2} \sigma_{\theta\theta} \cdot dz \quad (6.11)$$

Chapter 6 Applications of Ionic Polymer-Metal Composites

$$M_{\theta\theta} = \int_{-H/2}^{H/2} \sigma_{\theta\theta} \cdot z dz \quad (6.12)$$

where $\sigma_{\theta\theta}$ is the normal stress in the circumferential direction.

For a thin circular ring, the stress-strain relation under plain stress condition is

$$\sigma_{\theta\theta} = Y \cdot \varepsilon_{\theta\theta} \quad (6.13)$$

where Y and $\varepsilon_{\theta\theta}$ are the Young's modulus and the normal strain in the circumferential direction, respectively. The strain-displacement relation can be expressed as

$$\varepsilon_{\theta\theta} = \frac{1}{R} \left(\frac{\partial u_{\theta}}{\partial \theta} + u_3 \right) + \frac{z}{R^2} \left(\frac{\partial u_{\theta}}{\partial \theta} - \frac{\partial^2 u_3}{\partial \theta^2} \right) \quad (6.14)$$

Substituting Eqs.(6.13) and (6.14) into Eqs.(6.9)-(6.12), the motion equation can be written in a matrix form as

$$\begin{bmatrix} L_{11} & L_{12} \\ L_{21} & L_{22} \end{bmatrix} \cdot \begin{bmatrix} u_{\theta} \\ u_3 \end{bmatrix} = \begin{bmatrix} f_{\theta} \\ f_r \end{bmatrix} \quad (6.15)$$

where

$$L_{11} = \left(\frac{K}{R^2} + \frac{D}{R^4} \right) \frac{\partial^2}{\partial \theta^2} - \rho H \frac{\partial^2}{\partial t^2} \quad (6.16)$$

$$L_{12} = -\frac{D}{R^4} \frac{\partial^3}{\partial \theta^3} + \frac{K}{R^2} \frac{\partial}{\partial \theta} \quad (6.17)$$

$$L_{21} = \frac{D}{R^4} \frac{\partial^3}{\partial \theta^3} - \frac{K}{R^2} \frac{\partial}{\partial \theta} \quad (6.18)$$

Chapter 6 Applications of Ionic Polymer-Metal Composites

$$L_{22} = -\frac{D}{R^4} \frac{\partial^4}{\partial \theta^4} - \frac{K}{R^2} - \rho H \frac{\partial^2}{\partial t^2} - k \quad (6.19)$$

$$\begin{bmatrix} f_\theta \\ f_r \end{bmatrix} = \begin{bmatrix} \frac{1}{R} \frac{\partial N_{\theta\theta}^e}{\partial \theta} + \frac{1}{R^2} \frac{\partial M_{\theta\theta}^e}{\partial \theta} \\ \frac{1}{R^2} \frac{\partial^2 M_{\theta\theta}^e}{\partial \theta^2} - \frac{N_{\theta\theta}^e}{R} \end{bmatrix} \quad (6.20)$$

$$K = YHb, \quad D = Y \cdot H^3 b / 12 \quad (6.21)$$

The governing equation Eq.(6.15) can be solved by the method of modal expansion.

Since the IPMC ring vibrates in a pure bending mode when actuated, $N_{\theta\theta}^e = 0$ can be assumed. Considering that the bending moment of IPMC is uniform within the regions of electrodes, the moment distribution of IPMC ring can be expressed as

$$M_{\theta\theta}^e = M_0 [H(\theta - \theta_1) - H(\theta - \theta_2)] e^{j\Omega t} \quad (6.22)$$

where M_0 is the time independent part of Eq.(5.79), expressed as

$$M_0 = -\frac{Y_b b h L_A}{6(1 + w_0)} \left\{ \frac{f_A}{f_{A1}} [\exp(\frac{f_{A1}}{\Omega}) - 1] - \frac{\beta f_C}{f_{C1}} [\exp(\frac{f_{C1}}{\Omega}) - 1] \right\} \quad (6.23)$$

According to Eq.(6.20), the force vector is

$$\begin{bmatrix} f_\theta \\ f_r \end{bmatrix} = \begin{bmatrix} \frac{1}{R^2} M_0 [\delta(\theta - \theta_1) - \delta(\theta - \theta_2)] \\ \frac{1}{R^2} M_0 [\delta'(\theta - \theta_1) - \delta'(\theta - \theta_2)] \end{bmatrix} e^{j\Omega t} \quad (6.24)$$

Chapter 6 Applications of Ionic Polymer-Metal Composites

6.3.2 Displacement solutions

For a closed circular ring, the solution can be found in the form as

$$u_{\theta}(\theta, t) = \sum_{n=1}^{\infty} A_n \sin(n\theta + \varphi) e^{j\Omega t} \quad (6.25)$$

$$u_3(\theta, t) = \sum_{n=1}^{\infty} B_n \cos(n\theta + \varphi) e^{j\Omega t} \quad (6.26)$$

where φ is a phase angle.

When $\varphi = 0$, the natural modes of the ring can be expressed as

$$U_{\theta n1} = A_{n1} \sin(n\theta) e^{j\Omega t} \quad (6.27)$$

$$U_{3n1} = B_{n1} \cos(n\theta) e^{j\Omega t} \quad (6.28)$$

For a complete solution, another orthogonal mode should be taken into account.

When $\varphi = \pi / 2n$,

$$U_{\theta n2} = A_{n2} \cos(n\theta) e^{j\Omega t} \quad (6.29)$$

$$U_{3n2} = B_{n2} \sin(n\theta) e^{j\Omega t} \quad (6.30)$$

For $\varphi = 0$, the modal force vector is

$$\mathbf{F}_{n1} = \begin{bmatrix} -\frac{M_0}{R^2 \pi} [\sin(n\theta_2) - \sin(n\theta_1)] \\ \frac{nM_0}{R^2 \pi} [\sin(n\theta_2) - \sin(n\theta_1)] \end{bmatrix} e^{j\Omega t} \quad (6.31)$$

Chapter 6 Applications of Ionic Polymer-Metal Composites

The coefficients in Eqs.(6.27) and (6.28) can be obtained as

$$\begin{bmatrix} A_{n1} \\ B_{n1} \end{bmatrix} = \begin{bmatrix} \rho H \Omega^2 - s_{11} & s_{12} \\ s_{21} & \rho H \Omega^2 - s_{22} \end{bmatrix}^{-1} \begin{bmatrix} -\frac{M_0}{R^2 \pi} [\sin(n\theta_2) - \sin(n\theta_1)] \\ \frac{nM_0}{R^2 \pi} [\cos(n\theta_2) - \cos(n\theta_1)] \end{bmatrix} \quad (6.32)$$

where

$$s_{11} = \left(\frac{K}{R^2} + \frac{D}{R^4} \right) n^2 \quad (6.33)$$

$$s_{12} = s_{21} = -\frac{D}{R^4} n^3 - \frac{K}{R^2} n \quad (6.34)$$

$$s_{22} = \frac{D}{R^4} n^4 + \frac{K}{R^2} + k \quad (6.35)$$

Similarly, for $\varphi = \pi / 2n$, the coefficients in Eqs.(6.29) and (6.30) are

$$\begin{bmatrix} A_{n2} \\ B_{n2} \end{bmatrix} = \begin{bmatrix} \rho H \Omega^2 - s_{11} & -s_{12} \\ -s_{21} & \rho H \Omega^2 - s_{22} \end{bmatrix}^{-1} \begin{bmatrix} -\frac{M_0}{R^2 \pi} [\cos(n\theta_2) - \cos(n\theta_1)] \\ -\frac{nM_0}{R^2 \pi} [\sin(n\theta_2) - \sin(n\theta_1)] \end{bmatrix} \quad (6.36)$$

By using Eqs.(6.32) and (6.36), the final solution of the IPMC ring vibration can be expressed as

$$\begin{bmatrix} u_\theta(\theta, t) \\ u_3(\theta, t) \end{bmatrix} = \sum_{n=1}^{\infty} \begin{bmatrix} \sin(n\theta) & 0 \\ 0 & \cos(n\theta) \end{bmatrix} \begin{bmatrix} A_{n1} \\ B_{n1} \end{bmatrix} e^{j\Omega t} \quad (6.37)$$

Chapter 6 Applications of Ionic Polymer-Metal Composites

$$+ \sum_{n=1}^{\infty} \begin{bmatrix} \cos(n\theta) & 0 \\ 0 & \sin(n\theta) \end{bmatrix} \begin{bmatrix} A_{n2} \\ B_{n2} \end{bmatrix} e^{j\Omega t}$$

The corresponding total force generated on the elastic medium inside the ring can be calculated as

$$p_3(t) = \int_0^{2\pi} k \cdot u_3(\theta, t) \cdot H(u_3) d\theta \quad (6.38)$$

6.3.3 Illustrative example

To illustrate how the calculation procedure is carried out, assume a Nafion based IPMC ring in Na^+ form with mean radius of 50 mm and thickness of 0.224 mm. The IPMC ring consists of Nafion membrane and platinum electrodes. The thickness of Nafion membrane is 212 μm and the thickness of electrode is 6 μm on each surface. The applied electric potential is a 1.5-volt sinusoidal signal with frequency of 0.25 Hz. The thickness of anode boundary and cathode boundary calculated are $L_A = 9.78\ell$ and $L_C = 2.84\ell$, respectively, where $\ell = 0.862 \mu\text{m}$. Other model parameters are listed in Table 5.2.

Figs. 6.16-6.22 show the deformation of the IPMC ring for different electrode area with zero stiffness of elastic medium. As the elastic deformation of the IPMC ring is of interest, the rigid body motion due to the first vibration mode is not included in the calculation, i.e., the lower limit of the summation in Eq.(6.37) is $n = 2$. It is observed that the maximum deformation of the IPMC ring varies for different electrode areas. As shown in Figs.6.18 and 6.20, the IPMC ring has the largest deformation for the electrode area of $\pi/2$ and $3\pi/2$. In Fig.6.22, when the IPMC is fully plated with electrodes, the deformation is zero. This is true because the bending moment cancels each other at each point. By changing the area of electrode, larger deformation can be achieved. This conclusion is meaningful for reducing the cost of IPMC materials.

Chapter 6 Applications of Ionic Polymer-Metal Composites

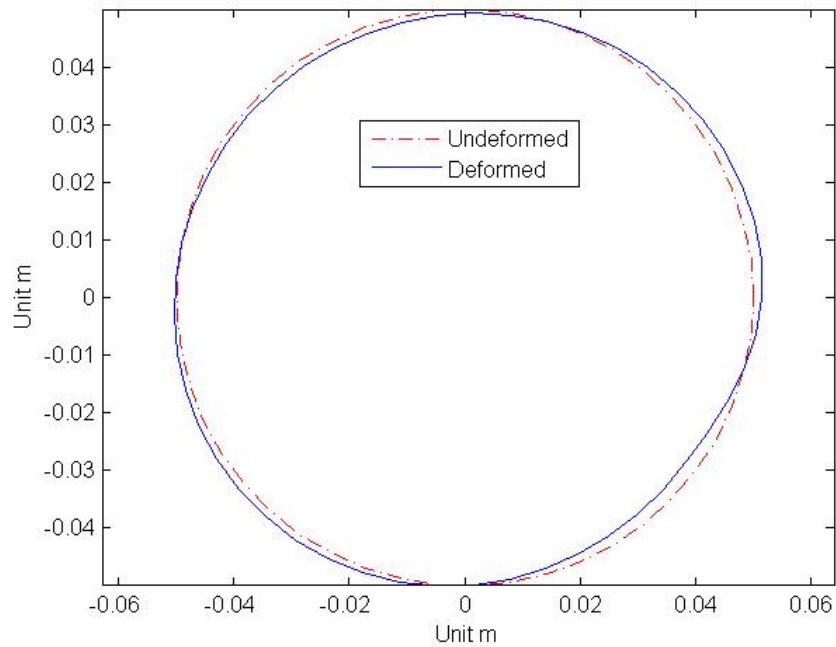


Figure 6.16 Deformation of IPMC ring with electrode area of $\pi/6$

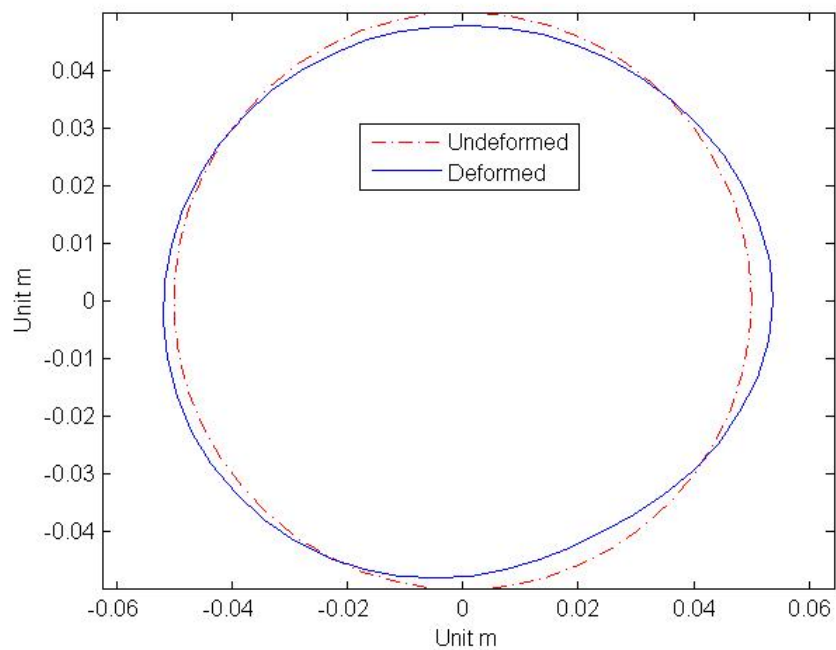


Figure 6.17 Deformation of IPMC ring with electrode area of $\pi/3$

Chapter 6 Applications of Ionic Polymer-Metal Composites

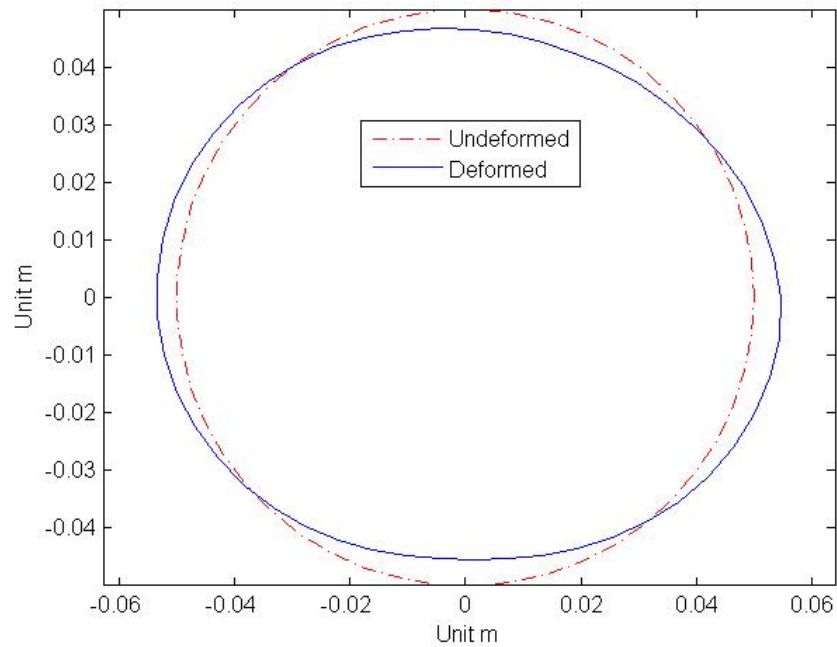


Figure 6.18 Deformation of IPMC ring with electrode area of $\pi/2$

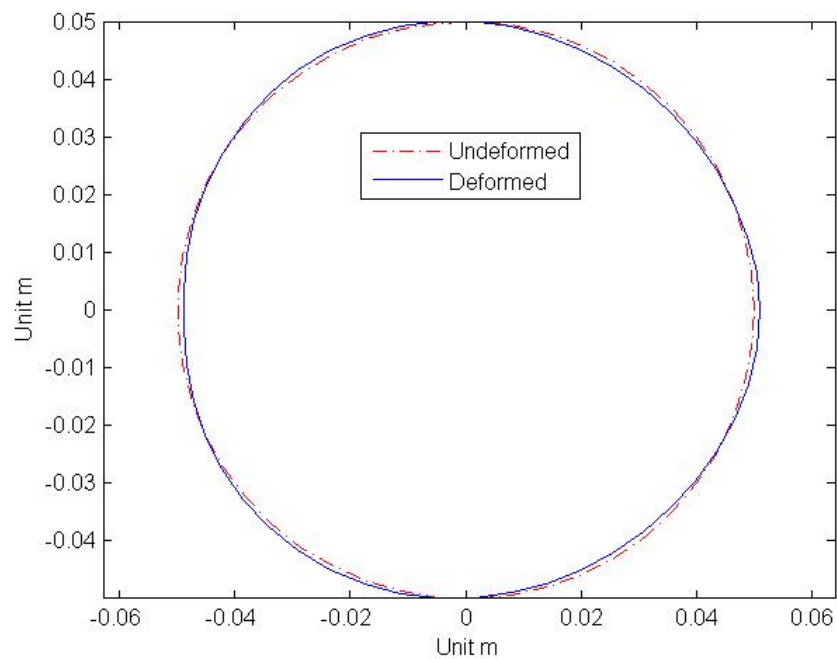


Figure 6.19 Deformation of IPMC ring with electrode area of π

Chapter 6 Applications of Ionic Polymer-Metal Composites

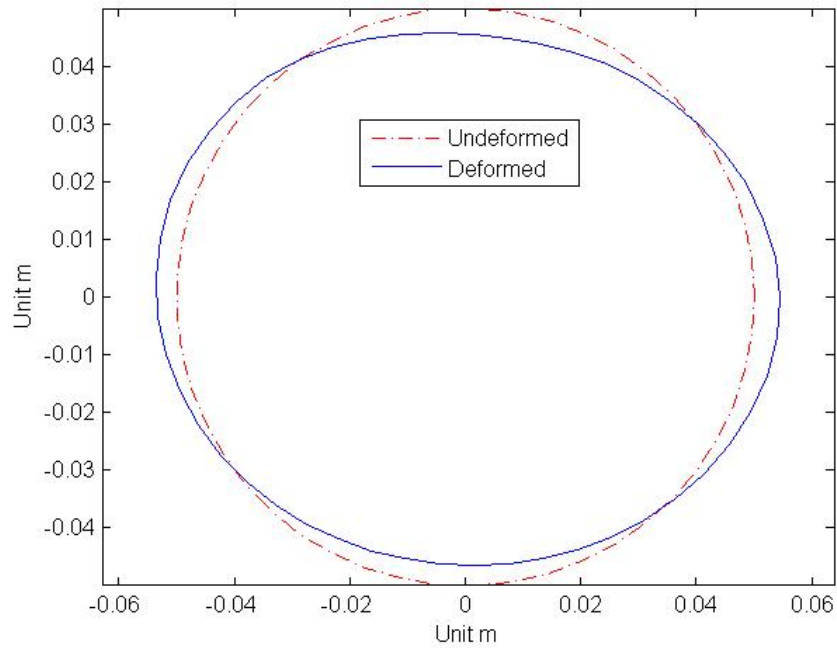


Figure 6.20 Deformation of IPMC ring with electrode area of $3\pi/2$

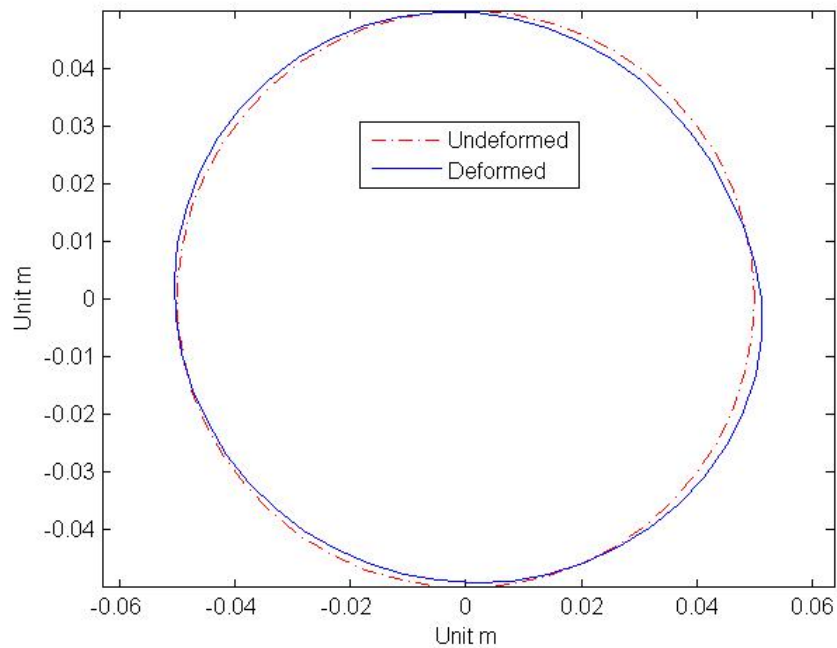


Figure 6.21 Deformation of IPMC ring with electrode area of 1.9π

Chapter 6 Applications of Ionic Polymer-Metal Composites

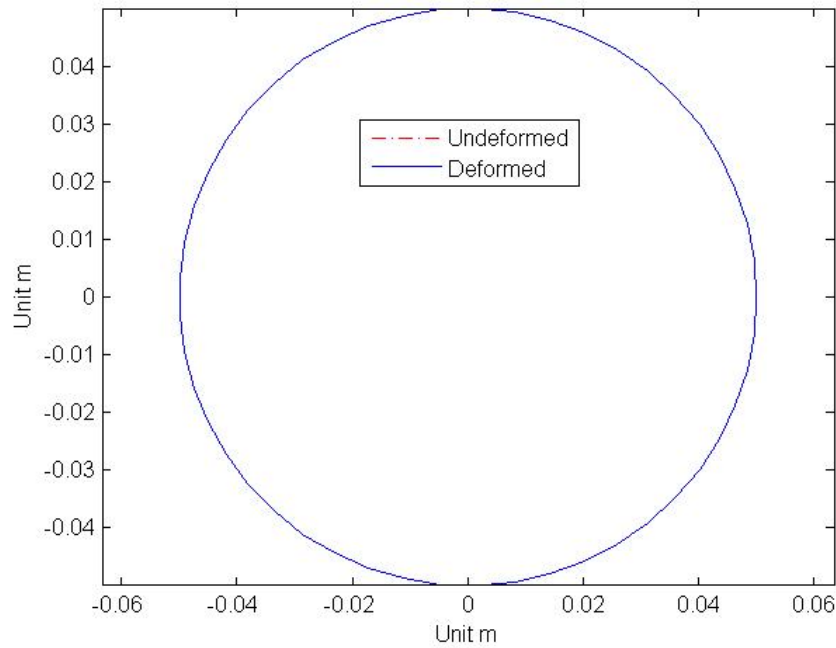


Figure 6.22 Deformation of IPMC ring with electrode area of 2π

Table 6.1 summarizes the largest deformation of the IPMC ring for different electrode areas. It is evident that the largest radial displacement occurs when electrode area is around $\pi/2$ and 1.5π . To further identify the electrode area corresponding to the largest radial deformation, a computer program is developed to find the relation between the electrode area and the maximum radial displacement. This computer program calculates the maximum radial displacement of the ring with different length of the electrode. A figure is obtained by plotting the maximum radial displacements vs the length of the electrode, as shown in Fig.6.23. It is observed that when the electrode area is around $\pi/2$ or $3\pi/2$, maximum radial displacement can be achieved.

Table 6.1 Maximum radial displacements for different electrode areas

Electrode area	$\pi/6$	$\pi/3$	$\pi/2$	π	1.5π	1.9π	2π
Maximum deformation (m)	0.0019	0.0037	0.0047	0.0011	0.0045	0.0019	0

Chapter 6 Applications of Ionic Polymer-Metal Composites

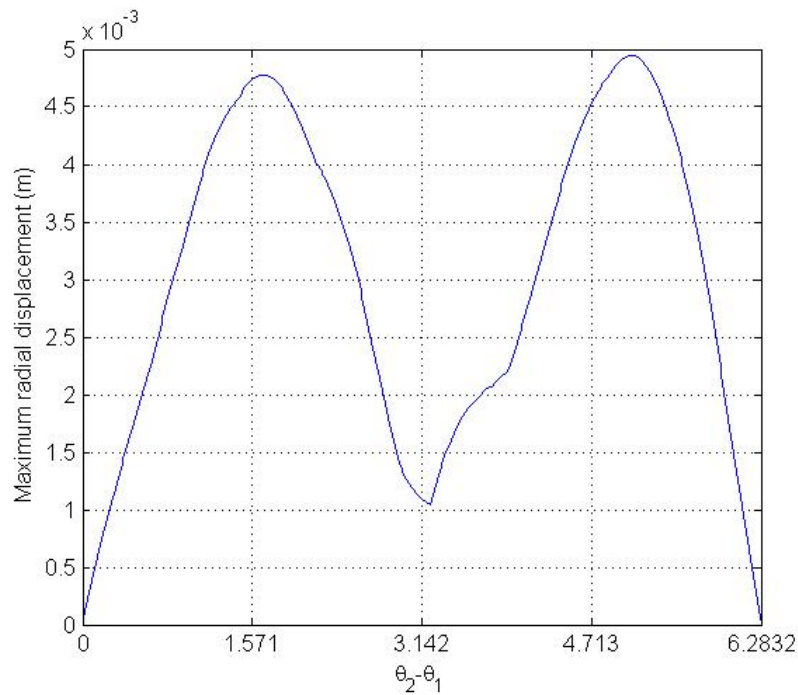


Figure 6.23 Electrode areas vs. maximum radial displacements

If the ring is assembled by two or more IPMC strips and electric potentials are applied independently to the electrodes, the vibration of the ring will vary a lot. The solution for this case can be obtained by the superposition of Eq.(6.37) for different coordinates of electrodes. Fig.6.24 illustrates an IPMC ring with segmented electrodes. Of the four segments, two opposite segments are set to be electrodes. Both electrode areas are $\pi/2$.

Chapter 6 Applications of Ionic Polymer-Metal Composites

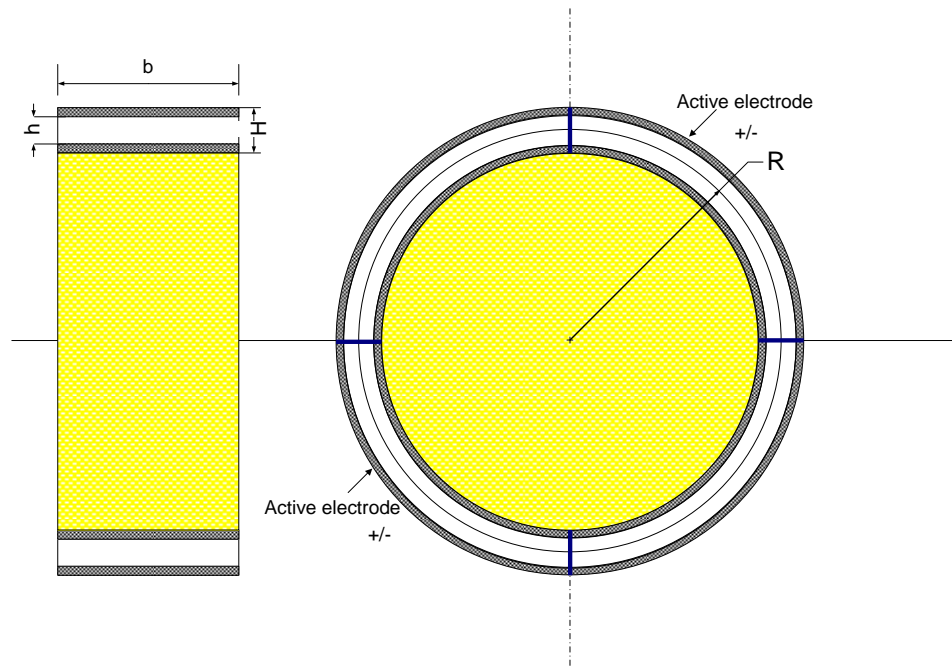


Figure 6.24 Configuration of two active electrode areas of IPMC ring

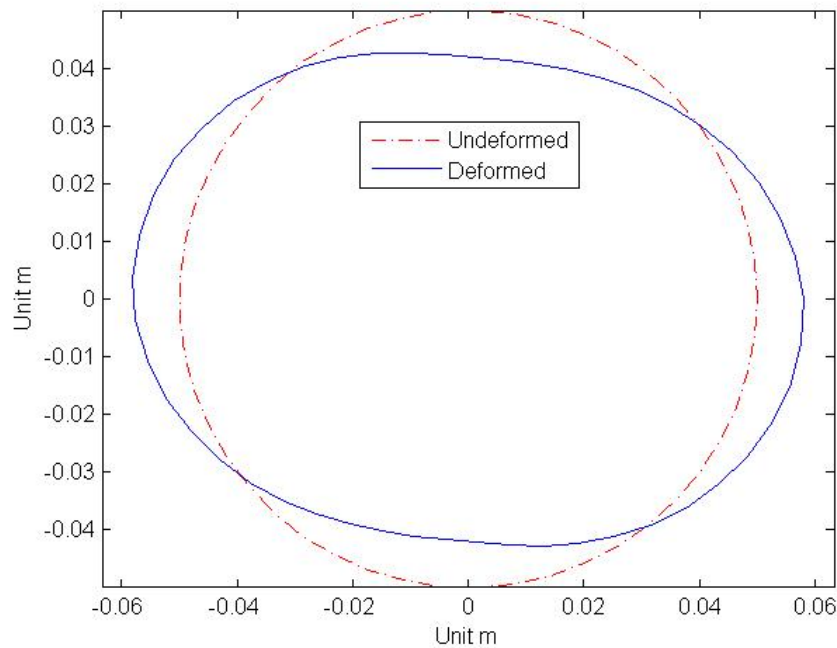


Figure 6.25 Deformation of IPMC ring with two electrodes

Fig.6.25 illustrates the IPMC ring deformation with two electrodes. Compared to the deformation of one electrode with area of $\pi/2$ as shown in Fig.6.18, the

Chapter 6 Applications of Ionic Polymer-Metal Composites

deformation is increased. The maximum radial displacement is 0.0082 m which is 1.74 times of the maximum radial displacement for single electrode.

The stiffness of the elastic medium in the above examples is set to be zero. When the stiffness is not zero, the displacements are small compared to the scale of the ring. The total pressure generated on the elastic medium by the ring can be evaluated by Eq.(6.38).

Assume that the stiffness of the elastic medium is 2.33 kPa, which is equivalent to the passive stiffness of myocyte of Guinea pig (Abe et al, 1996). As for non-zero stiffness, rigid body motion of ring no longer exists, the first vibration mode in Eq.(6.37) is included in the summation. For the configuration shown in Fig.6.24, the maximum displacement is 3×10^{-5} m, which is 0.37% of the maximum displacement with zero stiffness.

Fig.6.26 shows the relationship between the maximum radial displacement of the IPMC ring and the electrode area for six different elastic media. The stiffnesses of these elastic media are 0.3kPa, 0.5kPa, 1.0kPa, 1.5kPa, 2.33kPa and 3kPa. It is found that to achieve the largest displacement, the optimal electrode area is around 0.2-0.4 radian for the elastic media concerned. The higher the stiffness of the elastic medium, the smaller the active electrode area should be to achieve the largest displacement. Fig.6.27 illustrates the pressure distribution of the IPMC ring for the two electrodes as configured in Fig.6.24 for the six different media. The pressure distribution (in N/m) is the distribution of generated pressure (in Pa) along the circumference of the ring, which is obtained by integrating the generated pressure along the width of the ring. It is observed that with the increase of the stiffness of the elastic medium, the peak value of pressure also increases. For the elastic medium with stiffness of 2.33kPa, the peak value of pressure distribution is 0.0707

Chapter 6 Applications of Ionic Polymer-Metal Composites

N/m. By using Eq.(6.38), the overall force is calculated to be 0.0312 N, which is equivalent to 3.18 grams weight.

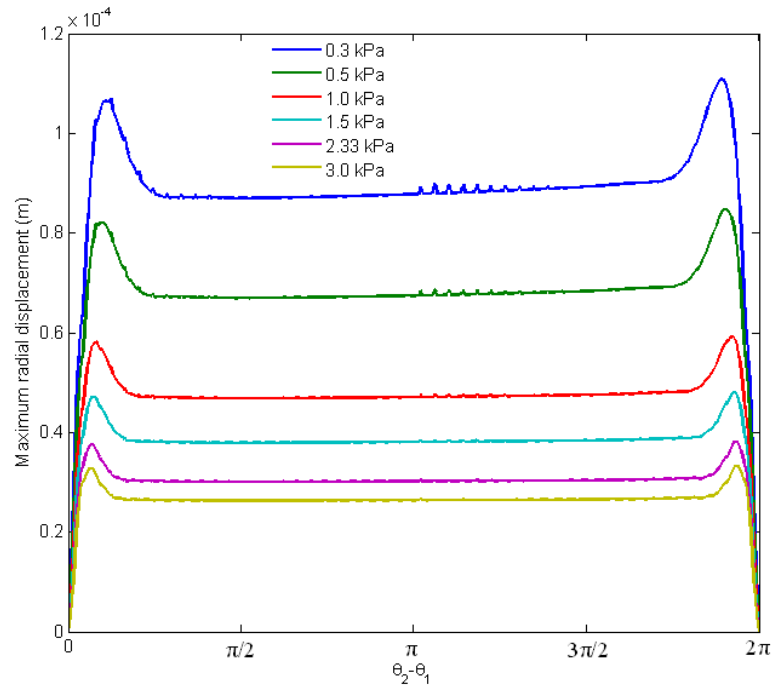


Figure 6.26 Electrode area vs. maximum radial displacement for different elastic media

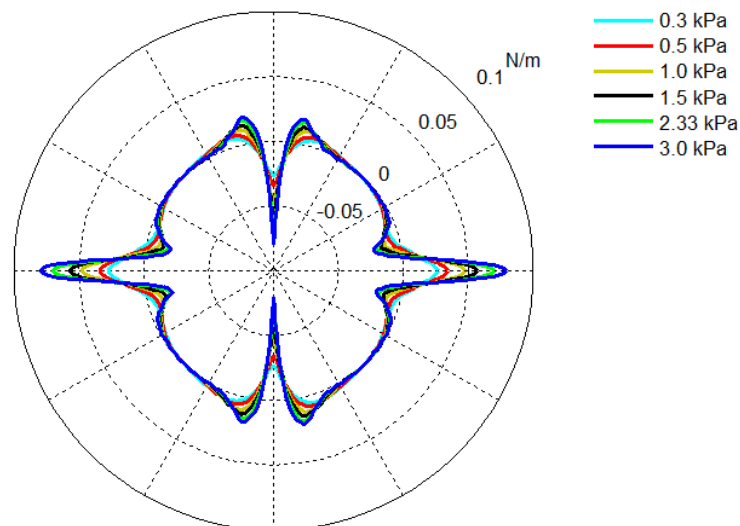


Figure 6.27 Pressure distribution of IPMC ring with two electrodes

Chapter 6 Applications of Ionic Polymer-Metal Composites

6.3.4 Concluding remarks

In this section, the vibration of an IPMC ring with elastic medium under harmonic electric signal has been studied. Based on the explicit bending moment expression of generative bending moment derived in Chapter 5, the analytical solution of IPMC ring vibration under electric potential has been obtained. The deformation of IPMC ring under different electrode areas and the pressure generated on elastic medium inside the ring were calculated. Multiple electrodes are also considered for the IPMC ring. Illustrative examples are presented. This model provides a general procedure for modeling the dynamic behavior of IPMC ring structure with elastic medium.

6.4 IPMC shell structure with flowing fluid

In some applications, the IPMC may be fabricated in the form of cylindrical shell. This kind of IPMC structure can be used as artificial vessels which are useful for biomedical practices. This section presents a study on an infinite IPMC cylindrical shell filled with steady-flow fluid. Vibrations of the shell-fluid coupled system occur when an electric potential is applied on the electrodes of IPMC. Analytical solutions are derived using the wave propagation method for the displacement of the cylindrical shell, the pressure in the liquid and the axial velocity of the liquid due to the electric potential excitation. The developed model may be useful for devices using IPMC cylindrical shell structures with or without contained liquids.

6.4.1 Problem formulation

6.4.1.1 Motion equation of cylindrical shell

Consider a segment of an infinite IPMC circular cylindrical shell with a discrete electrode as shown in Fig.6.28. The mean radius of the shell is R , the thickness of the shell wall is H and the thickness of the polyelectrolyte membrane part is h .

Chapter 6 Applications of Ionic Polymer-Metal Composites

The electrode of the shell covers the entire circumferential direction and locates between x_1 and x_2 in the axial direction.

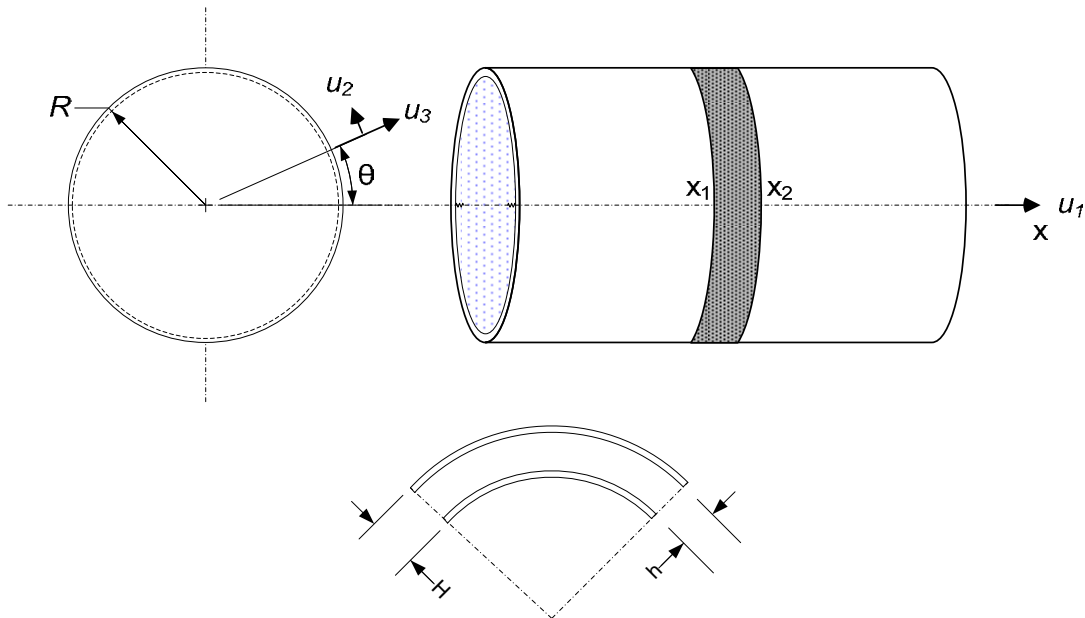


Figure 6.28 Configuration of IPMC circular cylindrical shell filled with fluid

Assume that the IPMC cylindrical shell is fully filled with an inviscid and incompressible fluid and an alternative electric potential is applied to the electrode on the IPMC shell. Due to the internal cation movement under electric field, the IPMC shell will vibrate at a frequency the same as that of the applied electric potential, resulting in the contained fluid being disturbed. According to the thin shell theory, the following equations can be derived (Soedel, 2004),

$$\frac{\partial(N_{xx} - N_{xx}^e)}{\partial x} + \frac{1}{R} \frac{\partial N_{\theta x}}{\partial \theta} - c_v \frac{\partial u_1}{\partial t} - \rho H \frac{\partial^2 u_1}{\partial t^2} = 0 \quad (6.39)$$

$$\begin{aligned} \frac{\partial N_{x\theta}}{\partial x} + \frac{1}{R} \frac{\partial(N_{\theta\theta} - N_{\theta\theta}^e)}{\partial \theta} + \frac{1}{R} \frac{\partial M_{x\theta}}{\partial x} + \frac{1}{R^2} \frac{\partial(M_{\theta\theta} - M_{\theta\theta}^e)}{\partial \theta} - c_v \frac{\partial u_2}{\partial t} \\ - \rho H \frac{\partial^2 u_2}{\partial t^2} = 0 \end{aligned} \quad (6.40)$$

Chapter 6 Applications of Ionic Polymer-Metal Composites

$$\begin{aligned} \frac{\partial^2(M_{xx} - M_{xx}^e)}{\partial x^2} + \frac{2}{R} \frac{\partial^2 M_{x\theta}}{\partial x \partial \theta} + \frac{1}{R^2} \frac{\partial^2(M_{\theta\theta} - M_{\theta\theta}^e)}{\partial \theta^2} - \frac{N_{\theta\theta} - N_{\theta\theta}^e}{R} - \\ c_v \frac{\partial u_3}{\partial t} - \rho H \frac{\partial^2 u_3}{\partial t^2} - p_p = 0 \end{aligned} \quad (6.41)$$

where N_{xx} , $N_{\theta x}$, $N_{x\theta}$, $N_{\theta\theta}$, M_{xx} , $M_{x\theta}$ and $M_{\theta\theta}$ are the membrane force resultants and bending moments in respective directions; the superscript e denotes the effect due to electric potential; c_v is the damping coefficient of the IPMC shell; ρ is the material density of the shell; u_1 , u_2 and u_3 are the displacements of middle surface of the shell in the axial, circumferential and radial directions, respectively; and p_p is the perturbation pressure of fluid on the inner shell surface, which will be determined in the next section.

Using the strain-stress and strain-displacement relationships of Flügge's shell theory (Soedel, 2004), the equation of motion can be obtained as

$$\begin{bmatrix} L_{11} & L_{12} & L_{13} \\ L_{21} & L_{22} & L_{23} \\ L_{31} & L_{32} & L_{33} \end{bmatrix} \begin{bmatrix} u_1 \\ u_2 \\ u_3 \end{bmatrix} = \gamma \begin{bmatrix} f_1 \\ f_2 \\ f_3 \end{bmatrix} \quad (6.42)$$

where L_{pq} ($p = 1, 2, 3$ and $q = 1, 2, 3$) are the differential operators defined as

$$\begin{aligned} L_{11} &= R^2 \frac{\partial^2}{\partial x^2} + (1+k) \frac{(1-\mu)}{2} \frac{\partial^2}{\partial \theta^2} - \frac{(1-\mu^2)R^2 c_v}{EH} \frac{\partial}{\partial t} - \frac{(1-\mu^2)\rho_s R^2}{E} \frac{\partial^2}{\partial t^2}, \\ L_{12} = L_{21} &= R \frac{1+\mu}{2} \frac{\partial^2}{\partial x \partial \theta}, \quad L_{13} = L_{31} = R\mu \frac{\partial}{\partial x} + k(-R^3 \frac{\partial^3}{\partial x^3} + R \frac{1-\mu}{2} \frac{\partial^3}{\partial x \partial \theta^2}), \\ L_{22} &= R^2 \frac{(1-\mu)}{2} \frac{\partial^2}{\partial x^2} + \frac{\partial^2}{\partial \theta^2} + kR^2 \frac{3(1-\mu)}{2} \frac{\partial^2}{\partial x^2} - \frac{(1-\mu^2)R^2 c_v}{EH} \frac{\partial}{\partial t} \\ &\quad - \frac{\rho_s(1-\mu^2)R^2}{E} \frac{\partial^2}{\partial t^2} \end{aligned} \quad (6.43)$$

Chapter 6 Applications of Ionic Polymer-Metal Composites

$$L_{23} = L_{32} = \frac{\partial}{\partial \theta} - kR^2 \frac{(3-\mu)}{2} \frac{\partial^3}{\partial x^2 \partial \theta},$$

$$L_{33} = 1 + k + k\nabla^4 + 2k \frac{\partial^2}{\partial \theta^2} - \frac{(1-\mu^2)R^2 c_v}{EH} \frac{\partial}{\partial t} - \frac{\rho_s(1-\mu^2)R^2}{E} \frac{\partial^2}{\partial t^2} - \frac{(1-\mu^2)R^2 p_p}{EH}$$

where $k = \frac{H^2}{12R^2}$ is a nondimensional thickness parameter; μ is the Poisson's ratio;

$\gamma = \frac{R^2(1-\mu^2)}{EH}$ and f_1 , f_2 and f_3 are the external loads in the axial,

circumferential and radial directions, respectively, which can be expressed as

$$f_1 = \frac{\partial N_{xx}^e}{\partial x} \quad (6.44)$$

$$f_2 = \frac{1}{R} \frac{\partial N_{\theta\theta}^e}{\partial \theta} + \frac{1}{R^2} \frac{\partial M_{\theta\theta}^e}{\partial \theta} \quad (6.45)$$

$$f_3 = \frac{\partial^2 M_{xx}^e}{\partial x^2} + \frac{1}{R^2} \frac{\partial^2 M_{\theta\theta}^e}{\partial \theta^2} - \frac{N_{\theta\theta}^e}{R} \quad (6.46)$$

6.4.1.2 Fluid perturbation

Consider the fluid contained in the infinite shell. Assume that the initial axial flow velocity is v_0 . When the IPMC shell vibrates due to the electric potential, the fluid inside the shell will be disturbed. The disturbed velocity field of the contained fluid is composed of two parts, the steady axial flow v_0 and the perturbation velocity due to the oscillation of the shell. Expressing the perturbation velocity as a function of perturbation potential Φ , the total velocity field can be written as

Chapter 6 Applications of Ionic Polymer-Metal Composites

$$\begin{bmatrix} v_1 \\ v_2 \\ v_3 \end{bmatrix} = \begin{bmatrix} v_0 + \frac{\partial \Phi}{\partial x} \\ \frac{1}{r} \frac{\partial \Phi}{\partial \theta} \\ \frac{\partial \Phi}{\partial r} \end{bmatrix} \quad (6.47)$$

The governing equation of the irrotational potential flow can be described by the Laplace equation (Paidoussis, 2004) as,

$$\frac{\partial^2 \Phi}{\partial r^2} + \frac{1}{r^2} \frac{\partial^2 \Phi}{\partial \theta^2} + \frac{\partial^2 \Phi}{\partial x^2} + \frac{1}{r} \frac{\partial \Phi}{\partial r} = 0 \quad (6.48)$$

The impermeability condition of the shell surface requires that the radial velocity of the fluid on the shell surface matches the instantaneous rate of change of the shell displacement in the radial direction. This boundary condition implies a permanent contact between the shell surface and the fluid boundary layer, which can be expressed as,

$$v_3|_{r=R} = \frac{\partial \Phi}{\partial r}|_{r=R} = \frac{\partial u_3}{\partial t} + v_0 \frac{\partial u_3}{\partial x} \quad (6.49)$$

The dynamic condition on the interface of the fluid and shell can be determined by the Bernoulli's equation for the disturbed motion as

$$\rho_f \frac{\partial \Phi}{\partial t} + \rho_f \frac{v_1^2 + v_2^2 + v_3^2}{2} + p_p = 0 \quad (6.50)$$

where ρ_f is the density of the contained liquid.

With Eqs.(6.47) and (6.50), the perturbation pressure on the fluid-shell interface can be obtained as

Chapter 6 Applications of Ionic Polymer-Metal Composites

$$p_p = -\rho_f \left(\frac{\partial \Phi}{\partial t} + v_0 \frac{\partial \Phi}{\partial x} \right) \quad (6.51)$$

It is noted that the higher order terms in Eq.(6.51) are neglected.

The velocity potential Φ can be expressed as

$$\Phi(r, x, \theta, t) = \Lambda(r) e^{j(\lambda x/R + n\theta + \Omega t)} \quad (6.52)$$

where $\Lambda(r)$ is a function to be determined; j is the imaginary unit; λ is a complex coefficient; n is the circumferential wave number; Ω is the angular frequency and t is time.

Substituting Eq.(6.52) into Eq.(6.48), the following equation can be obtained

$$\frac{d^2 \Lambda}{dr^2} + \frac{1}{r} \frac{d\Lambda}{dr} - \left(\frac{n^2}{r^2} + \frac{\lambda^2}{R^2} \right) \Lambda = 0 \quad (6.53)$$

Eq.(6.53) can be solved in terms of the modified Bessel functions of the first and second kind as

$$\Lambda(r) = D_1 I_n(\lambda r/R) + D_2 K_n(\lambda r/R) \quad (6.54)$$

where D_1 and D_2 are coefficients; and I_n and K_n are the n th order modified Bessel functions of the first and second kind, respectively. To arrive a finite solution, D_2 should be zero for the internal flow as $K_n(\lambda r/R)$ is singular at $r = 0$. Similarly, D_1 should be zero for the external flow as $I_n(\lambda r/R)$ approaches infinity when $r \rightarrow \infty$.

From Eqs.(6.51), (6.52) and (6.54), the perturbation pressure can be obtained as

Chapter 6 Applications of Ionic Polymer-Metal Composites

$$P_p = P_i - P_e \quad (6.55)$$

where p_i is the internal pressure on inner surface and p_e is the external pressure on outer surface.

$$P_i = -\rho_i \frac{R}{n + \lambda I_{n+1}(\lambda) / I_n(\lambda)} \left(\frac{\partial}{\partial t} + v_0 \frac{\partial}{\partial x} \right)^2 u_3 \quad (6.56)$$

$$P_e = -\rho_e \frac{R}{n - \lambda K_{n+1}(\lambda) / K_n(\lambda)} \left(\frac{\partial}{\partial t} + v_0 \frac{\partial}{\partial x} \right)^2 u_3 \quad (6.57)$$

where ρ_i and ρ_e are the density of internal and external flow, respectively.

As IPMC shell is in the pure bending deformation under the electric potential, assumptions can be made that $N_{xx}^e = N_{\theta\theta}^e = 0$, and the bending moments in the two orthogonal direction are identical, i.e., $M_{xx}^e = M_{\theta\theta}^e$, due to the homogeneous nature of IPMC. Consider that the bending moments are developed uniformly within the region of electrode,

$$M_{xx}^e = M_0 \cdot [H(x - x_1) - H(x - x_2)][H(\theta - 0) - H(\theta - 2\pi)]e^{j(\Omega t - \pi/2)} \quad (6.58)$$

$$M_{\theta\theta}^e = M_0 \cdot [H(\theta - 0) - H(\theta - 2\pi)][H(x - x_1) - H(x - x_2)]e^{j(\Omega t - \pi/2)} \quad (6.59)$$

where M_0 is the time-independent part of Eq.(5.79).

With the discussions of previous sections, the force vector in Eq.(6.42) is finally determined as

Chapter 6 Applications of Ionic Polymer-Metal Composites

$$\begin{bmatrix} f_1 \\ f_2 \\ f_3 \end{bmatrix} = \begin{bmatrix} 0 \\ 0 \\ M_0 [\delta'(x-x_1) - \delta'(x-x_2)] \end{bmatrix} \quad (6.60)$$

where $\delta'(\cdot)$ is the derivative of Dirac-delta function with respect to x .

6.4.2 Wave propagation solutions

The solution of displacement field to Eq.(6.42) can be written in the form of traveling wave as

$$\begin{bmatrix} u_1 \\ u_2 \\ u_3 \end{bmatrix} = \begin{bmatrix} A \\ B \\ C \end{bmatrix} e^{j(\lambda x/R + n\theta + \Omega t)} \quad (6.61)$$

where A , B and C are complex coefficients.

Substituting Eq.(6.61) into Eq.(6.42) and equating the left-hand side to zero, a linear homogeneous equation can be obtained for free vibration as

$$\begin{bmatrix} a_{11} & a_{12} & a_{13} \\ a_{21} & a_{22} & a_{23} \\ a_{31} & a_{32} & a_{33} \end{bmatrix} \cdot \begin{bmatrix} A \\ B \\ C \end{bmatrix} = \begin{bmatrix} 0 \\ 0 \\ 0 \end{bmatrix} \quad (6.62)$$

where $a_{11} = \lambda^2 + \frac{1-\mu}{2}n^2(1+k) + j(\bar{c}_v\bar{\Omega}) - \bar{\Omega}^2$, $a_{12} = a_{21} = \frac{1+\mu}{2}\lambda n$,

$a_{13} = -ja_{31} = -j\lambda[\mu + k(\lambda^2 - \frac{1-\mu}{2}n^2)]$, $a_{22} = n^2 + \frac{1-\mu}{2}\lambda^2(1+3k) + j(\bar{c}_v\bar{\Omega}) - \bar{\Omega}^2$,

$a_{23} = -ja_{32} = -j(n + \frac{3-\mu}{2}\lambda^2nk)$

Chapter 6 Applications of Ionic Polymer-Metal Composites

$$a_{33} = -j\{1 + k[(\lambda^2 + n^2)^2 - 2n^2 + 1] + j(\bar{c}_v \bar{\Omega}) - \bar{\Omega}^2$$

$$- \frac{(R/h)(\rho_i/\rho_f)(\bar{\Omega} + \bar{U}_i \lambda)^2}{n + \lambda I_{n+1}(\lambda)/I_n(\lambda)} + \frac{(R/h)(\rho_e/\rho_f)(\bar{\Omega} + \bar{U}_e \lambda)^2}{n + \lambda K_{n+1}(\lambda)/K_n(\lambda)}\}, \quad \bar{\Omega} = R\Omega \left[\frac{\rho(1-\mu^2)}{E} \right]^{1/2},$$

$$\bar{U}_i = v_0 \left[\frac{\rho(1-\mu^2)}{E} \right]^{1/2}, \quad \bar{U}_e = 0 \text{ and } \bar{c}_v = c_v R \left[\frac{\rho(1-\mu^2)}{E} \right]^{1/2}.$$

For non-trivial solution, the determinant of the coefficient matrix in Eq.(6.62) should be zero, i.e.,

$$\det \begin{bmatrix} a_{11} & a_{12} & a_{13} \\ a_{21} & a_{22} & a_{23} \\ a_{31} & a_{32} & a_{33} \end{bmatrix} = 0 \quad (6.63)$$

Through Eq.(6.63), the coefficient λ can be obtained for a given circumferential wave number n . Due to the transcendental nature of λ , there are infinite roots of λ for Eq.(6.63). Therefore, the complete solution of displacement field can be expressed as

$$\begin{bmatrix} u_1 \\ u_2 \\ u_3 \end{bmatrix} = \sum_{i=1}^{\infty} \begin{bmatrix} \alpha_i C_i \\ \gamma_i C_i \\ C_i \end{bmatrix} e^{j(\lambda_i x/R + n\theta + \Omega t)} \quad (6.64)$$

where the coefficients α_i and γ_i can be determined from Eq.(6.62) with the eigenvalue λ_i . However, since the available boundary conditions are generally not infinite, it is impossible to include infinite λ_i in Eq.(6.64). Moreover the values of λ_i that contribute most to the modal shapes are those with small modulus. Thus, it is possible to use truncated set of λ_i , say four or eight, to represent the displacement field with acceptable accuracy. In this section, only eight λ_i are used for the calculation.

Chapter 6 Applications of Ionic Polymer-Metal Composites

The values of C_i can be determined through the boundary conditions. There are four internal forces in the shell wall in the axial direction, which are the axial force N_{xx} , the bending moment M_{xx} , the transverse shear force S_{xx} and the torsional shear force T_{xx} , expressed as

$$N_{xx} = R \frac{\partial u_1}{\partial x} + \mu \frac{\partial u_2}{\partial \theta} + \mu u_3 - \frac{H^2}{12} \frac{\partial^2 u_3}{\partial x^2} \quad (6.65)$$

$$M_{xx} = R^2 \frac{\partial^2 u_3}{\partial x^2} + \mu \frac{\partial^2 u_3}{\partial \theta^2} - \mu \frac{\partial u_2}{\partial \theta} - R \frac{\partial u_1}{\partial x} \quad (6.66)$$

$$S_{xx} = R^3 \frac{\partial^3 u_3}{\partial x^3} + (2 - \mu) R \frac{\partial^3 u_3}{\partial x \partial \theta^2} - \frac{3 - \mu}{2} R \frac{\partial^2 u_2}{\partial x \partial \theta} + \frac{1 - \mu}{2} \frac{\partial^2 u_1}{\partial \theta^2} - R^2 \frac{\partial^2 u_1}{\partial x^2} \quad (6.67)$$

$$T_{xx} = \frac{\partial u_1}{\partial \theta} + R \frac{\partial u_2}{\partial x} + \frac{H^2}{4R} \left(\frac{\partial u_2}{\partial x} - \frac{\partial^2 u_3}{\partial x \partial \theta} \right) \quad (6.68)$$

At x_1 and x_2 , the following boundary conditions apply

$$N_{xx}(x = x_1, x_2) = 0 \quad (6.69)$$

$$M_{xx}(x = x_1, x_2) = -M_0 \quad (6.70)$$

$$S_{xx}(x = x_1, x_2) = 0 \quad (6.71)$$

$$T_{xx}(x = x_1, x_2) = 0 \quad (6.72)$$

Substituting Eq.(6.64) into Eqs.(6.69)-(6.72) and utilizing Eqs.(6.65)-(6.68), the following equation is obtained,

Chapter 6 Applications of Ionic Polymer-Metal Composites

$$\begin{bmatrix} b_{11} & b_{12} & b_{13} & b_{14} & 0 & 0 & 0 & 0 \\ b_{21} & b_{22} & b_{23} & b_{24} & 0 & 0 & 0 & 0 \\ b_{31} & b_{32} & b_{33} & b_{34} & 0 & 0 & 0 & 0 \\ b_{41} & b_{42} & b_{43} & b_{44} & 0 & 0 & 0 & 0 \\ 0 & 0 & 0 & 0 & b_{55} & b_{56} & b_{57} & b_{58} \\ 0 & 0 & 0 & 0 & b_{65} & b_{66} & b_{67} & b_{68} \\ 0 & 0 & 0 & 0 & b_{75} & b_{76} & b_{77} & b_{78} \\ 0 & 0 & 0 & 0 & b_{85} & b_{86} & b_{87} & b_{88} \end{bmatrix} \cdot \begin{bmatrix} C_1 \\ C_2 \\ C_3 \\ C_4 \\ C_5 \\ C_6 \\ C_7 \\ C_8 \end{bmatrix} = \begin{bmatrix} 0 \\ -M_0 \\ 0 \\ 0 \\ 0 \\ -M_0 \\ 0 \\ 0 \end{bmatrix} \quad (6.73)$$

where

$$b_{1s} = (j\alpha_s \lambda_s + j\mu\gamma_s n + \mu + k\lambda_s^2) e^{j(\lambda_s x_1 / R + n\theta)}$$

$$b_{2s} = (-\lambda_s^2 - \mu n^2 - j\mu\gamma_s n - j\alpha_s \lambda_s) e^{j(\lambda_s x_1 / R + n\theta)},$$

$$b_{3s} = [-j\lambda_s^3 - j(2 - \mu)\lambda_s n^2 + (3 - \mu)\gamma_s \lambda_s n / 2 - (1 - \mu)\alpha_s n^2 / 2 + \alpha_s \lambda_s^2] e^{j(\lambda_s x_1 / R + n\theta)}$$

$$b_{4s} = [j\alpha_s n + j\gamma_s \lambda_s n^2 + 3k(j\gamma_s \lambda_s + \lambda_s n)] e^{j(\lambda_s x_1 / R + n\theta)}, \quad s = 1, 2, 3, 4;$$

and

$$b_{5m} = (j\alpha_m \lambda_m + j\mu\gamma_m n + \mu + k\lambda_m^2) e^{[j(\lambda_m x_2 / R + n\theta)]},$$

$$b_{6m} = (-\lambda_m^2 - \mu n^2 - j\mu\gamma_m n - j\alpha_m \lambda_m) e^{j(\lambda_m x_2 / R + n\theta)},$$

$$b_{7m} = [-j\lambda_m^3 - j(2 - \mu)\lambda_m n^2 + (3 - \mu)\gamma_m \lambda_m n / 2 - (1 - \mu)\alpha_m n^2 / 2 + \alpha_m \lambda_m^2] e^{j(\lambda_m x_2 / R + n\theta)}$$

$$b_{8m} = [j\alpha_m n + j\gamma_m \lambda_m n^2 + 3k(j\gamma_m \lambda_m + \lambda_m n)] e^{j(\lambda_m x_2 / R + n\theta)}, \quad m = 5, 6, 7, 8.$$

The coefficient C_i , $i = 1, 2, \dots, 8$, can be easily solved from Eq.(6.73) as

$$\begin{bmatrix} C_1 \\ C_2 \\ C_3 \\ C_4 \\ C_5 \\ C_6 \\ C_7 \\ C_8 \end{bmatrix} = \begin{bmatrix} b_{11} & b_{12} & b_{13} & b_{14} & 0 & 0 & 0 & 0 \\ b_{21} & b_{22} & b_{23} & b_{24} & 0 & 0 & 0 & 0 \\ b_{31} & b_{32} & b_{33} & b_{34} & 0 & 0 & 0 & 0 \\ b_{41} & b_{42} & b_{43} & b_{44} & 0 & 0 & 0 & 0 \\ 0 & 0 & 0 & 0 & b_{55} & b_{56} & b_{57} & b_{58} \\ 0 & 0 & 0 & 0 & b_{65} & b_{66} & b_{67} & b_{68} \\ 0 & 0 & 0 & 0 & b_{75} & b_{76} & b_{77} & b_{78} \\ 0 & 0 & 0 & 0 & b_{85} & b_{86} & b_{87} & b_{88} \end{bmatrix}^{-1} \begin{bmatrix} 0 \\ -M_0^e \\ 0 \\ 0 \\ 0 \\ -M_0^e \\ 0 \\ 0 \end{bmatrix} \quad (6.74)$$

Therefore, for eight eigenvalues of λ , the displacement field is

Chapter 6 Applications of Ionic Polymer-Metal Composites

$$\begin{bmatrix} u_1 \\ u_2 \\ u_3 \end{bmatrix} = \sum_{i=1}^8 \begin{bmatrix} \alpha_i C_i \\ \gamma_i C_i \\ C_i \end{bmatrix} e^{j(\lambda_i x / R + n\theta + \Omega t)} \quad (6.75)$$

The corresponding velocity field of the contained fluid can be obtained from Eqs.(6.75), (6.52) and (6.49) as

$$\begin{bmatrix} v_1 \\ v_2 \\ v_3 \end{bmatrix} = \begin{bmatrix} \sum_{i=1}^8 -\frac{C_i \lambda_i (\Omega R + \lambda_i v_0) I_n(\lambda_i r / R)}{R(nI_n(\lambda_i) + \lambda_i I_{n+1}(\lambda_i))} e^{j(\lambda_i x / R + n\theta + \Omega t)} + v_0 \\ \sum_{i=1}^8 -\frac{C_i n (\Omega R + \lambda_i v_0) I_n(\lambda_i r / R)}{r(nI_n(\lambda_i) + \lambda_i I_{n+1}(\lambda_i))} e^{j(\lambda_i x / R + n\theta + \Omega t)} \\ \sum_{i=1}^8 -\frac{j C_i (\Omega R + \lambda_i v_0) (\lambda_i I_{n+1}(\lambda_i r / R) + n R I_n(\lambda_i r / R) / r)}{R(nI_n(\lambda_i) + \lambda_i I_{n+1}(\lambda_i))} e^{j(\lambda_i x / R + n\theta + \Omega t)} \end{bmatrix} \quad (6.76)$$

6.4.3 Illustrative example and discussion

To illustrate how the calculation procedure is carried out, assume a Nafion based IPMC circular cylindrical shell in Na^+ form with mean radius of 15 mm, and thickness of 224 μm . The IPMC cylindrical shell is composed of Nafion membrane and platinum electrode. The thickness of Nafion membrane is 212 μm and the thickness of electrode is 6 μm on each surface. The contained fluid is water with density of 10^3 kg/m^3 , and the initial axial velocity is assumed to be 0.9 m/s. The applied electric potential is a 1.5-volt sinusoidal signal with frequency 0.25 Hz. The coordinates of electrode are $x_1 = -0.005 \text{ m}$ and $x_2 = 0.005 \text{ m}$. The thickness of anode boundary and cathode boundary calculated are $L_A = 9.78\ell$ and $L_C = 2.84\ell$, respectively, where $\ell = 0.862 \mu\text{m}$. The damping coefficient c_v is set to be zero to ease the computation. Other model parameters are listed in Table 5.2.

Fig.6.29 shows the deformation of the IPMC shell when the electric potential is at its maximum. The radial deformation of the shell is amplified 10 times for clear

Chapter 6 Applications of Ionic Polymer-Metal Composites

illustration. It is observed that the waves are propagating symmetrically away from the electrode. The maximum axial velocity for this case is 0.9195 m/s, which is 2.17 % larger than the initial flow. For v_2 and v_3 , the maximum velocities are 0.0592m/s and 0.0055 m/s, respectively. It is evident that the velocity components v_2 and v_3 are negligible for this case. The maximum shell deformation is about 0.4 mm.

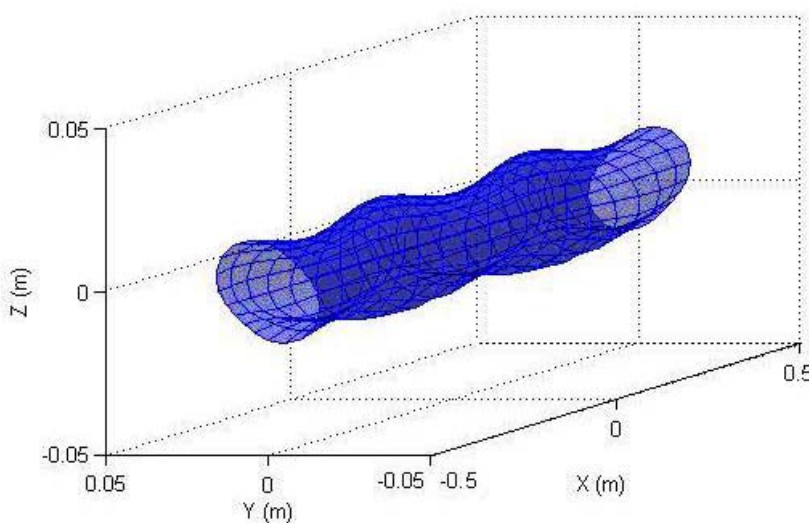


Figure 6.29 Amplified shell deformation at electric signal of 1.5 V/0.25 Hz (10 times)

Chapter 6 Applications of Ionic Polymer-Metal Composites

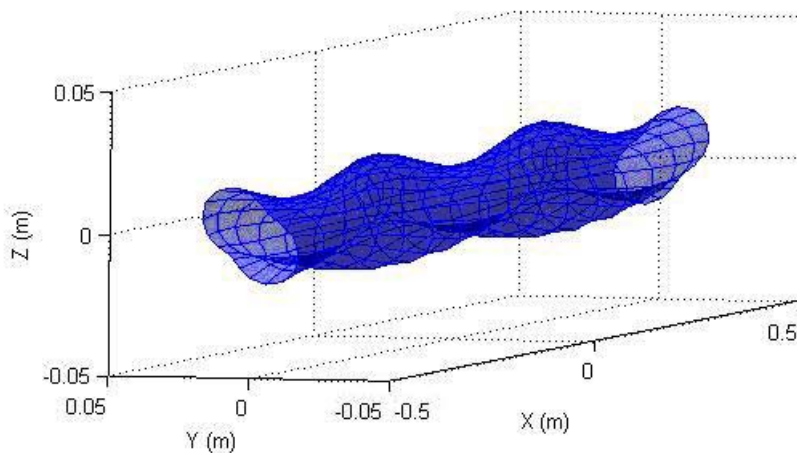


Figure 6.30 Shell deformation at electric signal of 3 V/0.25 Hz

Compared to the initial axial velocity, the change in axial velocity is quite small for the 1.5-volt electric potential. However, the axial velocity can be increased by applying larger electric potential. For a 3-volt signal, the maximum axial velocity is calculated to be 1.236 m/s, which is about 37.3% increment of the initial flow. The increment of axial flow is distinct compared to that under the 1.5-volt signal. Fig.6.30 shows the shell deformation in this condition without amplification. The Maximum deformation of the shell is around 4.992 mm. It is worth mentioning that under such large deformation, Eq.(6.42) may not be valid. In addition, the IPMC material has become unstable under such high voltage. However, this example does provide approximate order of magnitude of the shell deformation and the maximum increment of axial flow, which is meanful for future study.

Due to the limitation of solvent electrolysis, the applied electric potential generally can not be too high for IPMCs, e.g., 3 volts (electrolysis begins beyond 1.23 volt) for water as solvent. Alternatively, the axial velocity can be increased by utilizing multiple electrodes as shown in Fig.6.31. By individually exciting different electrodes, it is possible to generate a wave that could significantly amplify the axial velocity of flow. The solutions for multiple electrodes can be obtained by the superposition of the results of single electrode obtained in this section. For other

Chapter 6 Applications of Ionic Polymer-Metal Composites

special cases, the developed model can be easily reduced to the solutions of IPMC shell with quiescent fluid or without fluid.

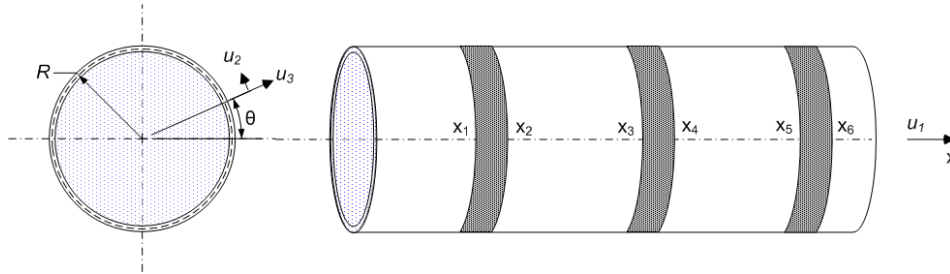


Figure 6.31 Cylindrical shell with multiple electrodes

6.4.4 Concluding remarks

In this section, a dynamic model of a fluid-filled IPMC shell was developed. The vibration response of the shell and the velocity field of the contained fluid under the applied electric potential were obtained by the wave propagation method. An illustrative example was presented. It was found that the flow velocity could be enhanced by the application of electric potential on the IPMC shell. It is also possible to further increase the axial flow by multiple electrodes and the solutions obtained in this section can be extended to multiple electrode analysis. This model could be important for further modeling of IPMC based artificial vessels.

6.5 Conclusions

In this chapter, three different models of IPMC based structures, i.e., an IPMC beam on human tissues, an IPMC ring with elastic medium and a fluid-filled IPMC cylindrical shell, were developed for possible biomedical applications. Analytical solutions were derived to account for the effect of IPMC actuation. The characteristics of the structural response under IPMC actuation were presented and discussed. Calculation examples were given for illustration. By examining the modeling results, it can be seen that the bending capacity of the IPMC materials

Chapter 6 Applications of Ionic Polymer-Metal Composites

is not sufficient to be used practically. The force generation capacity of the IPMC materials needs to be improved by nano or chemical fabrication methods. Another alternative is to replace the IPMC materials with other stronger EAPs to generate sufficient force or bending moment for practical use. The results obtained in this chapter provide guidelines for further modeling and experimental tests of these models.

Chapter 7 Conclusions and Recommendations

7.1 Summary and conclusions

Piezoelectric material and ionic polymer-metal composite are two kinds of popular smart materials. Although their actuation mechanisms are completely different, their responses to electric stimuli are quite similar. This thesis focuses on the actuation characteristics of the two materials. The relation between the actuation characteristics of the two types of smart materials and their output effects, i.e., vibration and displacement, generative pressure and force, and changes of velocity field of contained flowing fluid has been derived.

Piezoelectric material is a well studied material and has been used for many applications. In this thesis, piezoelectric actuated plate and shell structures have been studied. Analytical solutions have been obtained to associate the input electric signal with the structural response. The problem of optimal placement of piezoelectric actuator on plate and shell in terms of maximizing excitation has been investigated based on the solutions obtained. A simple yet general procedure has been proposed to find the optimal locations of the piezoelectric actuator.

For the IPMC material, the dynamic behaviors of IPMCs have been studied. Explicit bending moment expressions have been obtained to account for the bending capacity of IPMC under both the static and dynamic electric potentials. The bending moment expressions have been used to model IPMC based prototypes for possible biomedical applications. Three prototype models, i.e., an IPMC beam on human tissues, an IPMC ring with elastic medium and an IPMC cylindrical shell with flow fluid, have been developed. Solutions have been obtained to account for the effects of IPMC actuation. The results provide guidelines for future experimental tests and practical applications.

Chapter 7 Conclusions and Recommendations

The main research work carried out so far and the conclusions obtained can be summarized as follows,

- 1) Dynamic models of piezoelectric material actuated plate and shell structures have been developed. These models built up the relationships between the structural response and the input electric signals on the piezoelectric material. In-plane vibration of plate due to piezoelectric material actuation has been evaluated by finite difference method. The effect of in-plane vibration has been proved to be negligible compared to the transverse vibration.
- 2) Optimal placement of the piezoelectric actuator on plates and shells in terms of optimal excitation has been studied. By using the combined position mode functions (CPMFs), a simple and general procedure is proposed to find the optimal locations of the piezoelectric actuator on plates and shells. This procedure only requires the calculation of natural frequency of structures and therefore easy to implement.
- 3) The dynamic behaviors of IPMC have been studied. Bending moment expressions have been derived from Nemat-Nasser's hybrid actuation model. The bending moment expressions provide an easy estimation of the bending capacity of IPMC at certain hydration rate and given counter ion type, thus making them easy to be used in modeling of IPMC based devices.
- 4) Three prototypes of IPMC for biomedical applications are proposed, i.e., a beam structure for minimum invasive surgery, a ring structure for heart compression band and a fluid-filled cylindrical shell for artificial veins. Analytical solutions have been obtained to associate the actuation capacity of IPMC and the structure response. The output effects, i.e., the pressure on the elastic medium or tissues and the velocity changes in flowing fluid, have been obtained. These results are meaningful for further modeling and experimental tests of the three prototypes.

Chapter 7 Conclusions and Recommendations

7.2 Future work

The future work of this study is listed as follows,

- 1) Optimal excitation of plates and shells by piezoelectric materials for general boundary conditions. In Chapter 4, a simple yet general procedure is provided for finding the optimal locations of actuators. From the mathematical formulation, it is evident that the CPMF will change with the change of boundary conditions. By using the p-Ritz method (Liew et al, 1998) with polynomial solutions, it is possible to obtain a general expression of CPMF for general boundary conditions. Thus, the optimal excitation of plates and shells under general boundary conditions could be solved.
- 2) The optimal placement of multiple piezoelectric actuators should be investigated based on the conclusions obtained for single actuator placement. Experimental tests should be carried out to verify the theory.
- 3) The dynamic behaviors of IPMC should be further studied. Nemat-Nasser's hybrid actuation model provides a methodology to study the actuation and sensing mechanism of IPMC. The IPMC actuation is a complex process involving electric field induced charge transports, ion-ion interactions and ion-solvent-cluster interactions. The parameters of IPMC microstructure and physical variables are mostly time-dependent variables and difficult to determine. By introducing the probability approach to the micromechanics analysis of the IPMC actuation, a comprehensive understanding of IPMC actuation could be possible.
- 4) The phase lag effect in IPMC. Phase lag between the vibration response of IPMC and driving signal has been observed in almost all experiments. However, little research has been done on the quantitative analysis of the phase lag effect. The understanding and control of phase lag effect is very important for biomedical applications of IPMCs whose dynamic responses

Chapter 7 Conclusions and Recommendations

are required to be precisely controlled such as the heart compression band. Analytical and experimental studies are needed to acquire a good understanding of this phenomenon.

- 5) Frequency dependent characteristics of IPMC. From the bending moment expression Eq.(5.79), it is observed that the higher the driving frequency, the smaller the bending moment and therefore the smaller the vibration amplitude of IPMC. This observation is consistent with experimental observations. However, experimental tests are needed to verify this expression and justify model parameters.
- 6) Modeling of IPMCs' sensing capacity. Compared to the research on IPMC actuation, little progress has been made to study the sensing ability of IPMC. First principle models are needed to determine the quantitative relation between IPMC deformation and charge concentration on electrodes.
- 7) Further modeling and experimental tests of the three prototypes of IPMC for biomedical applications presented in Chapter 6, i.e., the beam structure for minimum invasive surgery, the ring structure for heart compression band and the fluid-filled cylindrical shell for artificial vessels should be carried out. The problem of optimizing the performance of multiple electrodes IMPC beams, rings and cylindrical shells with flowing fluid should be considered in future study of the three models. Extensive experimental tests are needed to verify the models and justify model parameters.

References

Abe H, Hayashi K and Sato M (1996), *Data Book on Mechanical Properties of Living Cells, Tissues, and Organs*, Tokyo: Springer-Verlag.

Abramovich H (1998) "Deflection control of laminated composite beams with piezoceramic layers--closed form solution", *Composite Structures*, 43(3), 217–231.

Akle B J and Leo D J (2005), "Correlation of capacitance and actuation in ionomeric polymer transducers", *Journal of Materials Science*, 40(14), 3715–3724.

Akle B J, Bennett M D and Leo D J (2006), "High-strain ionomeric-ionic liquid electroactive actuators", *Sensors and Actuators A: Physical*, 126(1), 173–181.

Aldraihem O J and Khdeir A A (2000), "Smart beams with extension and thickness-shear piezoelectric actuators", *Smart Materials and Structures*, 9(1), 1–9.

Aldraihm O J and Khdeir A A (2003), "Precise deflection analysis of beams with piezoelectric patches", *Composite Structures*, 60(2), 135–143.

Alterman Z and Loewenthal D (1972), "Computer generated seismograms", *Methods in Computational Physics vol 12* (ed B Adder et al), 35–164, New York: Academic Press.

Asaka K and Oguro K (2000a), "Bending of polyelectrolyte membrane platinum composites by electric stimuli II: response kinetics", *Journal of Electroanalytical Chemistry*, 480 (1–2), 186–198.

References

Asaka K and Oguro K (2000b), “Bending of polyelectrolyte membrane platinum composites by electric stimuli III: self-oscillation”, *Electrochimica Acta*, 45 (27), 4517-4523.

Asaka K, Oguro K, Nishimura Y, Mizuhata M and Takenaka H (1995), “Bending of polyelectrolyte membrane platinum composites by electric stimuli I: response characteristics to various waveforms”, *Polymer Journal*, 27 (4), 436-440.

Baillargeon B P and Vel S S (2005), “Exact solution for the vibration and active damping of composite plates with piezoelectric shear actuators”, *Journal of Sound and Vibration*, 282(3-5), 781-804.

Barboni R, Mannini A, Fantini E and Gaudenzi P (2000), “Optimal placement of PZT actuators for the control of beam dynamics”, *Smart Materials and Structures*, 9(1), 110-120.

Bar-Cohen Y (Editor) (2001), *Electroactive polymer (EAP) Actuators as Artificial Muscles, Reality, Potential, and Challenges*, Washington: SPIE Press.

Bar-Cohen Y (Editor) (2004), *Electroactive polymer (EAP) Actuators as Artificial Muscles, Reality, Potential, and Challenges*, 2nd Edition, Washington: SPIE Press.

Bar-Cohen Y (Editor) (2006), *Biomimetics: biologically inspired technologies*, New York: CRC/Taylor & Francis.

Bennett M D and Leo D J (2004), “Ionic liquids as stable solvents for ionic polymer transducers”, *Sensors and Actuators A: Physical*, 115(1), 79-90.

Bennett M D, Leo D J, Wilkes G L, Beyer F L and Pechar T W (2006) “A model of charge transport and electromechanical transduction in ionic liquid-swollen Nafion membranes”, *Polymer*, 47(19), 6782-6796.

References

- Bonomo C, Fortuna L, Giannone P and Graziani S (2005), “A method to characterize the deformation of an IPMC sensing membrane”, *Sensor and Actuators A Physical*, 123-124, 146-154.
- Bruant I, Coffignal G, Lene F and Vege M (2001), “A Methodology for determination of piezoelectric actuator and sensor location on beam structures”, *Journal of Sound and Vibration*, 243(5), 861-882.
- Centolanza L R and Smith E C (2002), “Induced-shear piezoelectric actuators for active twist rotor blades”, *43rd AIAA/ASME/ASCE/AHS/ASC Structures, Structural dynamics, and Materials conference*, Denver, Colorado, April 2002.
- Chandrashekhara K and Varadarajan S (1997), “Adaptive shape control of composite beams with piezoelectric actuators”, *Journal of Intelligent Material Systems and Structures*, 8(2), 112-124.
- Cheng C C and Lin C C (2005), “An impedance approach for vibration response synthesis using multiple PZT actuators”, *Sensors and Actuators A: Physical*, 118(1), 116-126.
- Chu X, Ma L and Li L (2006), “A disk-pivot structure micro piezoelectric actuator using vibration mode B_{11} ”, *Ultrasonics*, 44, Supplement 1, e561-e564.
- Crawley E F and Luis J D (1987), “Piezoelectric actuators as elements of intelligent structures”, *AIAA Journal*, 25(10), 1373-1385.
- Damaren C J (2003), “Optimal location of collocated piezo-actuator/sensor combinations in spacecraft box structures”, *Smart Materials and Structures*, 12(3), 494–499.
- Dimitriadis E K, Fuller C R and Rogers C A (1991), “Piezoelectric actuators for distributed vibration excitation of thin plates”, *Journal of Vibration and Acoustics*,

References

113(1), 100-107.

Dong S, Bouchilloux P, Du X H and Uchino K (2001), "Ring type Uni/BiMorph piezoelectric actuators", *Journal of Intelligent Material Systems and Structures*, 12(9), 613-616.

Farinholt K and Leo D J (2004), "Modeling of electromechanical charge sensing in ionic polymer transducers", *Mechanics of Materials*, 36(5-6), 421-433.

Fernandes A and Pouget J (2006), "Structural response of composite plates equipped with piezoelectric actuators", *Computers and Structures*, 84(22-23), 1459-1470.

Glazounov A E and Zhang Q M (1998), "Piezoelectric actuator generating torsional displacement from piezoelectric d_{15} shear response", *Applied Physics Letters*, 72(20), 2526-2528.

Gorman D J (1982), *Free Vibration Analysis of Rectangular Plates*, New York: Elsevier.

He J H, Liu H M and Pan N (2003), "Variational model for ionomeric polymer-metal composite", *Polymer*, 44(26), 8195-8199.

IEEE Standard on Piezoelectricity (1987), ANSI/IEEE, Std. 176.

Ikeda T (1990), *Fundamentals of Piezoelectricity*, Oxford University Press, Oxford.

Ip K H and Tse P C (2001), "Optimal configuration of a piezoelectric patch for vibration control of isotropic rectangular plates", *Smart Materials and Structures*, 10(2), 395-403.

References

-
-
- Jin Z, Yang Y W and Soh C K (2005), “Application of fuzzy GA for optimal vibration control of smart cylindrical shells”, *Smart Materials and Structures*, 14(6), 1250–1264.
- Kang Y K, Park H C, Hwang W and Han K S (1996) “ Optimum placement of piezoelectric sensor/actuator for vibration control of laminated beams”, *AIAA Journal*, 34(9), 1921-1926.
- Khdeir A A and Aldraihm O J (2001), “Deflection analysis of beams with extension and shear piezoelectric patches using discontinuity functions”, *Smart Materials and Structures*, 10(2), 212-220.
- Kim J H, Kim S H and Kwak Y K (2003), “Development of a piezoelectric actuator using a three-dimensional bridge-type hinge mechanism”, *Review of Scientific Instruments*, 74(5), 2918-2924.
- Kim K J and Shahinpoor M (2003), “Ionic polymer-metal composites: II. Manufacturing techniques”, *Smart Materials and Structures*, 12(1), 65-79.
- Leissa A W (1973), “The free vibration of rectangular plates”, *Journal of Sound and Vibration*, 31, 257-293.
- Liew K M, Wang C M, Xiang Y and Kitipornchai S (1998), *Vibration of Mindlin Plates : Programming The p-version Ritz Method*, , Oxford UK, Elsevier Science.
- Markus S (1988), *The Mechanics of Vibrations of Cylindrical Shells*, New York: Elsevier.
- Matthews J L, Lada E K, Weiland L M, Smith R C and Leo D J (2006) “Monte Carlo simulation of a solvated ionic polymer with cluster morphology”, *Smart Materials and Structures*, 15(1), 187-199.

References

Mehrabian A R and Yousefi-Koma A (2007), “Optimal positioning of piezoelectric actuators on a smart fin using bio-inspired algorithms”, *Aerospace Science and Technology*, 11(2-3), 174-182.

Nemat-Nasser S (2002), “Micromechanics of actuation of ionic polymer-metal composites”, *Journal of Applied Physics*, 92(5), 2899-2915.

Nemat-Nasser S and Li J Y (2000), “Electromechanical response of ionic polymer-metal composites”, *Journal of Applied Physics*, 87(7), 3321-3331.

Nemat-Nasser S and Thomas C (2001), *Electroactive polymer (EAP) Actuators as Artificial Muscles, Reality, Potential, and Challenges*, edited by Yoseph Bar-Cohen, 2nd Edition, Chapter 6, 171-230, Washington: SPIE Press.

Nemat-Nasser S and Wu Y (2003), “Comparative experimental study of the ionic polymer-metal composites with different backbone ionomers and in various cation forms”, *Journal of Applied Physics*, 93(9), 5255-5267.

Nemat-Nasser S and Wu Y (2006), “Tailoring the actuation of ionic polymer-metal composites”, *Smart Materials and Structures*, 15(1) 1-15.

Nemat-Nasser S and Zamani S (2006a), “Effect of solvents on the chemical and physical properties of ionic polymer-metal composites”, *Journal of Applied Physics*, 99, 104902.

Nemat-Nasser S and Zamani S (2006b), “Modeling of electrochemomechanical response of ionic polymer-metal composites with various solvents”, *Journal of Applied Physics*, 100, 064310.

Newbury K M and Leo D J (2002), “Electromechanical modeling and characterization of ionic polymer benders”, *Journal of Intelligent Material Systems and Structures*, 13(1), 51-60.

References

- Newbury K M and Leo D J (2003a), “Linear electromechanical model of ionic polymer transducers-part I: Model development”, *Journal of Intelligent Material Systems and Structures*, 14(6), 333-342.
- Newbury K M and Leo D J (2003b), “Linear electromechanical model of ionic polymer transducers-part II: Experimental validation”, *Journal of Intelligent Material Systems and Structures*, 14(6), 343-357.
- Oguro K, Kawami Y and Takenaka H (1992) “Bending of an ion-conducting polymer film-electrode composite by an electric stimulus at low voltage”, *Trans. Journal of Micromachine Society*, 5, 27-30.
- Paidoussis M P (2004), *Fluid-Structure Interactions: Slender Structure and Axial Flow*, Vol 2, New York: Elsevier Academic Press.
- Paquette J W and Kim K J (2004), “Ionomeric electroactive polymer artificial muscle for naval applications”, *IEEE Journal of Ocean Engineering*, 29(3), 729-737.
- Preumont A (2002), *Vibration Control of Active Structures: An Introduction*, London: Kluwer Academic Publishers.
- Qing G, Qiu J and Liu Y (2006), “A semi-analytical solution for static and dynamic analysis of plates with piezoelectric patches”, *International Journal of Solids and Structures*, 43(6), 1388-1403.
- Qiu Z, Zhang X, Wu H and Zhang H (2007), “Optimal placement and active vibration control for piezoelectric smart flexible cantilever plate”, *Journal of Sound and Vibration*, 301(3-5), 521-543.
- Rao J S (1999), *Dynamics of Plates*, New Delhi: Narosa Publishing House.

References

Rogers C A, Barker D K and Jaeger C A (1988), “Introduction to Smart Materials and Structures”, *Smart Materials, Structures and Mathematical Issues*, U.S. Army Research Office Workshop, Virginia Polytechnic Institute & State University, Sept. 15-16, 1988, 17-27.

Sadeghipour K, Salomon R and Neogi S (1992) “Development of a novel electrochemically active membrane and ‘smart’ material based vibration sensor/damper”, *Smart Materials and Structures*, 1(2), 172-179.

Shahinpoor M (1992), “Conceptual design, kinematics and dynamics of swimming robotic structures using ionic polymer gel muscles”, *Smart Materials and Structures*, 1(1) 91-94.

Shahinpoor M and Kim K J (2001), “Ionic polymer-metal composites: I. fundamentals”, *Smart Materials and Structures*, 10(4), 819-833.

Shahinpoor M and Kim K J (2002), “Mass transfer induced hydraulic actuation in ionic polymer-metal composites”, *Journal of Intelligent Material Systems and Structures*, 13(6), 369-376.

Shahinpoor M and Kim K J (2004), “Ionic polymer-metal composites: III. Modeling and simulation as biomimetic sensors, actuators, transducers, and artificial muscles”, *Smart Materials and Structures*, 13(6), 1362-1388.

Shahinpoor M and Kim K J (2005), “Ionic polymer-metal composites: IV. Industrial and medical applications”, *Smart Materials and Structures*, 14(1), 197-214.

Soedel W (2004), *Vibrations of shells and plates*, 3rd Edition, New York: Marcel Dekker.

References

Sun C T and Zhang X D 1995 “Use of thickness-shear mode in adaptive sandwich structures”, *Smart Materials and Structures*, 4(3), 202–206.

Tamagawa H, Yagasaki K and Nogata F (2002), “Mechanical characteristics of ionic polymer-metal composite in the process of self-bending”, *Journal of Applied Physics*, 92(12), 7614-7618.

Thompson B S, Gandhi M V and Kasiviswanathan S (1992), “An introduction to smart materials and structures”, *Materials and design*, 13(1), 3-9.

Ting T C T (1996), *Anisotropic Elasticity: Theory and Applications*, Oxford: Oxford University Press.

Toi and Kang (2005), “Finite element analysis of two-dimensional electrochemical-mechanical response of ionic conducting polymer-metal composite beams”, *Computers and Structures*, 83(31-32), 2573-2583.

Uchino K (1996), *Piezoelectric Actuator and Ultrasonic Motors*, Boston: Kluwer Academic.

Vel S S, Mewer R C and Batra R C (2004), “Analytical solution for the cylindrical bending vibration of piezoelectric composite plates”, *International Journal of Solids and Structures*, 41(5-6), 1625-1643.

Wang Q and Wang C M (2000), “Optimal placement and size of piezoelectric patches on beams from the controllability perspective”, *Smart Materials and Structures*, 9(4), 558-567

Wang Q, Xu B, Kugel V D and Cross L E (1996), “Characteristics of shear mode piezoelectric actuators”, *Proceedings of the Tenth IEEE International Symposium on Applications of Ferroelectrics*, 1, 767-770.

References

-
-
- Wang Z, Zhu W and Yao X (2002), “d31 type inplane bending multilayer piezoelectric microactuators-a design concept and its application”, *Sensors and Actuators A: Physical*, 101(3), 262-268.
- Weiland L M and Leo D J (2005a) “Computational analysis of ionic polymer cluster energetics”, *Journal of Applied physics*, 97, 013541.
- Weiland L M and Leo D J (2005b) “Ionic polymer cluster energetics: Computational analysis of pedant chain stiffness and charge imbalance”, *Journal of Applied physics*, 97, 123530.
- Wetherhold R, Messer M and Patra A (2003), “Optimization of directionally attached piezoelectric actuators”, *Journal of Engineering Materials and Technology*, 125(2), 148-152.
- Yagasaki K and Tamagawa H (2004), “Experimental estimate of viscoelastic properties for ionic polymer-metal composites”, *Physical Review E*, 70, 052801.
- Yamakita M, Kamamichi N, Kaneda Y, Asaka K and Luo Z W (2004), “Development of an artificial muscle linear actuator using ionic polymer-metal composites”, *Advanced Robotics*, 18(4) 383-399.
- Yang Y W, Ju C K and Soh C K (2003), “Analytical and semi-analytical solutions for vibration control of a cantilevered column using a piezoelectric actuator”, *Smart Materials and Structures*, 12(2), 193-203.
- Zhang X and Erdman A G (2006), “Optimal placement of piezoelectric sensors and actuators for controlled flexible linkage mechanisms”, *Journal of Vibration and Acoustics*, 128(2), 256-260.
- Zhang X D and Sun C T (1996), “Formulation of an adaptive sandwich beam”, *Smart Materials and Structures*, 5(6), 814–823.

List of Publications

- 1 Yang Y.W. and Zhang L. (2006) “Optimal excitation of a rectangular plate resting on an elastic foundation by a piezoelectric actuator”, *Smart Materials and Structures*, 15(4), 1063-1078.
- 2 Zhang L. and Yang Y.W. (2007), “Modeling of ionic polymer-metal composite beam on human tissues”, *Smart Materials and Structures*, 16(2), S197-S207.
- 3 Yang Y.W. and Zhang L. (2008) “Modeling of ionic polymer-metal composite ring”, *Smart Materials and Structures*, 17(1), 015023.
- 4 Zhang L. and Yang Y. W. (2008) “Modeling of a fluid-filled ionic polymer-metal composite cylindrical shell as artificial vessel”, *Smart Materials and Structures* (under review).
- 5 Zhang L. and Yang Y.W. (2006) “Modeling of ionic polymer-metal composite (IPMC) beam on human tissues”, *SPIE 13th International Symposium on Smart Structures and Materials cum International Conference on Electroactive Polymer Actuators and Devices (EAPAD)*, Proceedings of SPIE, 6168-47, 26 Feb.–2 Mar., San Diego, CA.
- 6 Zhang L. and Yang Y.W. (2006) (*Invited Paper*), “Modeling of a fluid-filled ionic polymer-metal composite cylindrical shell”, *SPIE International Symposium on Smart Materials, Nano- and Micro-Smart Systems cum Smart Structures, Devices, and Systems III*, Proceedings of SPIE, 6414-15, 11-13 Dec. Adelaide, Australia.
- 7 Zhang L. and Yang Y.W. (2007), “Effect of charge redistribution on dynamic actuation of ionic polymer-metal composites”, *SPIE 14th International Symposium on Smart Structures and Materials cum International Conference*

List of Publications

- on Electroactive Polymer Actuators and Devices (EAPAD)*, Proceedings of SPIE, 6524-11, 18–23 Mar., San Diego, CA.
- 8 Zhang L. and Yang Y.W. (2007), “Optimal excitation of a cylindrical shell by piezoelectric actuators”, *SPIE 14th International Symposium on Smart Structures and Materials cum Active and Passive Smart Structures and Integrated Systems*, Proceedings of SPIE, 6525-84, 18–23 Mar., San Diego, CA.
- 9 Yang Y.W. and Zhang L. (2007) (*Invited Paper*), “Modeling of dynamic behaviors of ionic polymer-metal composites”, *Proceeding of World Forum on Smart Materials and Smart Structures Technology*, 22-27 May, Nanjing & Chongqing, Paper no. 392.
- 10 Zhang L. and Yang Y.W. (2008), “Three-dimensional charge redistribution of ionic polymer-metal composites with uncertainty in surface conductivity”, *International Conference on Multifunctional Materials and Structures*, paper number MF138, 28-31 July, Hong Kong, China. (Accepted)